Order Number 9020743

Search for a particle at 1.8 MeV through resonant Bhabha scattering

Asoka Kumar, Palakkal P. V., Ph.D.

City University of New York, 1990

U·M·I
300 N. Zeeb Rd.
Ann Arbor, MI 48106

SEARCH FOR A PARTICLE AT 1.8 MeV THROUGH RESONANT BHABHA SCATTERING

by

PALAKKAL P.V. ASOKA KUMAR

A Dissertation submitted to the Graduate Faculty in Physics in partial fulfillment of the requirements for the degree of Doctor of Philosophy, The City University of New York.

1990

This manuscript has been read and accepted for the Graduate Faculty in Physics in satisfaction of the dissertation requirement for the degree of Doctor of Philosophy.

Oct. 11, 1989

Date

Prof. M.S. Lubell
Chair of Examining Committe

Dec. 4 1989

Date

Prof. J. Gersten
Executive Officer

Prof. M. Dine

Prof. P. Nemethy

Prof. L.O. Roellig

Prof. C.M. Shakin
Supervisory Committee

The City University of New York

Abstract

SEARCH FOR A PARTICLE AT 1.8 MeV
THROUGH RESONANT BHABHA SCATTERING

by

PALAKKAL P.V. ASOKA KUMAR

Adviser: Professor Michael S. Lubell

This thesis describes an experimental approach to a search for a particle of mass 1.8 MeV through the use of resonant Bhabha scattering. The project was motivated by the discovery of correlated back-to-back electron-positron pairs observed at GSI, Darmstadt, Germany. If the pair generation is due to the formation and subsequent decay of a new low-mass neutral particle, evidence for such a particle should be found in the production of a resonance in s-channel Bhabha scattering. In order to search for such a resonance an experiment was developed at Brookhaven National Laboratory which is sensitive to a particle of lifetime shorter than a few times 10^{-13} sec. A ^{22}Na β^+ source with a 6000 Å-thick W(100) transmission moderator was employed to produce a positron beam with an intensity of 5×10^5 e^+/sec, a half-angle divergence of less than 0.5°, and a FWHM size of 1.1 mm. The beam energy spread at the target was found to be less than 1

keV (FWHM), and the high-energy contamination of the beam from the unmoderated positrons, less than 1 e^+/sec. The thesis contains descriptions of the positron beam generation, extraction, acceleration and transport, as well as summaries of the GSI studies, prior searches for a neutral particle, and preliminary measurements at Brookhaven.

Acknowledgements

My first word of thanks goes to my supervisor, Prof. M.S. Lubell for his constant encouragement and understanding during the course of this work. I express my sincere appreciation to Dr. K.G. Lynn for making the work presented here enjoyable. I have enjoyed the research atmosphere provided by the positron group at Brookhaven National laboratory and have benifited from the company of Dr. S. McCorkle, Dr. A. Vehanen, Dr. H. Huomo, H. Hacker, Dr. M.Weber and Dr. R. Mayer. I also thank S.D. Henderson, B. Phlips, Dr. J. McDonough, and Prof. J.S. Greenberg of Yale university for valuable discussions at various stages of this work.

Finally, I wish to thank my parents, Sri. P.K.K. Nambiar & Smt. P.V. Rugmini Amma for their love and understanding which helped me in various ways during my academic years.

Table of Contents

Chapter 1:

The Impetus for the Project:

Supercritical Fields and Heavy Ion Collisions 1

1. Overview 1

2. Spontaneous Sparking of the Vacuum 2

3. From Theory to Experiment - Predictions 5

4. Superheavy Quasimolecules 6

5. Positron Experiments - Spectrometers 7

6. Gross Features and Background 9

7. Narrow Lines in the Positron Spectrum 13

8. Monoenergetic Electron-Positron Pair Production 18

Chapter 2:

The Conjecture of a New Particle or a Composite System 24

1. Overview 24

2. The Absence of the Spontaneous Sparking 25

3. Failure of Conventional Schemes - Atomic and Nuclear Origins 26

4. The Particle Scenario 29

5. Model-Dependent Constraints on the Particle 32

6. Model-Independent Constraints on the Particle 37

7. Is it a Composite System ? 51

Quasibound Electron-Positron State and Poly-positronium . . 52

New QED Phase 53

A Model with New Fermions 57

8. Constraints on a Light Composite Particle 58

Chapter 3:

Experimental Approach - Phenomenological considerations 61

1. Overview 61

2. Resonant Bhabha Scattering off Electrons at Rest 62

3. Resonant Bhabha Scattering off Electrons Bound in an Atom . 74

4. The Effects of Spread in Beam Parameters 82

5. Normalization using the Mott Scattering 83

6. Results from Experiments Performed at other Facilities 84

Chapter 4:

Details of the Experimental Setup 95

1. Overview 95

2. Positron Beam Production 95

The Positron Source 96

Moderator 99

Source Chamber 104

3. The Design and The Fabrication of The Filter System 104

4. The Acceleration 114

5. The Beam Transport System 119

The Solenoid Lens 120

The Double Focusing Bending Magnet 121

The TRANSPORT Program and The Beam Line Design . . 124

Beam Monitoring System 127

6. The Target Chamber, Detector System, and Beam Dump . . 132

Chapter 5:

Results and Conclusions 142

References 153

List of Figures

Fig. 1.2.1 Energy levels of a point charge nucleus 4

Fig. 1.6.1 Positron spectrum observed in superheavy ion collisions . . 11

Fig. 1.6.2 Total positron production 12

Fig. 1.7.1 First positron peak observed at GSI 14

Fig. 1.7.2 Z dependence of the 1s resonance state 15

Fig. 1.7.3 Positron spectra for six collision systems 16

Fig. 1.8.1 Intensity distribution of the coincident events 19

Fig. 1.8.2 Projections of intensity distributions for coincident events . 20

Fig. 1.8.3 Additional coincident peaks 21

Fig. 2.6.1 Beam dump experiment 38

Fig. 2.6.2 Feynman diagram for Delbrück scattering 40

Fig. 2.6.3 Feynman diagram for positronium hyperfine level splitting . 41

Fig. 2.6.4 Corrections to the magnetic moment of a lepton 45

Fig. 2.6.5 The coefficient K_i 46

Fig. 2.6.6 Mass-lifetime plot for excluded regions 50

Fig. 2.7.1 Phase diagram for QED 56

Fig. 3.2.1 Feynman diagram for resonant Bhabha scattering 64

Fig. 3.2.2 Differential cross section for resonant Bhabha scattering . . 73

Fig. 3.3.1 Resonant Bhabha scattering off a bound electron 76

Fig. 3.3.2 X-production cross section 79

Fig. 3.3.3 Particle production cross section 80

Fig. 3.6.1 Bhabha scattering cross section 87

Fig. 3.6.2 Experimental setup at Stuttgart 88

Fig. 3.6.3 Results from Stuttgart experiment 89

Fig. 3.6.4 Ratio of Bhabha to Mott scattering cross section 92

Fig. 3.6.5 Ratio of Bhabha to Mott scattering cross section 93

Fig. 4.2.1 The ^{22}Na source 98

Fig. 4.3.1 Positron spectrum 106

Fig. 4.3.2 Modified Soa gun 107

Fig. 4.3.3 Positron trajectories through the modified soa gun 109

Fig. 4.3.4 Symmetrical einzel lens system 111

Fig. 4.3.5 The filter system 112

Fig. 4.3.6 Positron trajectories through the filter section 113

Fig. 4.4.1 Injection stage of the accelerator 116

Fig. 4.4.2 Trajectories during the initial stages of acceleration 117

Fig. 4.5.1 Double focusing bending magnet 123

Fig. 4.5.2 Layout of the Dynamitron accelerator facility 128

Fig. 4.5.3 Beam envelope through the transport system 130

Fig. 4.6.1 The target chamber 133

Fig. 4.6.2 The detector system 135

Fig. 4.6.3 MWPC and the readout scheme 137

Fig. 4.6.4 Calibration run for Bicron scintillators 138

Fig. 4.6.5 Monte-Carlo of the scattered events 139

Fig. 4.6.6 Read-out block diagram and trigger logic 141

Fig. 5.1 Ge spectra at 1.4 MeV 145

Fig. 5.2 Energy spectrum of Mott and Bhabha events 149

Fig. 5.3 Angular distribution of Mott and Bhabha events 150

List of Tables

Table 1.7.1 Summary of the positron lines observed at GSI 17

Table 2.5.1 Summary of the decay limits on a light neutral particle . . 36

Table 2.6.1 Survey of the results from the beam dump experiments . . 39

Table 2.6.2 Limits on the particle coupling constants 48

Table 3.2.1 The coupling vertices 63

Table 4.5.1 The beam parameters 129

Table 5.1 The final beam parameters 146

Chapter 1.

The Impetus for the Project: Supercritical Fields and Heavy Ion Collisions

1. Overview

Positron production from heavy ion collisions has been under investigation for a decade at GSI, Darmstadt, Germany,[1-2] motivated originally by the possibility of creating supercritical fields.[2] It was argued that in a supercritical nuclear system, such as those created in superheavy ion collisions, the electronic spectrum of the single particle Dirac equation shows one or more resonances in the lower continuum, causing the spontaneous creation of e^+e^- pairs from the vacuum. As a result, the positron spectrum should show sharp peaks, superimposed on a smooth background of positrons produced by dynamical processes. Results from these experiments did indeed show narrow positron peaks at the center-of-mass energies $E_{e^+}^{cm} = 255 \pm 7, 337 \pm 6$, and 396 ± 6 keV. Curiously, however, electron peaks were also observed in coincidence corresponding to center-of-mass sum energies of $624 \pm 10, 760 \pm 20$, and 815 ± 10 keV.[1] Recently,[3] more e^+e^- coincident lines have been reported at sum energies of, 540 ± 16, 640 ± 10, 716 ± 10, 809 ± 8, and 895 ± 10 keV.

This thesis will describe the development of an experimental program at Brookhaven National Laboratory that was stimulated by the GSI findings and that has as its goal a careful search for s-channel resonances in low-energy Bhabha (e^+e^-) scattering. The thesis will emphasize the development and characterization of the intense low-energy positron beam necessary for carrying out the search. It will also highlight the technical problems that must be confronted in such studies and the demands they place on the properties of the beam.

In the remaining sections of chapter 1, we will review in more detail the results of the GSI work and the basic theory of supercritical heavy ion collisions. In chapter 2, we will confront the conjecture of a new particle or a composite in e^+e^- systems. Chapter 3 will describe the general approach to searches for s-channel resonances in Bhabha scattering, and chapter 4 will treat the technical details of the Brookhaven experiment. Chapter 5, which concludes the thesis, will present the experimental characterization of the positron beam as well as some preliminary observations of Bhabha events.

2. Spontaneous Sparking of the Vacuum

Quantum electrodynamics is one of the most triumphant disciplines of theoretical physics, with predictions of great precision for the Lamb shift in atoms,[4] the hyperfine structure of positronium,[5] and the electron anomalous magnetic moment,[6] among others. In spite of the somewhat disturbing divergences in the renormalization scheme, quantum electrodynamics (QED)

can be regarded as a complete theory. But there is a new aspect of QED which attracted attention only recently: the charged vacuum in supercritical electrostatic fields. It starts with the well known Sommerfeld fine structure formula[7]

$$E_{n'j} = m_e c^2 \left\{ \frac{1 + (Z\alpha)^2}{\left(\sqrt{(j+\frac{1}{2})^2 - (Z\alpha)^2} + n' \right)^2} \right\}^{-\frac{1}{2}} \qquad (1.2.1)$$

for a point nucleus, where $m_e c^2$ is the electron rest energy and α is the fine structure constant. The quantum numbers j and n' assume the values $j = \frac{1}{2}, \frac{3}{2}, \frac{5}{2}, \frac{7}{2}...$ and $n' = 0, 1, 2, 3, ...$ Eq. (1.2.1) describes the spectrum of electronic bound states in the external coulomb potential, $V = -\frac{Z\alpha}{r}$, of a point charge Ze and is obtained from the analytic solution of the Dirac equation. The presence of the term $\sqrt{(j+\frac{1}{2})^2 - (Z\alpha)^2}$ in the denominator of Eq. (1.2.1) causes the solution to break down when $Z\alpha > j + \frac{1}{2}$. For example, the curve for the energy as a function of Z for the $1S_{\frac{1}{2}}$ state ceases to exist at $Z = \frac{1}{\alpha} \sim 137$ as shown in the Fig. 1.2.1. The corresponding wave function becomes non-normalizable at the origin. When finite nuclear size effects are included in the calculations, the breakdown is delayed until Z reaches the value[2] $Z_{crit} \sim 173$. Greiner and collaborators [2] traced the levels $E_{n'j}$ down to a binding energy of twice the electron rest energy. At this charge number, the energy levels meet the "Dirac sea", which is filled with electrons according to the particle-hole interpretation of the solution to the Dirac equation. When the strength of the nuclear electromagnetic field is increased further, bound states will "dive" into the negative energy continuum. If an eigenlevel of such a system is empty initially, then as the field crosses the

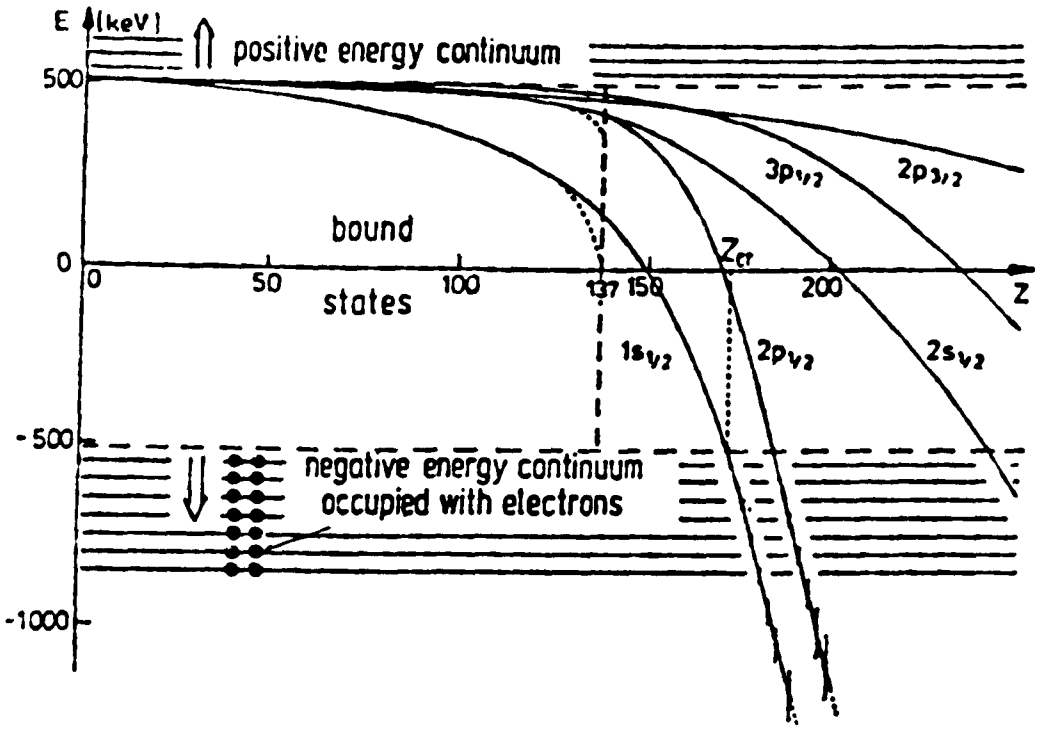

Figure 1.2.1 Ground state of the Dirac equation for a point nucleus with charge Ze. Sommerfeld fine structure formula breaks down at $Z = 137$, whereas solutions with finite nuclear size effects break down at $Z_{crit} \sim 173$.[2]

critical value, the creation of an e^+e^- pair from the vacuum becomes energetically favorable. Under these circumstances, the electron becomes bound to the supercritical nucleus, and the positron appears spontaneously in the laboratory, a combined process sometimes called spontaneous sparking.

3. From Theory to Experiment - Predictions

In nature, there are no stable nuclear systems with $Z \sim 173$. Thus an attempt was made to create supercritical fields through heavy ion collisions. A crucial question had to be answered. Would such collisions truly provide good enough time to create the fields necessary for charging the vacuum? If the electrons see the combined nuclear charge as the source of the binding potential, the system will behave as an atomic molecule with a superheavy nucleus. However, even if formed, this supercritical quasimolecule must live long enough, to allow the vacuum to decay. In addition, if electron capture is to occur, the quasimolecule must be produced with an empty low-lying level; that is a hole in the strongly bound K-shell.

It should be noted that the kinetic energy of the escaping positrons (given by the binding energy - $2m_ec^2$) will not be sharp, but will have a Breit-Wigner type distribution, due to the finite decay time of the empty shell imbedded in the negative energy continuum. Furthermore, it should have a strong dependence on Z. Indeed, from a self consistent solution of the Dirac equation, it was shown[2] that the mean energy of the spontaneously emitted positrons should follow an unusual Z_u^{20} dependence on the combined nuclear charge Z_u. Thus an experiment using different projectile-target combinations with Z_u ranging from $Z_u < Z_{crit}$ to $Z_u > Z_{crit}$ should provide an unambiguous signature for spontaneous sparking.

4. Superheavy Quasimolecules

In a collision of two superheavy ions, electrons will experience the combined potential of both the nuclei, for a very short period of time. Thus the first task carried out at GSI was to establish the existence of superheavy quasimolecules. The velocity of the colliding nuclei was chosen so that the electrons could adjust to the increasing strength of the potential of the nuclei as they approached each other. At energies up to 6 MeV/amu, the nuclear coulomb barrier decelerates the incident nuclei, thereby considerably reducing their relative velocity while they are at close internuclear distances. At such energies the nuclear motion is 5-10 times slower than the electronic motion.

The existence of the superheavy quasimolecules was unambiguously confirmed in a series of experiments by Greenberg and coworkers [8] using the characteristic Doppler shifted, K-Xray lines. In addition, they determined that the ionization probability of 1s state is of the order of several percent, while that of the $2p_{\frac{1}{2}}$ states is 50% or more. (It should be remembered that the rate of K-hole production is crucial for the spontaneous sparking of the vacuum, since it describes the available empty K-levels for the "diving" process.)

A second class of experiments, tested the strong localization of the quasimolecule wave functions. The detailed study of the energy distribution of the ejected electrons provided the necessary access.[9] These studies

provided additional evidence for the production of the superheavy quasimolecules during the collisions.

5. Positron Experiments - Spectrometers

The experimental configurations used to detect the positrons emitted during the heavy ion collisions must satisfy a number of needs. First, since positron production cross sections are fairly small (a few positrons for every 10^5 collisions), the spectrometers employed have to detect positrons emitted into a wide range of solid angles with good efficiency. Second, since the super heavy ion collisions initiate many other processes, the positrons have to be filtered out from an overwhelming background of γ rays, delta electrons, and neutrons. Third, since the correct nuclear reactions must be isolated, the scattered ions must be tagged appropriately.

To meet these challenges, the GSI detector systems were designed with large sensitivity for the primary positrons and with the simultaneous suppression of positrons from pair creation. The primary positrons originate from the quasimolecule which is at rest in the center of mass of the colliding system and is moving along the beam direction. On the other hand, positrons produced by pair creation originate mostly from individual colliding partners and have velocity components perpendicular to the beam direction. The difference in their velocity properties can be used to separate primary positrons from the pair created positrons. All of the detector systems used in the studies at GSI employed a magnetic transport system to collect the positrons and

guide them to the detectors away from the interaction region. While we will concentrate most heavily in this thesis on the experimental results of the EPOS spectrometer (Electron POsitron Spectrometer),[1] we wish to point out that significant contributions have also been made by the *Orange* type β-spectrometer [10] group.

The EPOS experiment used a solenoidal transport system in which the magnetic field produced by the solenoid focused the positrons from the target onto a cylindrical energy-sensitive Si(Li) counter. The opposite sense of helical motion of positrons and electrons in a magnetic field permits the positrons to be transported selectively. In the early EPOS experiments, the electrons were simply rejected by the transport system; however, in some of the later experiments the electrons were simultaneously transported to the opposite end of the spectrometer where they were sensed by another set of detectors. This arrangement provided high efficiency for the collection of the positrons and electrons produced from the quasimolecular target and suppressed the detection of the scattered positrons and electrons along with those created by external pair conversion. The target chamber was itself lined with position sensitive parallel-plate avalanche counters which detects the heavy ions, thereby determining the scattering kinematics on an event by event basis. The coincident detection of the positrons (and electrons) permitted the positron (and electron) peaks to be correlated to the heavy ion kinematics. Additional γ-ray detectors were used to monitor the nuclear radiation.

The *Orange* spectrometer also employed a magnetic field for the momentum and the charge analysis of the detected particles. In the case of *Orange* spectrometer, however, point-to-point focusing was used for momentum analysis. The toroidal magnetic field focused the positrons originating from one point on the axis, namely the target, onto a point on the other side of the field torus. Since the focal point depends on the momentum of the positron, the positron energy could be determined by means of a position sensitive detector. At a given strength of the magnetic field only a narrow range of the positron momenta were selected. Hence, the magnetic strength was varied in steps to measure the full positron spectrum. The positron detector itself consisted of a plastic scintillator surrounded by a set of proportional counters to filter out γ-rays.

6. Gross Features and Background

A variety of background processes can produce positrons in a heavy ion collision, most of which involve the conversion of a real or virtual γ-ray into an electron-positron pair. The processes include internal conversion of γ-rays from the highly excited nuclear states, external conversion of γ-rays in the target, external conversion of γ-rays in the transport system or in the detector, and conversion of X-rays produced by nuclear or electronic bremsstrahlüng. In nuclear collisions, it is easy to create a highly deformed nuclei with a rich collection of low-lying rotational bands. As a result, internal pair conversion from the excited nuclear levels dominate the background by far.

Electric monopole transitions contribute, since they occur by internal conversion with subsequent ejection of a bound atomic electron. For transitions of higher multipolarity (E1,M1,E2,etc.), the positron spectrum reflects the γ-ray spectrum of the excited nuclei. In this case the differential positron production is given by[2]

$$\frac{dN(e^+)}{dE_p} = N_\gamma(E_x)\frac{d\beta_{M\lambda}(E_x)}{dE_p}, \tag{1.6.1}$$

where $N_\gamma(E_x)$ is the number of photons with energy E_x, $M\lambda$ is the multipolarity of the transition, E_p is the energy of the emitted positrons, and $\frac{d\beta}{dE_p}$ is the differential conversion coefficient which can be calculated very reliably, since it is not influenced significantly by nuclear structure. Since pair conversion occurs only if E_x is greater than $2m_ec^2$, the contribution to the positron spectrum from the nuclear transition is given by

$$\frac{dN(e^+)}{dE_p} = \int_{2m_ec^2}^{\infty} dE_x N_\gamma(E_x)\frac{d\beta_{M\lambda}(E_x)}{dE_p}. \tag{1.6.2}$$

As a practical matter it is hard to measure the multiplicity of these γ-ray lines, since the γ-rays emitted above 1 MeV are continuous and intrinsically Doppler shifted. Experimentally a mean multipolarity is therefore deduced, and the same value is used for nuclei with similar structures. The effective multipolarity can then be used to determine the positron background.

A method to determine the mean multipolarity involves the measurement of γ-ray and positron yield as a function of Z_u.[11] Fig. 1.6.1(a) shows the result of such a study and shows that the ratio of the positron yield

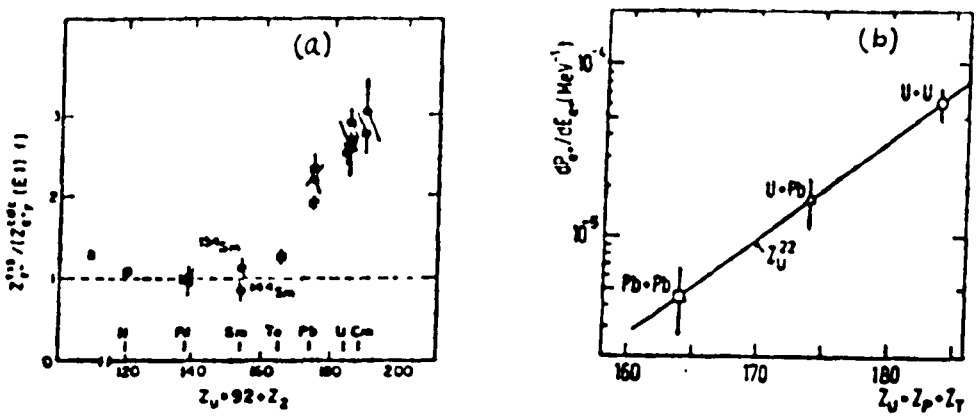

Figure 1.6.1 (a) Observed positron yield in Uranium + Z_2 collisions compared with the yield expected from conversion of the measured γ-ray spectra. The steep rise beyond 160 is due to vacuum "shake off". (b) Z dependence of the induced positron production with the theoretical prediction (solid curve).[2]

from experiment and theory is a constant upto $Z_u \sim 160$.[12] However, the ratio rises fast after $Z_u \sim 160$. This rise is attributed to a process known as "shake off" of the vacuum polarization cloud. In the strong coulomb field of the colliding heavy ions, virtual electron-positron pairs are formed in greater numbers than in the case of normal atoms, and some fraction of these virtual pairs are excited onto the mass shell, due to the time varying coulomb field. This process has been called *shake-off of the vacuum polarization cloud.*[13] Since the total charge of the colliding partners exceeds the fine structure constant, this is essentially a nonperturbative aspect of QED. Hence, it is impossible to calculate this process using a Feynman diagram approach. Lowest order Feynman diagram gives $Z_1^2 Z_2^2$ dependence, whereas experimentally it varies like $(Z_1 + Z_2)^{20}$ as shown in the Fig. 1.6.1(b).[14] The

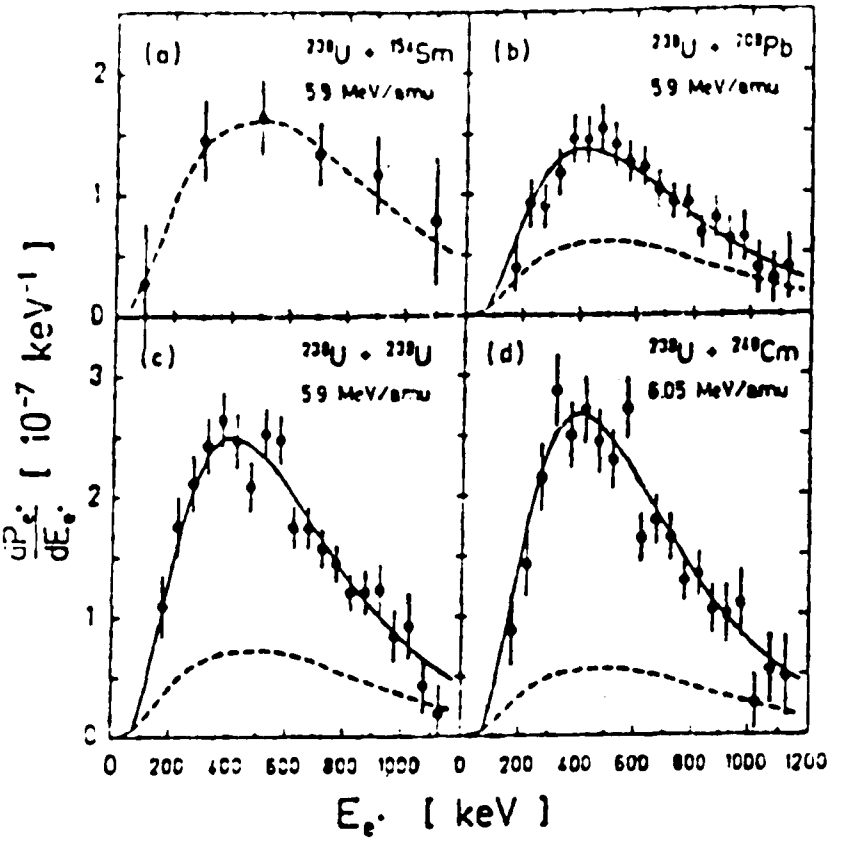

Figure 1.6.2 Scattering-angle averaged kinetic energy distribution of positron production probabilities for four different scattering systems. Broken line: nuclear background, Solid line: Strong field QED plus nuclear background.[2]

positron production cross section is given by a coherent sum of large number of Feynman diagrams. Theoretical predictions [13] using an adiabatic picture for this vacuum excitation by nuclear motion, is in good agreement with the experimental data as shown in the Fig. 1.6.1(b).

More detailed comparisons between the theory and the experiment is shown in Fig. 1.6.2.[15] This compares the measured positron spectra, integrated over the ion scattering angles $25° < \theta_{lab} < 65°$, with the theory

for four different systems, all involving a uranium projectile. To summarize, the background contributions to the positron production are very well understood.

7. Narrow Lines in the Positron Spectrum

Originally, the search for the spontaneous sparking of the vacuum concentrated on the supercritical collision systems near the coulomb barrier. Even though it was shown that there is a finite probability for K-hole creation in these collisions, the collisions occur over such a short time scale (10^{-21}s), compared to that associated with spontaneous sparking of the vacuum (10^{-19}s), that a natural line width of a few keV is broadened to 300 keV. Thus positrons from the sparking can only add to a dominating background of positrons created by *vacuum shakeoff* and other nuclear processes.

It was a considerable surprise when the EPOS collaboration observed an enhancement of low-energy positron production for U+Cm($Z_u \sim 188$) collisions near the coulomb barrier, at a bombarding energy of 6.05 MeV/amu.[16] In subsequent experiments, the EPOS collaboration discovered an anomalous positron peak (see Fig. 1.7.1(a)) at a center of mass energy, $E_{e^+}^{cm}$ of, 316 ± 10 keV, having a width of ~ 80 keV.[17] As shown by both the dashed line in Fig. 1.7.1, the shape of the unenhanced positron spectrum is reproduced by the dynamic theory based on the *vacuum shakeoff* superimposed on a nuclear background.

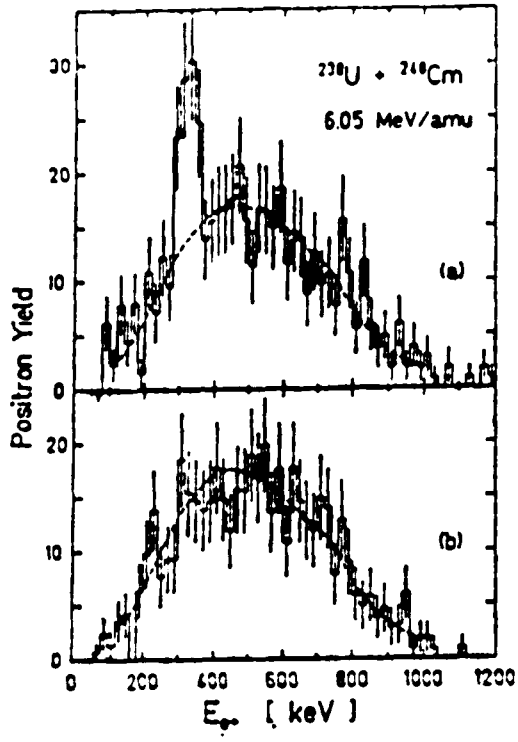

Figure 1.7.1 Positron energy spectra observed for ^{238}U $+^{248}$ Cm collisions at a projectile energy of 6.05 MeV/amu. Kinematic selections overlap preferentially with elastic scattering angles of (a) $100° < \theta_{cm} < 130°$ and (b) $50° < \theta_{cm} < 80°$. Dashed line represent the theoretical distribution for positron production based on Rutherford trajectories together with the nuclear background deduced from γ-ray spectra.[16]

Several interesting features are associated with the observation of this positron line. The presence or absence of the line structure in the spectrum depends critically on the kinematic coincidence requirements for the heavy ion scattering angles. As shown by Fig. 1.7.1(a) it appeared in quasielastic scattering events with the ion scattering angles, $100° < \theta_{cm} < 130°$, whereas, it disappeared with the kinematic selection of $50° < \theta_{cm} < 80°$, as shown by Fig. 1.7.1(b). In addition, the γ-ray and the electron energy distributions

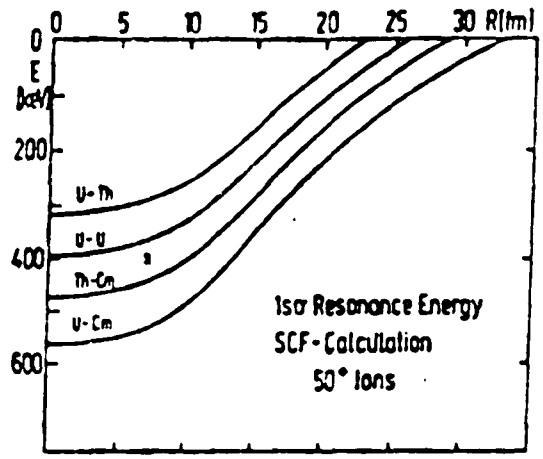

Figure 1.7.2 The location of the 1s resonance as a function of nuclear separation R for the systems U+Th ($Z_u = 182$), U+U($Z_u = 184$), Th+Cm($Z_u = 186$) and U+Cm($Z_u = 188$).[2]

measured simultaneously under identical conditions as the positron peak, do not show any lines, ruling out the final state nuclei as the source of the observed peak. Finally, similar results are also observed in U+U collisions[18] and in U+U and U+Th collisions.[19]

When these peak structures were first observed, it was very tempting to attribute it to the spontaneous sparking. In particular, in the U+Cm system, the peak energy corresponds to the predicted value (1s binding energy minus $2m_ec^2$) for a configuration with the nuclear centers separated by 17 fm (the closest approach for a head-on collision at 6.05 MeV/amu). Since it was

possible to explain the observed intensity, width, and the energy of the peak by means of spontaneous sparking in a small fraction of collisions (10^{-3}), where a giant nuclear quasimolecule is formed with the life time exceeding 10^{-19}s, more systems were systematically studied to gain insight into the process and to verify the predictions such as the Z_u^{20} dependence of the peak energy, as illustrated by Fig. 1.7.2.

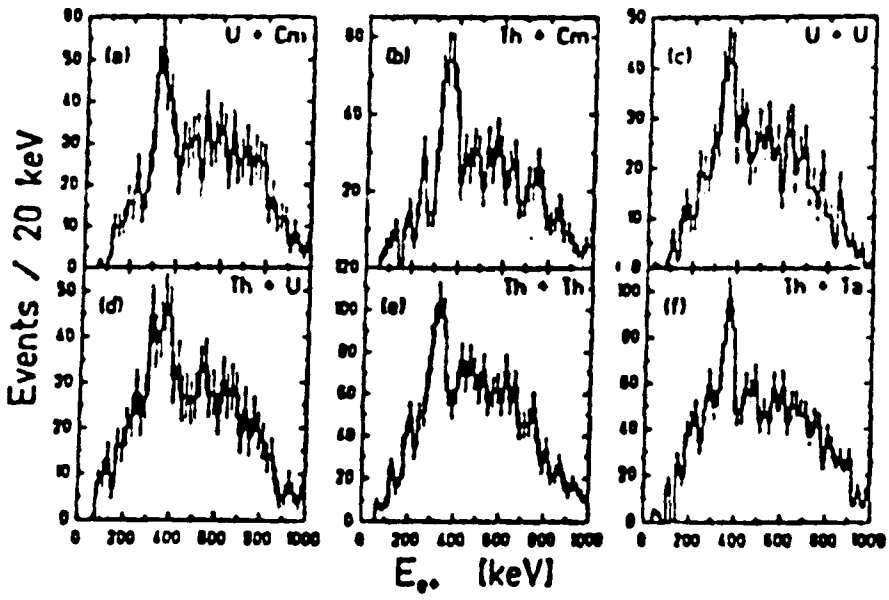

Figure 1.7.3 (a)-(f) Positron spectra from six collision systems.[1]

The EPOS group varied the collision partners from $Z_u = 188$(U+Cm), where positron peak is predicted at $E_{e^+}^{cm} = 300$ keV to $Z_u = 180$(Th+Th), where $E_{e^+}^{cm} = 80$ keV.[2] However the results from these experiments showed

$E_{e^+}^{cm}$ [keV]	FWHM [keV]	Collision system	Z_u	Bomb. Energy (MeV/amu)
238 ± 10	50	U + U	184	5.6, 5.9
250 ± 5	34	U + Ta	165	5.9
261 ± 4	26	Pb + Pb	164	5.7
263 ± 5	24	U + Au	171	5.9
Mean value $= 255 \pm 7$				
277 ± 6^a	65	U + Th	182	5.9
280 ± 6^a	70	U + U	184	5.7, 6.2
313 ± 10	~ 75	U + U	184	5.9
316 ± 10	~ 75	U + Cm	188	6.05
327 ± 10	~ 75	Th + Th	180	5.75
330 ± 4	~ 13	U + Ta	165	5.9
334 ± 10	~ 75	U + Cm	188	6.07
337 ± 4	33	U + Au	171	5.9
348 ± 10	~ 75	U + U	184	5.8
349 ± 10	≥ 100	Th + U	182	5.82
350 ± 5	39	Pb + Pb	164	5.7
352 ± 4	34	U + U	184	5.6, 5.9
354 ± 10	~ 75	Th + Cm	186	6.02
Mean value $= 337 \pm 6$				
375 ± 10	~ 75	Th + Ta	163	5.78
380 ± 10	≥ 80	U + U	184	5.9
409 ± 5	31	U + U	184	5.6, 5.9
Mean value $= 396 \pm 5$				

[a] These values are not included in the determination of mean values.
See Ref. 20 for details.

Table 1.7.1 Survey of the positron line energies observed at GSI.

a positron line at an unvarying energy as shown in Fig. 1.7.3. Moreover, the line persisted in an undercritical system, $Z_u = 163$(Th+Ta), as shown in Fig. 1.7.3(f). Positron line energies observed by the *Orange* spectrometer

group also share a nearly common energy,[10] even though their mean energy is shifted from the EPOS results.

The experimental results from both the EPOS and Orange experiments are summarized in Table 1.7.1. They cluster into 3 groups with mean energies of $255 \pm 7, 337 \pm 6$ and 396 ± 5 keV.[20] Although this grouping is somewhat arbitrary, it is clear that the peak structures occur at more than one energy. The cross sections for the line production is about $10 \mu b/sr$.[1] This corresponds to roughly one positron in every 10,000 collisions and indicates the complexity of the peak separation from the background. In contrast to the behaviour of the line energies, the Orange group found[20] that the line cross sections depended on the combined charge Z_u of the collision system in accordance with the relation $\frac{d\sigma_{e^+}}{d\Omega_{HI}} \propto Z_u^{22 \pm 2}$, where Ω_{HI} denotes the solid angle of the scattered heavy ions. This Z_u dependence is very close to the well established Z_u^{20} dependence for the dynamical positron production, and may be closely connected with the strong electromagnetic field created during the collisions. The width of the peak indicates that the velocity of the emitting source is comparable to the center-of-mass velocity.

8. Monoenergetic Electron-Positron Pair Production

The nearly common peak energies for all of the systems studied suggests a common source for the positron production. One speculation is that these positrons are the product of a two-body decay of a previously unknown object in the mass region 1.6 MeV to 1.8 MeV.[21] An obvious candidate for

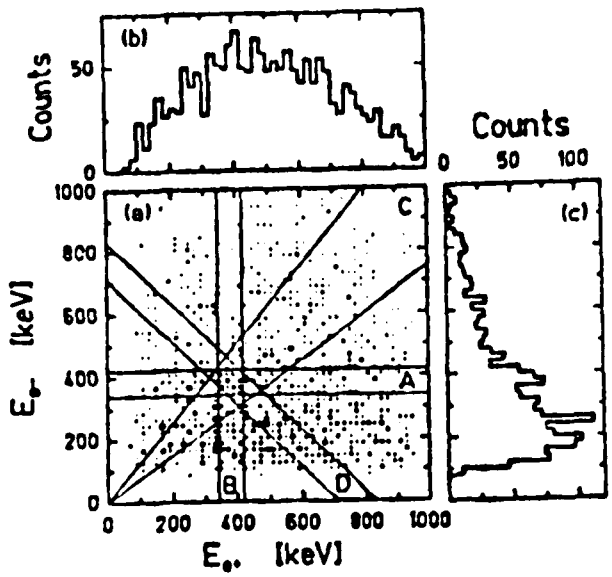

Figure 1.8.1 (a) Intensity distribution of coincidence events as a function of E_{e^+} and E_{e^-} for 5.83 MeV/amu U+Th collisions. (b),(c) Projections of this distribution onto the E_{e^+} and E_{e^-} axes, respectively. Cuts A through D are explained in the text.[1]

the other member of the decay is the electron. Since the positron line-width indicates that the object would have to be at rest in the center-of-mass system, it would emit an electron-positron pair back to back in the center-of-mass system, with each partner having the same energy. The EPOS collaboration was thus led to examine the spectra of the coincident electrons and positrons in two opposite hemispheres. Using a symmetric axial field[1](with respect to the target), the EPOS group discovered the presence of a narrow peak in the energy spectra of the electrons measured in coincidence with the monoenergetic positron line for U+Th collisions at 5.83 MeV/amu.

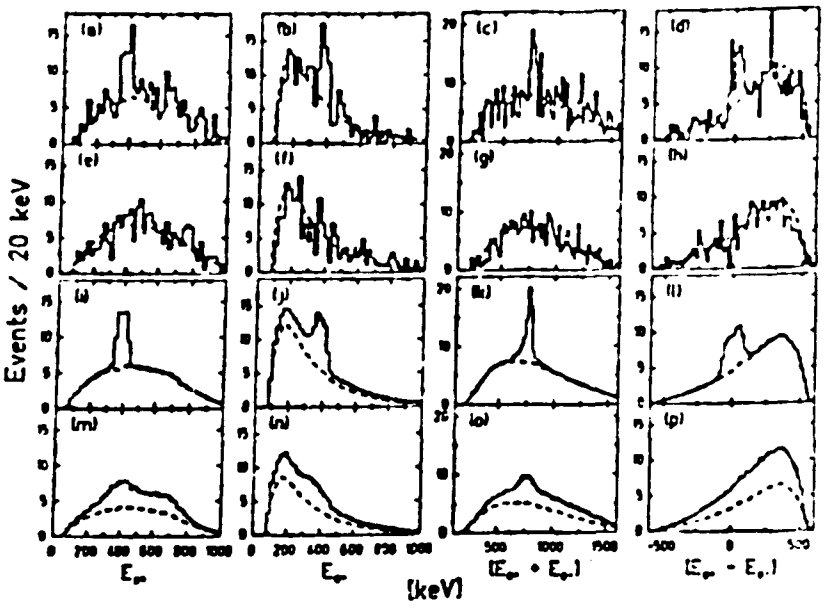

Figure 1.8.2 (a)-(h) Projections of the measured intensity distribution onto E_{e+}, E_{e-}, $E_{e+}+E_{e-}$, and $E_{e+}-E_{e-}$ axes. (i)-(p) Results of Monte Carlo simulations: (i)-(l) for the two-body decay of a neutral particle (scaled by 6×10^{-4}) and (m)-(p) for internal pair conversion of a nuclear state (scaled by 6×10^{-3}). Parts (a)-(d), as well as (i)-(l) and (m)-(p), correspond to the gates labeled A-D in Fig.1.8.1(a), respectively. Parts (e)-(h) are the average of similar gates adjacent to either side of the gates A-D, respectively.[1]

The Fig. 1.8.1(a) shows the scatter plot of electron-positron coincidences as a function of the positron and electron kinetic energies, E_{e+} and E_{e-} respectively. These spectra include all the events measured with the ion scattering angles of 20° to 70° in the laboratory system. Fig. 1.8.1(b) and (c) show the coincidence events projected onto E_{e+} and E_{e-} axes, respectively. The lines through these spectra represent the Monte-Carlo calculations using the shapes for nuclear and atomic contributions, normalized to the total event yield.

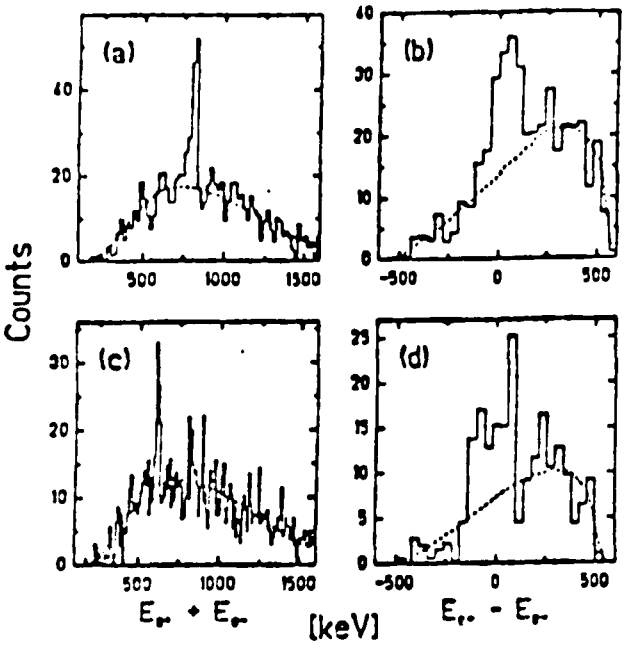

Figure 1.8.3 The sum energy from $e^+ - e^-$ coincidence measurements for U+Th collisions near 5.87 MeV/amu. There are two prominent sum lines at ~ 810 keV and ~ 620 keV.[1]

Fig. 1.8.2(a) shows the positron spectrum in coincidence with the electrons when the electron energy is restricted to the interval $340 < E_{e^-} < 420$ keV (window A). Fig. 1.8.2(b) is the corresponding spectrum with a cut on the positron spectrum (window B). These spectra show peak structures at an energy of 380 ± 15 and 375 ± 15 keV, respectively. The width of the electron peak, 70 ± 15 keV, is similar to the positron peak, 80 ± 15 keV. The lines through the smooth part of the spectra are obtained by Monte-Carlo calculations using the shapes of the dynamical background, and making the appropriate projections after normalizing to the total number of coincidence events. The number of positrons and electrons in the lines are 26.7 ± 7.7

counts and 31.7 ± 7.6 counts, respectively. Fig. 1.8.2(c) shows the spectrum of the energy sum $E_{e+} + E_{e-}$ with the condition $E_{e+} \approx E_{e-}$ (window C), set to allow for the kinematic broadening with the increasing energies. The figure exhibits a line at the sum energy of, 760 ± 20 keV and with a width of, 80 ± 20 keV, which is as narrow as the individual lines, thus suggesting a correlated cancellation of the positron and the electron Doppler shifts. Fig. 1.8.2(d) is the $E_{e+} - E_{e-}$ spectrum with $E_{e+} + E_{e-}$ held constant (window D). A peak appears near zero energy difference. If windows (A-D) are not used, the peak cannot be discovered. Fig. 1.8.2(e)-(h) shows the corresponding spectra with cuts taken adjacent to windows A-D, respectively.

Fig. 1.8.3 shows the high resolution measurements [1] of sum and difference energy spectra for U+Th collisions at a bombarding energy of 5.87 MeV/amu. Two narrow sum energy lines at 620 keV and 810 keV with widths of about 25 keV and 40 keV are clearly visible. They are both much narrower than the individual electron and positron lines. The difference spectra show a much broader peak. Thus the EPOS results clearly establish 3 lines at an approximate electron-positron sum energies of 620, 760, and 810 keV.

Recently, using the double *Orange* spectrometer, Bedermann *et al.*[3] reported e^+e^- coincidence measurements from U+U and U+Pb collisions at 5.9 MeV/amu. Even though the statistical significance of the line structures is rather poor (at a level of 3 standard deviations or less), the measurements provide additional support for some of the EPOS results. The sum lines are

found at 540 ± 16, 640 ± 10, 716 ± 10, 809 ± 8, and 895 ± 10 keV. The most prominent structure is the one at 809 ± 8 keV.

Chapter 2.

The Conjecture of a New Particle or a Composite System

1. Overview

The coincident e^+e^- peaks and the nearly common energies of all the positron peaks observed in the GSI experiments cannot be attributed to the spontaneous sparking of the supercritical system. The results further cannot be explained by any of the known atomic or nuclear processes. Even though, several models were developed[22-23] to explain some of the observations, none of them were able to accommodate all of the observed features. At present there seems to be no convincing explanation for these line structures. The results seem to indicate the production and subsequent decay of several particles or composites (henceforth called X), with an invariant mass in the range of 1.5-1.8 MeV. The limits on the X-particle , from the experimental results, such as, beam dump, heavy meson decays, nuclear level transitions, high precision QED experiments etc. are summarized.

2. The Absence of the Spontaneous Sparking

As we have already seen, the continuous part of the positron spectrum agrees very well with the theoretical prediction for positrons produced in the time varying electromagnetic fields of colliding ions. The models used were also able to reproduce the strong dependence of the continuous background positron production on Z_u (the combined nuclear charge) and the heavy-ion scattering angles.[2] The quantitative agreement between theory and experiment provides great confidence in the formalism, a formalism which predicts the spontaneous sparking of the charged vacuum when Z_u exceeds 173 and which predicts a dramatic shift in the position of the spontaneous positron peak energy as Z_u is varied.

As we noted earlier, the first line structure observed[16] in the $U + Cm$ system created great initial enthusiasm, since it was consistent with the interpretation of the spontaneous decay of the neutral vacuum to the charged vacuum. However, the enthusiasm partially turned to consternation as subsequent measurements showed that the positron peaks were still produced in collision systems for which Z_u was less than 173.[1] Moreover, the positron peak energies remained nearly the same in all the systems studied, demonstrating that the phenomenon is not consistent with the ordinary spontaneous sparking hypothesis. Currently, it is also believed that the time scale available in these collisions is not long enough to induce the spontaneous sparking.[24]

3. Failure of the Conventional Schemes - Atomic and Nuclear Origins

One of the simple explanations proposed to explain the EPOS data is based on the photon pair conversion in the presence of a heavy nucleus. But the positron-electron spectra resulting from the pair conversion are not consistent with the observations, as indicated by Monte-Carlo calculations.[25] In the absence of Coulomb effects, the photon pair conversion probability is nearly a constant, when considered as a function of the energy of the created pair. When the Coulomb effects are added, peak-like structures do emerge in the spectra.[26] However, the Coulomb interaction destroys the symmetry in the positron-electron spectra, with the positron (electron) energy shifted to a higher (lower) value due to the coulomb repulsion (attraction) of the nucleus. For example, in the presence of a Pb nucleus, an incident photon of energy 1.5 MeV, will create a pair in which the positron will share twice the electron energy. Thus a peak in the $E_+ + E_-$ spectrum can be reproduced, whereas the $E_+ - E_-$ spectrum will not show any structure.

A second suggestion of the origin of the line structure involves Zr,[26] a standard fission product of all the EPOS experiments. Both ^{90}Zr and ^{96}Zr have low lying 0-0 transitions that are very close to the EPOS sum lines; namely, the E0 transitions at 1.76 MeV and 1.59 MeV respectively. However, there are many problems with this explanation. Similar to the case of pair conversions, these products cannot reproduce the observed widths and the splitting of the electron-positron lines in the EPOS spectra. The

measurements of the pair conversion spectrum in ^{90}Zr give full-widths-at-half-maximum (FWHM) for both the electrons and the positrons in excess of 150 keV.[27] In addition, due to the coulomb effects, the centroids of the lines are separated about 100 keV. Moreover, in ^{96}Zr, the ratio of the K-conversion intensity to the pair conversion intensity is measured to be 2.38 ± 0.08. A K-conversion electron line is simply not found in the EPOS electron spectrum. There is an additional inconsistency associated with the lifetime of the Zr E0 transition (38 and 62 nsec in ^{90}Zr and ^{96}Zr respectively).[28] Since the source of the line structures travels with the center-of-mass velocity and hence takes only 1 nsec to cover the detector fiducial volumes, and since the produced e^+e^- pair has a time of flight of less than 10 nsec, a Zr fragment will not have enough time to decay and produce a signal in the EPOS spectrometer. In fact, no Zr component is detected among the heavy ion fragments in coincidence with the electron-positron pairs contributing to the peak structures.

Another group of suggestions involve models which predict that the electron-positron pair may not be the result of a single decay, but rather a sequential decay in a cascade process.[1] For example, if a positron conversion is uniquely preceded or followed by an internal electron conversion, two coincident peak structures will be observed. However, such a scheme fails to explain the observed widths and the nearly common energies of the electron and the positron lines. Moreover, the absence of any correlation between the positron and the electron emission angles in a sequential decay would result in a broad sum-energy peak, contradicting the GSI observations.

Yet another attempt to explain the positron peaks is based on atomic process.[29] In this model, the multiple vacancies in the molecular outer shells of the combined system are transferred to the inner shells, at relatively large intermolecular distances, of the order of 500 fm. These vacancies are filled from the positron continuum as in the original scheme and thus induce the positron emission. However, this scheme has the obvious difficulty of explaining the width of the positron peaks and the independence of the positron peak energy on the colliding partners. In addition, it fails to reproduce the coincident electron lines.

The vibrational modes of the quasimolecule formed during the collision were also considered[30] as a possible source of the observed electron-positron pair. If two classical charge distributions are examined along the line joining the two nuclei an oscillation of the nuclear surface about a spherical shape can be generated with the nuclei touching at one point. If the time-dependent part of the electromagnetic field of the vibrating nucleus is then treated as a perturbation, the pair creation probability can be estimated. Multiple electron-positron peaks with some of the observed features such as the soft Z-dependence of the peak energies, the production of the pair by the subcritical systems, and the absence of any competing γ-ray emissions, are thus reproduced. Unfortunately, such an approach fails for the following reasons: First, for softer Z-dependence of the peak energies, the model requires long-lived quasimolecules, for example, with a life time of 5×10^{-16} s for a combined charge of 163. In comparison, the Rutherford scattering time for the heavy ion collision is $\sim 10^{-21}$ s. Second, even though there is a preferred

direction (the line joining the two nuclei), the model cannot reproduce the observed angular correlation between the electron and the positron. Finally, the model simply fails to reproduce the equality of the energies in the electron and the positron lines.

4. The Particle Scenario

All of the observed features of the GSI experiments seem to suggest that the positron-electron lines are emitted by a common source X, produced essentially at rest in the center-of-mass system of the colliding ions. Moreover, the combined results of the EPOS and the ORANGE groups point toward the existence of several such systems all falling within the energy range of 1.5-1.8 MeV. Let us therefore consider on purely kinematic grounds the probability of producing a GSI positron-electron spectrum from the decay of an unknown neutral X particle ($X \longrightarrow e^+e^-$).[31]

First we note that we would observe a monochromatic positron spectrum only if the particle is produced at rest in the laboratory reference frame. In actuality the X-particle would probably be created with a broad energy distribution in the center of mass system of the colliding nuclei. Hence, the decay products would acquire a Doppler broadening. Additional broadening of the spectra will occur when the decay products are boosted from the center-of-mass frame to the laboratory frame.

If the production and the subsequent decay of the X-particle are isotropic in the center-of-mass frame, the corresponding positron spectrum in the center of mass system is given by

$$\frac{dw}{dE'_+} = \frac{m_X}{\sqrt{m_X^2 - 4m_e^2}} \int_{E_1}^{E_2} dE_X \frac{1}{\sqrt{E_X^2 - m_X^2}} \frac{dw}{dE_X}, \tag{2.4.1}$$

where

$$E_{1,2} = \frac{M_X}{2m_e^2}\left[E'_X m_X \pm (E'^2_+ - m_e^2)^{1/2}(m_X^2 - 4m_e^2)^{1/2}\right]. \tag{2.4.2}$$

The variables E_X and E'_+ are respectively the center-of-mass energies of the X-particle and the positron, and $\frac{dw}{dE_X}$ is the production spectrum of the X-particle in the center-of-mass frame. The expression given by Eq. (2.4.1) must be boosted to the laboratory frame for comparison to the observed spectrum. The transformation is

$$\frac{dw}{dE_+} = \frac{1}{2}\int d(cos\theta)\frac{p_+}{p'_+}\frac{dw}{dE'_+}, \tag{2.4.3}$$

where E_+, the laboratory positron energy is related to E'_+ by $E'_+ = \gamma(E_+ - \beta p_+ cos\theta)$ with $\gamma = (1-\beta^2)^{-1/2}$, and $\beta = (v_{cm}/c)$, v_{cm} being the velocity of the center-of-mass system. The variables p_+ and p'_+ represent the positron momenta in the laboratory frame and the center-of-mass frame, respectively.

In Ref. 31, the shape of the resulting spectrum is examined in detail. Since the production mechanism is not known, it is difficult to guess a correct functional form for $\frac{dw}{dE_X}$. However, an exponentially decaying function of the form

$$\frac{dw}{dE_X} \simeq \frac{1}{\Gamma} e^{-(E_X - m_X)/\Gamma}, \tag{2.4.4}$$

with a decay constant, Γ in the range of 100 to 1000 keV produces positron spectra with half widths in the range of 250 to 700 keV for a mass $m_X = 1.68$ MeV. Another function

$$\frac{dw}{dp_X} \simeq \frac{1}{\Gamma} e^{-p_X/\Gamma}, \tag{2.4.5}$$

which weights the low momentum side more, produces spectra with widths between 70 and 130 keV for the same range of values of Γ. Hence, the second function can reproduce a narrow positron line. However, it is difficult to explain how such an enhancement of X-particle with low momentum component will occur during the production process.

Another way to create a narrow positron spectrum is to assume a long lifetime for the X-particle, so that most of decays occur outside the detector volume. In such a case, the observed positron spectrum would be dominated by decays from the slowly moving particles. For a sufficiently long lifetime, $\tau_X \sim 10^{-8}$s, a sharp positron spectrum could then be reproduced,[31] at the expense of course, of a reduced signal in the detector.

It is perhaps the observation of several peaks that makes a new elementary particle picture most difficult to explain. The EPOS results it should be remembered, suggest that more than one neutral state is in fact formed. Moreover, the states must survive until the background fields of the colliding nuclei cease to exist. Otherwise, with Z $\sim$ 90, for example, a Coulomb energy separation ΔE, of more than 20 keV between the electron and the positron lines would be produced if the decay occurred at a distance less than $r = \frac{2Ze^2}{\Delta E} \approx 6500$ fm from the nucleus. Constrained by the observed

width of the sum energy peak and the acceptance of the detector volume, the lifetime of the X-particle must actually lie between 10^{-19} and 10^{-9}s.

5. Model-Dependent Constraints on the Particle

There are several experiments, which set severe constraints on a hypothetical neutral X-particle in the mass range covered by the GSI results. In this section we will summarize some of these published results, which depend on a specific model for the coupling of the particle to the leptons and the quarks.

When the first electron-positron sum energy line was reported,[1] much attention was initially devoted to the long sought-after axion. The postulated existence of an axion follows from a cure for strong CP and P violations occurring in QCD. Originally suggested by Peccei and Quinn, the cure introduces a global $U_{PQ}(1)$ symmetry to the QCD Lagrangian,[32] which in turn requires two Higgs-field doublet ϕ_1 and ϕ_2 coupled to the up and down quarks. The axion is the Goldstone boson associated with the spontaneous symmetry breaking of this new symmetry.

The axion mass can be estimated as[33]

$$m_X \simeq 75 \left(x + \frac{1}{x} \right) \text{ keV}, \tag{2.5.1}$$

where x is the ratio $\frac{<\phi_1>}{<\phi_2>}$ of the vacuum expectation values of the Higgs fields. The axion couplings to quarks and the electrons are given by

$$\frac{m_q}{f} i \bar{q} \gamma_5 q X \begin{pmatrix} x \\ \frac{1}{x} \end{pmatrix} \qquad \begin{pmatrix} \text{for up quarks} \\ \text{for down quarks} \end{pmatrix} \tag{2.5.2}$$

and

$$\frac{m_e}{f} i\bar{e}\gamma_5 eX \frac{1}{x} \qquad \text{for electron} \tag{2.5.3}$$

where, q, e, and X respectively denote quark, electron, and axion wave functions, m_q and m_e are the quark and the electron masses, and f is defined by $f = \sqrt{f_1^2 + f_2^2}$ with $f_i = \sqrt{2} < \phi_i >$. If a mass is assigned to the axion, the coupling strengths of the axion to the lepton and the quark sectors are thus fixed.

The existence of a standard axion is ruled out[26] by the experiments which searched for the radiative decay of heavy vector mesons, $V \longrightarrow \gamma + X$, where V is either J/ψ or Υ. Such experiments looked for a high-energy photon along with an axion decay product of e^+e^- or $\gamma\gamma$ pair. Since the J/ψ decay rate is proportional to x^2 and the Υ decay rate is proportional to x^{-2}, it is clear that a non-observation[34] of these decays, rules out a large range of x values.

A bound independent of the parameter x can be clearly obtained[26] from the product of the branching ratios for the J/ψ and Υ decays. Theoretically the product $P = B(J/\psi \longrightarrow \gamma X)B(\Upsilon \longrightarrow \gamma X)$ can be estimated[26] to be 1.6×10^{-8}. Experimentally, however, a value of $P < 10^{-9}$ is found, in clear conflict with the theoretical estimate. It should be noted, however, that the experimental searches were not sensitive to particles with lifetimes shorter than 10^{-13}s, since such particles would decay before reaching the sensitive regions of the detector volume. On the other hand, a short-lived axion requires a small value of x (~ 0.04), which implies a small value for the vacuum expectation value for one of the Higgs fields. This in turn forces the

axion to be coupled strongly to the b quark, thereby increasing the branching ratio for $\Upsilon(1S) \longrightarrow \gamma X$ and making it the dominant decay mode of Υ. The decay products, $\gamma e^+ e^-$, would then exceed the observed QED background by two orders of magnitude. The results of some of the vector meson experiments are summarized in Table 2.5.1. All of them rule out the standard axion.

There are models[35] with short-lived variant axions which can survive the above limits. These models have a suppressed coupling to the b and c quarks and an enhanced coupling to the electrons (which produces a fast decay). The models retain the $U_{PQ}(1)$ symmetry only for u and d quarks. However, the variant axions associated with these models cannot survive the limits provided by other experiments which we will now review. (It should be noted that the limits of these experiments apply to other short-lived neutral particles as well.)

The SINDRUM collaboration searched[36] for the decay $\pi^+ \longrightarrow e^+ \nu X$ with a subsequent decay $X \longrightarrow e^+ e^-$. Decay of pions by this mode will have a phase space enhancement over the standard decay $\pi \longrightarrow \pi^0 e^+ \nu$. The non-observation of this decay at a level of 10^{-10} is in strong contradiction to the theoretical prediction of 2×10^{-6} for models with short-lived variants.

Muon decays were examined[36,37] for the evidence of the inclusive process $\mu^+ \longrightarrow e^+ X$. In ordinary muon decay, $\mu^+ \longrightarrow e^+ \nu_e \bar{\nu}_\mu$, the positron energy spectrum is continuous. The decay, $\mu^+ \longrightarrow e^+ X$, by contrast, would produce an e^+ at a fixed positron kinetic energy. Searches for peaks in the positron spectrum revealed no candidates for this process.

If the X-particle couples to the light quarks significantly, it will be similar to the flavor changing weak neutral current interactions. An experiment designed to explore the 1.8 MeV mass region should therefore be sensitive to very low energy e^+e^- pairs. One experiment[38] performed in the late 1960's, $\Sigma^+ \longrightarrow pe^+e^-$, fortuitously had superb sensitivity in the low e^+e^- mass region with virtually no background present. Three events were indeed observed with e^+e^- invariant masses of (1.4 ± 1.0) MeV, (1.6 ± 1.2) MeV, and (1.9 ± 1.2) MeV. Unfortunately, even though the masses lie in the region of interest, they are consistent with the expected rates for the process, $\Sigma^+ \longrightarrow p\gamma \longrightarrow pe^+e^-$. The limit for the branching ratio of the process $\Sigma^+ \longrightarrow pX$ is less than 7×10^{-6}.

Another process that can produce a light pseudoscalar particle is the rare decay mode of K-mesons, $K^+ \longrightarrow \pi^+X$. A search for this process,[39] for a lifetime shorter than 10^{-13}s, gave an upper limit of 4.5×10^{-7} for the branching ratio.

It is also possible to look for a light neutral particle by examining the decay of an excited nuclear state $|J_1^{P_1}T_1>$ to its ground state $|J_2^{P_2}T_2>$. Here J, P, and T denote the spin, parity, and isospin of the nucleus respectively. If such deexcitations proceed by the emission of a light pseudoscalar particle, the particle will carry away $J^P = 0^-, 1^+, 2^-, 3^+, \ldots$. The calculation of the decay process is similar to that for photon decay and can be performed in a lowest order perturbation theory,[32] provided the coupling is weak. Table 2.5.1 contains entries for three decay experiments which gave negative

Process	Upper* limits
$B(\Upsilon \to \gamma X)B(X \to e^+e^-)$	10^{-3}
$B(J/\psi \to \gamma X)$	1.4×10^{-5}
$\Gamma(\pi^+ \to e^+\nu X)$	10^{-9}
$\Gamma(\mu \to eX)/\Gamma(\mu \to e\nu\bar{\nu})$	2.6×10^{-6}
$B(\Sigma^+ \to pX)B(X \to e^+e^-)$	7×10^{-6}
$B(K^+ \to \pi^+X)B(X \to e^+e^-)$	4.5×10^{-7}
$^6Li(0^+, 3.562\text{MeV}), \Gamma_X/\Gamma_\gamma$	9×10^{-4}
$^{13}C(\frac{3}{2}^-, 3.680\text{MeV}), \Gamma_X/\Gamma_\gamma$	7×10^{-5}
$^{14}N, ^{16}O, ^8Be$ Decays	1×10^{-2}

* See the text for references.

Table 2.5.1 Summary of the decay limits on a light neutral particle. Some of these results put limits on axions as well. Here, B stands for the branching ratio and Γ for the partial decay width.

results. It should be noted however that these experiments provide no limits for a particle which couples only to electrons and photons.

6. Model-Independent Constraints on the Particle

Some of the most stringent limits on a particle scenario are provided by beam dump experiments.[40-43] A beam of electrons or protons is stopped in a dense target which absorbs all of the incident energy. (See Fig. 2.6.1(a) for a schematic of such an experiment.) The dump length is chosen to be equal to several radiation lengths in order to reduce the background arising from the "punch-through" of incident particles. A particle can be produced by electron or muon Bremsstrahlüng (Fig. 2.6.1(b)) and by Primakoff processes (Fig. 2.6.1(c)). Since only the mass and the decay width for the X-particle are needed to compute[26,44] the cross sections, the production rate is model independent for all $X \longrightarrow e^+e^-, \gamma\gamma$ processes.

The results from the electron and the proton beam dump experiments are summarized in Table 2.6.1. The excluded domain in the mass-lifetime plane is shown in Fig 2.6.6. Taken together, these experiments set an upper limit of about 10^{-14}s on a particle of mass 1.8 MeV. They cannot place a limit on a very short-lived neutral particle, since such a particle would decay inside the dump.

One of the arguments against the validity of beam dump searches is that the neutral particle could interact and decay within the dump. The argument is specious, however, as shown by the analysis of Riordan *et al.* [42]. In their experiment, carried out at SLAC, the X-nucleon cross section has to be at least of the order of 50 mb for the signal not to show up in the detector. This value is comparable to the size of the π-p cross section,

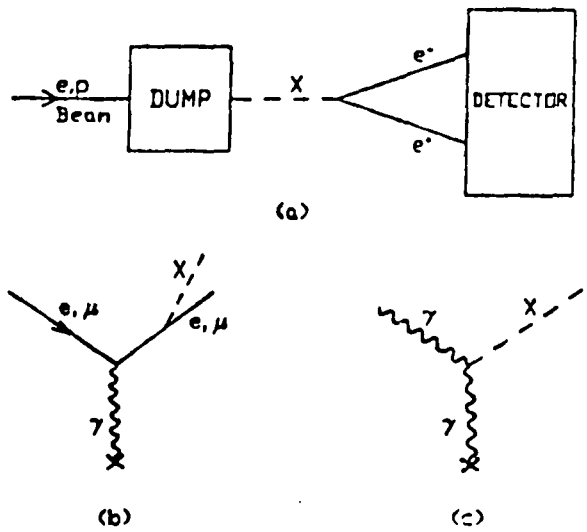

Figure 2.6.1 (a) A schematic of a beam dump experiment. The particle production processes in such an experiment are the (b) electron or muon Bremsstrahlung and the (c) Primakoff production.

and hence would have dominated the long range part of the nucleon-nucleon interaction (caused by the lighter X-particle exchange as compared to π-meson exchange). A comparison of the X-nucleon coupling to the pion-nucleon coupling, leads to an X-nucleon cross section of 1 μb, a value that is far too small to have any effect on the SLAC beam dump results.

Now we will turn to the low-energy precision experiments. Since the mass of the proposed particle is small, it must contribute to virtual processes in QED in a measurable way. Experimental studies of Delbrück scattering (the scattering of photons in a nuclear field), the positronium hyperfine

Energy(GeV) Beam Particle	Dump length (m)	τ_X Range excluded (s)
2.5, e^-	2.4	$5 \times 10^{-13} - 1 \times 10^{-7}$
1.5, e^-	0.1	$6 \times 10^{-11} - 9 \times 10^{-4}$
9.0, e^-	0.1	$1 \times 10^{-14} - 5 \times 10^{-11}$
800, p	5.5	$1 \times 10^{-14} - 1 \times 10^{-11}$

Table 2.6.1 The summary of the beam dump experiments searching for a light, axion-like particle decaying into e^+e^-.

level splitting, the H-lamb shift, and the anomalous magnetic moment of the electron and the muon, will then produce bounds on the particle scenario. Although we will examine all four of the studies we will emphasize the g-2 constraint on the lifetime, since we will eventually rely on it to establish the expected rates for the particle production in the e^+e^- scattering experiments.

Delbrück scattering sets limits on the two-photon couplings of a scalar and pseudoscalar boson. The process is described by the Lagrangians[45]

$$g_s(E^2 - B^2)X, \qquad \text{for a scalar boson,} \qquad (2.6.1)$$

and

$$g_p(E \cdot B)X, \qquad \text{for a pseudoscalar boson,} \qquad (2.6.2)$$

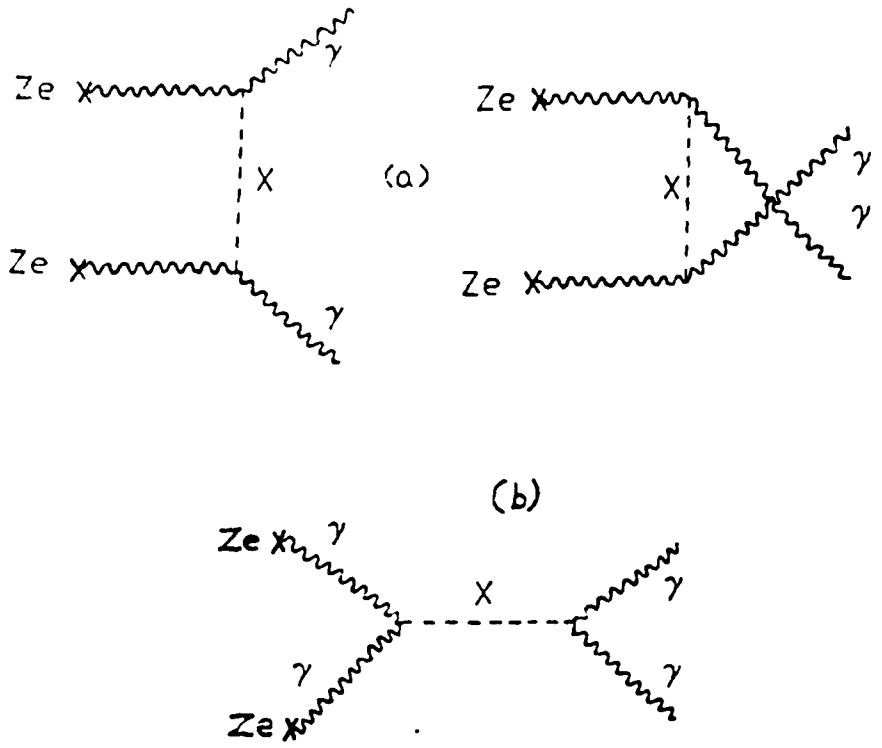

Figure 2.6.2 The Feynman diagrams contributing to the Delbrück scattering. For a pseudoscalar coupling the contribution comes from the diagram (b) alone.

where g_s and g_p are the coupling constants. The Feynman diagrams for these processes are shown in Fig. 2.6.2. Fig. 2.6.2(b) contributes only to the pseudoscalar case. In Ref. 45, the contributions to the cross section from the pseudoscalar and the scalar couplings are calculated. A bound on the coupling, results from the demand that the contribution not exceed the observed cross section. Experimental data for Delbrück scattering off uranium, results in the bounds $g_p < (2GeV)^{-1}$ and $g_s < (50GeV)^{-1}$. It should be remembered that there are analogous photon exchange diagrams

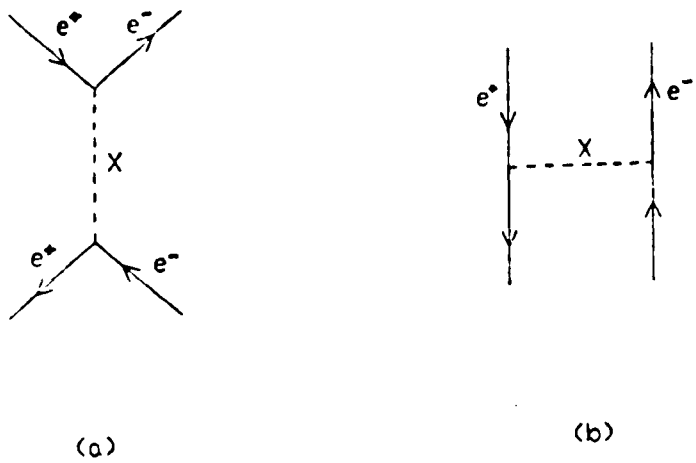

Figure 2.6.3 The s-channel and the t-channel contributions to the positronium hyperfine level splitting.

contributing to the cross section. Hence, in a more realistic calculation there will be interference terms, which will lower these bounds even further.

The positronium hyperfine splitting[45,26] is also modified by the existence of a light particle. A pseudoscalar particle will contribute only to the singlet state ($J^P = 0^-$), while a vector particle will influence only the triplet ground state ($J^P = 1^-$). Both particles will mix through the s-channel diagram shown in Fig. 2.6.3(a) when the spin-parity quantum numbers of the X-particle agrees with the corresponding positronium level. The t-channel diagram (Fig. 2.6.3(b)) contributes to all of the positronium states equally

and hence will not change the level spacings. The diagram in Fig. 2.6.3 gives rise to the following matrix element

$$M = \frac{g^2}{m_X^2 - 4m_e^2} A - \frac{g^2}{m_X^2} B, \tag{2.6.3}$$

where $A = (\bar{v}\Gamma u)(\bar{u}\Gamma v)$ and $B = (\bar{v}\Gamma v)(\bar{u}\Gamma u)$ with $\Gamma = 1, i\gamma_5, \gamma_\mu, \gamma_\mu\gamma_5$ corresponding to spin-parity assignments of $0^+, 0^-, 1^-, 1^+$ for the neutral state X. The variables u and v are the spinors for the electron and the positron respectively, and g is the X-electron coupling constant. In the non-relativistic limit A and B are given by

$$\begin{aligned}
&J^P(X) = 0^+, \quad A = 0, && B = -1, \\
&J^P(X) = 0^-, \quad A = \frac{1}{2}(1 - < \sigma_1 \cdot \sigma_2 >), && B = 0, \\
&J^P(X) = 1^-, \quad A = -\frac{1}{2}(3 + < \sigma_1 \cdot \sigma_2 >), && B = 1, \\
&J^P(X) = 1^+, \quad A = \frac{1}{2}(1 - < \sigma_1 \cdot \sigma_2 >), && B = < \sigma_1 \cdot \sigma_2 > .
\end{aligned} \tag{2.6.4}$$

For the positronium singlet and triplet states, $< \sigma_1 \cdot \sigma_2 >$ takes the values of -3 and $+1$, respectively. The agreement between the QED prediction and the experimental results[46] for the hyperfine level splitting can be stated as

$$|\Delta E_{exp} - \Delta E_{th}| < 10\ MHz, \tag{2.6.5}$$

resulting in a bound on the coupling constant g. For $m_X = 1.7$ MeV, for example, we obtain[45] for $J^P = 0^-, 1^-$, and 1^+

$$\frac{g^2}{4\pi} < 10^{-6}, \quad J^P = 0^-, 1^-, \tag{2.6.6}$$

and

$$\frac{g^2}{4\pi} < 7 \times 10^{-6}, \quad J^P = 1^+. \tag{2.6.7}$$

We cannot obtain a limit for the scalar coupling ($J^P = 0^+$) since the shift due to the scalar coupling is identical for both the positronium levels.

If we assume that the particle is created through the nuclear (or quark) current during the heavy ion collisions with a subsequent decay to e^+e^-, the atomic binding energies are also modified by the same coupling. Hence we can use some of the known atomic properties to set bounds[47] on the combined coupling constants $g^p g^e$ and $g^n g^e$, where g^p, g^n, and g^e are the particle-proton, the particle-neutron, and the particle-electron coupling respectively.

The experimental value for the Lamb shift (the $2S_{1/2} - 2P_{1/2}$ level splitting) in hydrogen,[48] $\Delta E = 1057845 \pm 9$ kHz, agrees with the theoretical prediction[4] to within 30 kHz. From this agreement a limit of $g^e g^p < 2 \times 10^{-8}$ can be deduced[47] for the combined coupling constant. In muonic atoms, the transition energies between high-lying levels ($5g_{9/2} \rightarrow 4f_{7/2}$ in μPb for example) agree with QED predictions to within 10 eV,[49] leading to a limit of $g^\mu g^{p/n} < 10^{-7}$, where $g^{p/n}$ represents an average of g^p and g^n.

The limits provided by the atomic processes all apply to the product of g^e and $g^{p,n}$. Although the coupling constant $g^{p/n}$ can be estimated to be $\sim 10^{-4}$ from the GSI results for the production cross section of the positron lines, the coupling constant g^e can take on much smaller values. Hence the atomic results are really of limited utility for setting any stringent upper bound on the particle couplings.

One of the most quoted success stories of QED is the agreement between the theoretical predictions and the experimental results of the anomalous magnetic moment of the electron[6] and the muon.[50] These results can be used to provide a bound on the particle-lepton coupling constants g_i^e and g_i^μ. The subscript i specifies the different couplings: Scalar(S), Pseudoscalar(P), Vector(V) and Axialvector(A).

The Dirac theory treats a lepton as a point particle and predicts a magnetic moment of $\mu_B = \frac{e\hbar}{2mc}$, where m is the corresponding lepton mass. The magnetic moment $\vec{\mu}$ is related to the spin vector $\vec{s}$ by

$$\vec{\mu} = g\mu_B \vec{s},$$

where $g\mu_B$ is known as gyromagnetic ratio and g is called the Landé g-factor (not to be confused with the coupling constant introduced earlier). According to Dirac theory, a point-like spin-1/2 particle will have a g-factor of 2. The measured value of the g-factor differs from this prediction by 0.2%, and is attributed to the virtual photon cloud surrounding the electron.

The Fig. 2.6.4(a) shows all the virtual processes to be considered (to the order α^2) to account for the deviation. By summing the contribution from each of these diagrams, the magnetic moment of a lepton can be calculated. For the electron, by summing terms to the order of α^4, Kinoshita has calculated[6] the theoretical g-value anomaly, a_e^{th}:

$$a_e{}^{(th)} \equiv (\frac{g-2}{2}) = 1\ 159\ 652\ 263(22)(104) \times 10^{-12}. \qquad (2.6.8)$$

The first uncertainty (22) is due to the error estimated in the calculation and the second uncertainty (104) is due to the propagated uncertainty in the

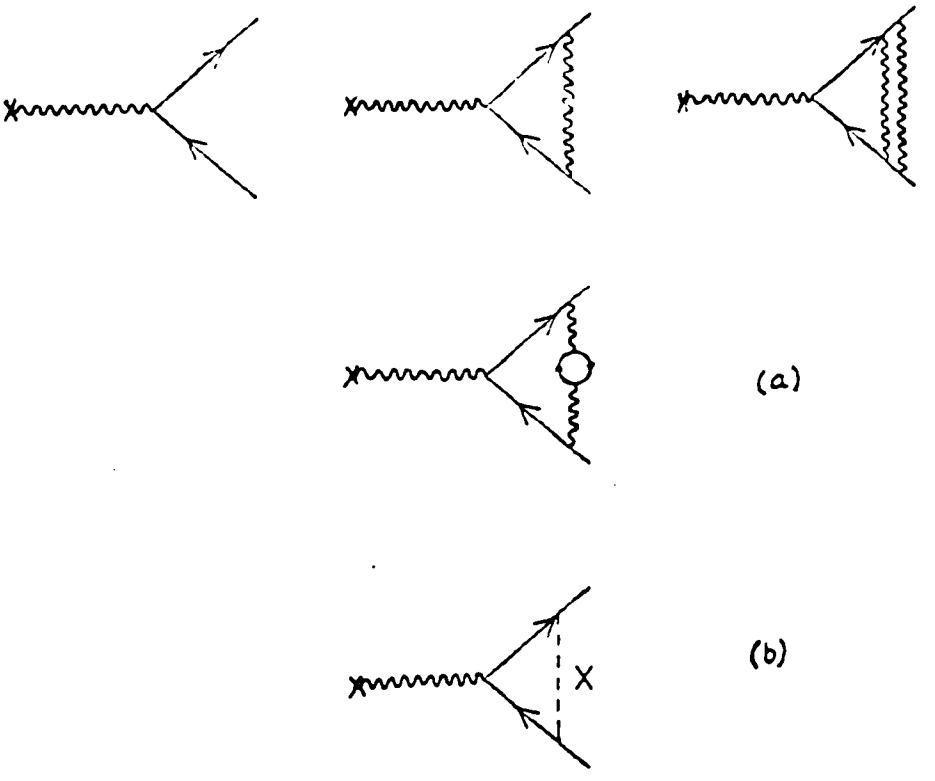

Figure 2.6.4 Feynman diagrams for (a) the QED radiative corrections of the magnetic moment of a lepton (to the order of α^2) and (b) the first order correction to the photon-lepton vertex from the virtual X exchange. Straight line: lepton, broken line: X, curly line: photon.

fine structure constant,[51] $\alpha^{-1} = 137.0359815(123)$. Eq. (2.6.8) includes the contributions from the lepton ($\mu^{\pm}$ and $\tau^{\pm}$) loops, the hadronic effects, and the weak interactions. The latest experimental value[52] for the anomaly is

$$a_e^{(exp)} = 1\ 159\ 652\ 193(4) \times 10^{-12}. \qquad (2.6.9)$$

In the case of the muon, due to its larger mass, the anomaly is more sensitive to the physics at short distances. Hence, the contributions from the virtual hadronic processes and the virtual weak processes are substantial. For muons also, the calculations are carried out[50] to order α^4:

$$a_\mu^{(th)} = 11\ 659\ 202(20) \times 10^{-10}. \tag{2.6.10}$$

The experimental value from CERN muon storage ring is[53]

$$a_\mu^{(exp)} = 11\ 659\ 240(85) \times 10^{-10}. \tag{2.6.11}$$

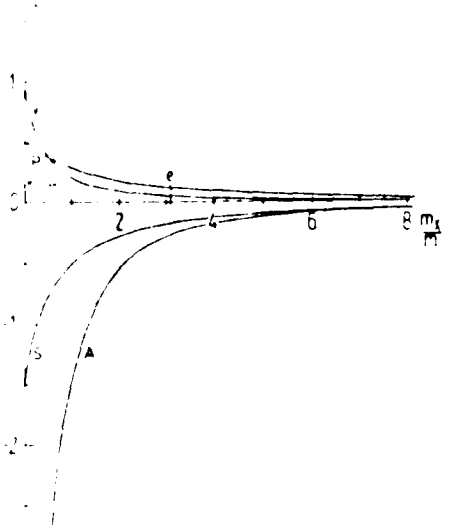

Figure 2.6.5 The coefficients $K_i(m_X/m)$ describing the contribution from a new particle-lepton coupling to the anomalous magnetic moment of a lepton of mass m. (See Ref. 31 for details.)

We know from the above discussions that, the anomalous magnetic moment of leptons are measured with great precision and that the theoretical predictions agree with them to an exceedingly high accuracy. A light particle coupling to the leptons will contribute to the g-2 factor through the Feynman graphs shown in Fig. 2.6.4(b). In Ref. 31 the contributions from the various X-lepton couplings are calculated. The electron or the muon anomaly can be expressed as

$$a_{e,\mu} = a_{QED} + a_{had} + a_{weak} + \Delta a_i^{e,\mu} = a_{e,\mu}{}^{(th)} + \Delta a_i^{e,\mu}, \qquad (2.6.12)$$

where $\Delta a_i^{e,\mu}$ is the first-order radiative correction to the anomalous magnetic moment from the new particle of type i, with i = S, P, V, and A. It can be shown that Δa_i^l can be written as

$$\Delta a_i^l = \left(\frac{\alpha_i^l}{2\pi}\right) K_i(m_X/m) \qquad (2.6.13)$$

with

$$\begin{aligned}
K_S &= -\Big[\frac{3}{2} - \rho + \frac{1}{2}\rho(\rho-3)\ln\rho - (\rho^2 - 5\rho + 4)F(\rho)\Big], \\
K_P &= +\Big[\frac{1}{2} + \rho - \frac{1}{2}\rho(\rho-1)\ln\rho + \rho(\rho-3)F(\rho)\Big], \\
K_V &= +\Big[1 - 2\rho + \rho(\rho-2)\ln\rho - 2(\rho^2 - 4\rho + 2)F(\rho)\Big], \\
K_A &= -\Big[-9 + 2\rho - (\rho^2 - 6\rho + 4)\ln\rho + 2(\rho^2 - 8\rho + 14)F(\rho)\Big],
\end{aligned} \qquad (2.6.14)$$

where $F(\rho)$ denotes the function

$$\begin{aligned}
F(\rho) &= \Big[\frac{\rho}{(\rho-4)}\Big]^{\frac{1}{2}} \mathrm{Arth}\Big[\frac{(\rho-4)}{\rho}\Big]^{\frac{1}{2}} \qquad \text{for } \rho > 4, \\
F(\rho) &= \Big[\frac{\rho}{(4-\rho)}\Big]^{\frac{1}{2}} \arctan\Big[\frac{(4-\rho)}{\rho}\Big]^{\frac{1}{2}} \qquad \text{for } \rho < 4,
\end{aligned} \qquad (2.6.15)$$

i	S	P	V	A
$\alpha_i^e <$	7×10^{-9}	1×10^{-8}	3×10^{-8}	5×10^{-9}
$\alpha_i^\mu <$	4×10^{-8}	10^{-7}	7×10^{-8}	3×10^{-9}
$\tau_X^i >$	$2 \times 10^{-13} s$	$1 \times 10^{-13} s$	$4 \times 10^{-14} s$	$5 \times 10^{-13} s$

Table 2.6.2 The upper bounds on X-electron and X-muon coupling constants α_i^e and α_i^μ, for i = Scalar, Pseudoscalar, Vector, and Axial vector. Also listed is the corresponding lower bounds on the lifetime, τ_X of the new particle assuming a mass of 1.8 MeV for X.[31]

and $\rho = (m_X/m)^2$. The symbol α_i^l denotes the new particle-lepton coupling constant, where l denotes the leptons ($l = e, \mu$). We reproduce the plot[31] for these functions in Fig. 2.6.5 to show the contributions from the coefficients. Also indicated in the figure are the values of (m_X/m) for the case of the electron and the muon, when $m_X = 1.68$ MeV.

The agreement between the theory and the experiment (see Eqs. 2.6.8, 2.6.9, 2.6.10, 2.6.11) for the anomalous magnetic moment gives the following upper bounds for $\Delta a_i^{e,\mu}$:

$$\Delta a_i^e < 3 \times 10^{-10} \tag{2.6.16}$$

and

$$\Delta a_i^\mu < 1 \times 10^{-8}. \tag{2.6.17}$$

Using the values for the coefficients $K_i(m_X/m)$ from Fig. 2.6.5 and the above upper bounds, we can estimate bounds on the allowed values for the coupling constants as shown in Table 2.6.2. These bounds can then be used to deduce lower limits for the lifetime τ_X^i of the X-particle. Since the decay width for the process $X \longrightarrow e^+e^-$ can be expressed as[54]

$$\Gamma^{(i)} = m_X \alpha_i^e f_i(\rho), \tag{2.6.18}$$

where

$$\begin{aligned} f_S(\rho) &= \frac{1}{2}\frac{(\rho-4)^{3/2}}{\rho}, \\ f_P(\rho) &= \frac{1}{2}(\rho-4)^{1/2}, \\ f_V(\rho) &= \frac{1}{3}\frac{(\rho-4)^{1/2}(\rho+2)}{\rho}, \\ f_A(\rho) &= \frac{1}{3}\frac{(\rho-4)^{3/2}}{\rho}, \end{aligned} \tag{2.6.19}$$

the lifetime of the X-particle is given by

$$\tau_X^i = \frac{\hbar}{\Gamma^{(i)}} = \frac{\hbar}{m_X \alpha_i^e f_i(\rho)} \simeq \frac{7.9 \times 10^{-22} s}{\alpha_i^e f_i(\rho)}. \tag{2.6.20}$$

The limits on the lifetime are listed in Table 2.6.2.

The excluded regions for a light particle in the mass-lifetime plane using the beam dump and the g-2 results are shown in Fig. 2.6.6. In each case, the excluded regions are to the left of the curve. The figure shows that when all of these experimental facts are taken together, any particle in the mass region of interest is precluded. However a loophole still exists. While the g-2 constraints appear to provide very stringent bounds on any new particle coupling to the electron, one problem with this conclusion is evident

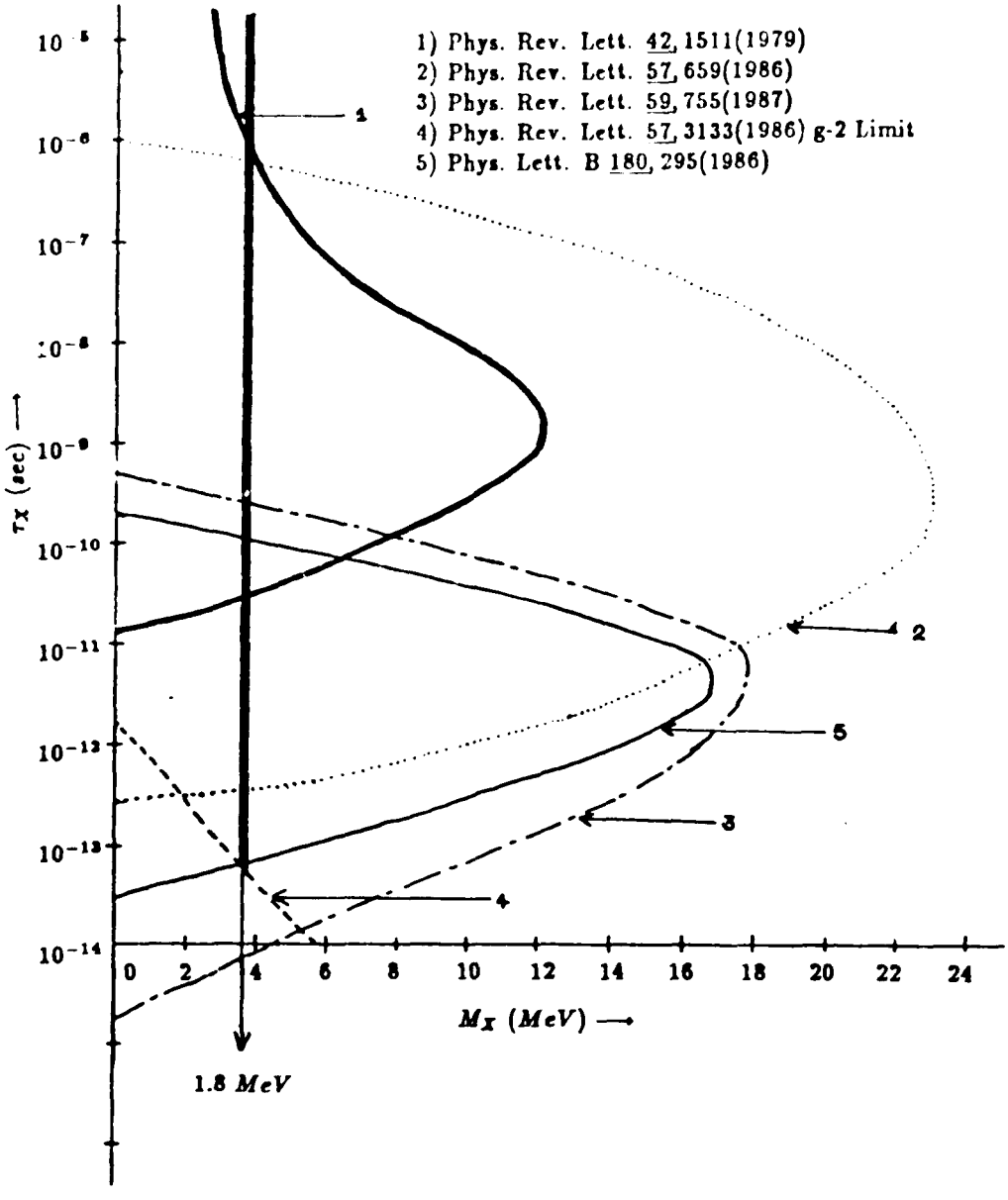

Figure 2.5.6 The plot showing the excluded regions (to the right of each curve) of light particle from the beam dump and the (g-2) experiments. The line at 1.8 MeV shows the location of proposed new particle from the GSI results. Part of this line is thickened to show the allowed regions from the g-2 results alone.

from Fig. 2.6.5. Since the coefficients K_i have different signs for (S,A) and (P,V) couplings, contributions from several particles (of different coupling type) can cancel resulting in a smaller value of $\Delta a_i^{e,\mu}$. In this regard, we should note that, the GSI results do have more than one sum energy line.

7. Is it a Composite System ?

The EPOS results[1] clearly show three sum energy lines at 610, 750, and 815 keV, an observation which is not easily accommodated in a point-like particle scenario, since it would imply not one but several new particles. Any new point-like particle, moreover, would have to interact strongly with hadronic matter with a cross section per nucleon large compared to $10^{-26} cm^2$, and as already noted there is mounting evidence against a light particle with invariant mass in the region of interest. The next logical speculation is a composite system with several excited states consistent with the observed line structures.

In postulating a composite system, one is immediately faced with two difficulties. *A priori*, one does not know the constituents which comprise the composite system, nor does one know their interactions. Consequently some of the proposed composite models contain new point-like particles as well as novel schemes for their interactions. We will briefly discuss some of the models.

Quasibound Electron-Positron State and Poly-positronium

Wong and Becker[55] explored the possibility of a quasibound electron-positron state arising from strong electromagnetic interactions at short distance. The Coulomb interaction between the electron and the positron creates only well known positronium states and cannot explain the EPOS results. However, the magnetic interaction at short distance is rather singular in nature and can be strongly attractive requiring a non-perturbative analysis. Wong and Becker treated the interaction as a static force between two magnetic dipoles. (A particle at rest with a magnetic moment $\vec{\mu}$ generates a vector potential $\vec{A} = \frac{\vec{\mu} \times \vec{r}}{r^3}$, which acts on the other particle.) Such an interaction can be very attractive when the spin and orbital momentum are properly aligned. Although there is no magnetic $\vec{S} \cdot \vec{L}$ interaction when $S = 0$, for $S = 1$, $L = 1$, and $J = 0$ there is a strong interaction at short distances which produces a potential well that extends over a range of a few fm and is deep enough to achieve binding. Such an interaction can create a $J^{PC} = 0^{++}$ magnetic resonance at an energy of $E = 1.579$ MeV, where P and C stand for the parity and charge conjugation quantum numbers respectively. The resonance can decay through tunneling, and it can produce equal energy electron and positron lines.

Wong and Beckers analysis, however, is based on a classical static dipole interaction between the electron and the positron, which has little physical reality. The extreme localization of the e^+e^- state demands large momentum transfer thereby requiring the relativistic treatment of effects such as recoil and radiation. Recently, Geiger *et al.*[56] solved a covariant

relativistic two fermion equation for short distances and found that the effective radial potential is highly singular. It has no potential pocket that can produce bound e^+e^- states.

A composite system consisting of a droplet containing several electron-positron pairs was introduced by Müller *et al.*[57] Such a tightly bound polypositronium system can have a large number of excited states, corresponding to either single particle or collective excitations. Since the electromagnetic force is not strong enough to produce binding, a new microscopic force has to be introduced. The model has difficulty explaining why such a force does not produce any energy corrections for atomic levels. More significantly, the model fails to predict results relevant to the EPOS data.

New QED Phase

Superheavy-ion collisions create unusually strong and rapidly varying electromagnetic fields. Thus some attention has been given to the possibility of a new non-perturbative QED phase with a spectrum of associated e^+e^- bound states.[58–60] There is additional theoretical impetus for a non-perturbative QED phase from both continuum and lattice studies. Even though the new phase can account for most of the observed GSI features, there are still several difficulties with the models, as we will point out shortly.

Celenza *et al.*[58] proposed that the GSI features are produced from the decay of nontopological solitons formed in a new vacuum created by the intense field of the colliding ions. With the introduction of a photon condensate which screens the intense fields of the heavy ions, a new vacuum

phase results. The new phase contains quasiparticles called quasielectrons and quasipositrons which are heavier than ordinary electrons due to their coupling to the condensate. The model thus gives rise to a soliton of mass 1.7 MeV with a characteristic radius of about 300 fm and several excited states having level spacings of 100 keV. In this scenario, the width of the observed electron-positron peaks can be explained naturally, since the nuclear quasimolecule responsible for the new phase exists only for a short period of time ($10^{-19} - 10^{-20}$ s) and the decay takes place after the intense fields of the heavy ions cease to exist. Since the soliton is at rest in the center-of-mass frame of the colliding ions, the decay products will experience only a small Doppler shift in the laboratory frame. Thus the near equality of the electron and the positron energies is easily explained, since the decay takes place after the heavy ions have flown apart.

A proposal by Ng and Kikuchi[59] is also based on the assumption of a new QED phase formation. In order to calculate the spectrum of a strongly coupled positronium atom, they used the Schrödinger equation with a linear potential between two charged particles. The ground state mass of the system was taken as 1650 keV and the 2S-1S splitting as 200 keV (guided by the EPOS results of sum lines at 1650 keV and 1850 keV), thereby fixing the "string tension" for the model potential. Their model predicts higher S-states at 2013, 2158, and 2259 keV. In addition it predicts the existence of strongly bound photon states, the QED counterpart to the glueball states in QCD.[61]

Lattice QED calculations for a strong coupling phase were performed by Caldi and Chodos.[60] They calculated the low lying meson spectrum using a Hamiltonian formulation with Kogut-Susskind fermions. The three peaks observed in the EPOS experiment are reasonably well reproduced by the Caldi and Chodos approach. Additional peaks in this mass range are also predicted, but they lie beyond the energy resolution achieved with the experimental apparatus at GSI. The lowest lying state in the Caldi-Chodos approach is an *electro-pion*, and as in QCD, it may be considerably lighter than the other mass states.

The QED phenomenology that we have discussed thus far in this section is based on the assumption that the new phase is formed in the fields created by the super heavy ion collisions. We know, both from continuum[62] and lattice[63] studies that, as the coupling constant α is increased to unity, QED undergoes a transition to a confining, strongly coupled phase in which the chiral symmetry is broken. However, in the heavy ion collisions at GSI, the coupling constant has the usual QED value of $\frac{1}{137}$. Hence, for the new phase to materialize, there must be an order parameter O, that varies with the external electromagnetic field, so that a phase transition can occur at the weak coupling as shown in Fig. 2.7.1.[64] Unfortunately, there are theoretical arguments against this scheme. Dogotto and Wyld, [65] for example, studied the behaviour of QED on the lattice in the presence of a background Coulomb field and showed that the phase transition point moves toward the strong coupling point rather than the weak coupling point. The strong Coulomb field will thus break up the electron-positron pairs created, thereby

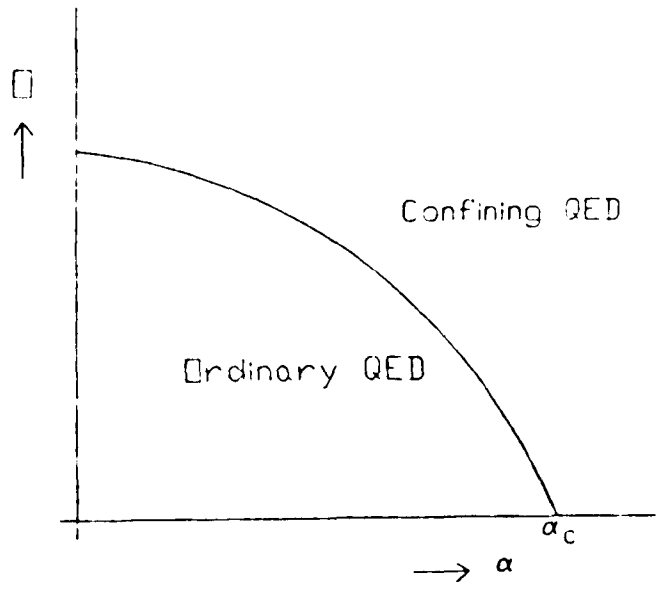

Figure 2.7.1 Possible phase diagram showing the new QED phase in the presence of a strong external electromagnetic field. O is the order parameter depending on the external field and α is the electromagnetic coupling constant.[64]

reducing the chance for the formation of the condensates responsible for the chiral symmetry breaking. A possible rejoinder to this argument is the observation that the relevant order parameter is not the magnitude of the static Coulomb field. At present, however, the various models have not isolated any order parameter associated with external field configurations that can drive the system through the phase transition. Thus although the concept of a new

QED phase formation in heavy ion collisions has merits over other models, it is quite speculative and will remain so until a triggering mechanism for the phase transition is found and a detailed non-perturbative analysis of QED is performed.

A Model with New Fermions

A bag picture for X can be constructed[66] along the same line as the MIT bag model[67] with the constituents treated as essentially free particles. The radius and the mass of the bag are related by uncertainty principle. The resulting expression for the energy of the bag, E_{bag}, consists of two parts, one characterized by a volume energy and one, by a single-particle energy. Specifically, E_{bag} can be written as

$$E_{bag} = \frac{4}{3}\pi R_X^3 B + E_y, \tag{2.7.1}$$

where B is the bag pressure and E_y is the energy eigen value of the bag constituents determined by the free particle Dirac equation, assuming linear bag boundary conditions. For a spherical bag E_y is proportional to R_X^{-1}, where R_X is the radius of the bag.

Schramm *et al.*[66] developed a bag picture by introducing a new set of light electrically charged fermions $y^{\pm}$ having a mass m_y and bound together by a hitherto unknown confining force similar to the SU(3) colour force for the MIT bag picture. The radius of the bag is chosen such that the energy of the bag is minimum at 1.8 MeV, with the consequence that the bag pressure B ranges from $B^{1/4} \approx 250$ keV for $m_y = 0$ to $B^{1/4} = 0$ for $m_y = 900$ keV.

The corresponding radius R_X ranges from 400 fm to 4000 fm. Schramm *et al.* chose a large radius to produce a rich spectrum of energy levels as required by the GSI results. Since the energy of the bag decreases substantially when an external electromagnetic field is present, the y^+y^- spectrum will be similar to that for spontaneous e^+e^- pair creation in an overcritical vacuum. The only difference from the situation for spontaneous sparking is that there are no occupied y^- states available initially to suppress pair creation. However, the relative enhancement will be partially compensated by a suppression due to the relatively higher mass of m_y compared to the electron mass. Since the whole bag is bound by the heavy ions, the X-particle will be produced preferentially at rest in the center of mass system of the colliding nuclei, in agreement with the GSI observations. Additional energy gained by the bag as it is dragged along by one of the separating nuclei can be shown to be small.

Even though the bag model of Schramm *et al.* is able to reproduce several of the experimental features of the heavy ion data, it introduces new particles and a hitherto unknown confining force. Since there is no evidence for such a system from any other known experiments, it seems somewhat unwarranted to introduce a new family of fermions with an associated confining force just to explain few structures observed at GSI.

8. Constraints on a Light Composite Particle

Many of the constraints applicable to a point particle, discussed earlier, are not germane or can be circumvented for a composite system. First,

the existence of a composite system will leave the electron g-factor anomaly essentially unchanged. (The existence of positronium, for example, positronium does not modify the observed $g-2$ factor.) Second, since the X-photon coupling is suppressed by higher powers of $R_{nucleus}/R_X$, depending on the multipolarity of the photon, an extended object with a size of several fm will not contribute significantly to Delbrück scattering. Finally, since the X-nucleon coupling varies as the ratio of the nucleon to X volumes, a large X composite will not produce a competing decay mode of excited nuclear levels compared to γ-decays. One note of caution–if the constituents of the composite comprise a set of new particles, such as $y^{\pm}$, their existence will initiate jet production in high-energy experiments, and this is not observed.

The probability of observing a composite object in beam dump experiments has been analysed by Schäfer.[22] He concludes that the cross section for X-bremsstrahlüng in electron beam dump experiments is suppressed only if the composite has a size in excess of 100 fm. For example, an extended object of size $R_X \sim 1000$ fm with an internal charge distribution will have a typical mean free path of

$$\lambda = \frac{1}{\sigma\rho} \sim \frac{1}{\pi R_X^2 \cdot 4 \times 10^{22} cm^{-3}} \sim 1.6 \times 10^{-3} cm, \qquad (2.8.1)$$

where we have used the geometrical area of the object for the total cross section σ, ρ representing the typical number density of the target atoms. Hence, a composite object will never escape the dump, even if it is produced in the dump itself.

However, it should be remembered that a very long-lived small object can travel and decay beyond the sensitive part of the detector volume. Even though the composite models provide a viable explanation for the GSI data, more systematic studies are needed to establish the physical foundation of these models.

Chapter 3.

Experimental Approach - Phenomenological considerations

1. Overview

In the previous chapter, we summarized the main features of the GSI results and some of the phenomenological models proposed to explain them. The observation of the correlated electron-positron lines at kinetic sum energies of 620, 760, and 815 keV by the EPOS group and the subsequent observation of the sum energy lines at 540, 640, 716, 809, and 895 keV by the ORANGE group cannot be explained satisfactorily by any of these models. Even though multiple line structures make a single-particle explanation very unlikely, we could be witnessing new physics with a family of new particles. Alternately, we could be observing a composite system with several excited states. In either case, an obvious way to proceed is through the investigation of positron-electron (Bhabha) scattering. In this chapter we will describe the phenomenological considerations for a positron-electron scattering experiment searching that has its goal a search for a resonance state. We will also briefly review the results of several experiments performed using these principles.

2. Resonant Bhabha Scattering off Electrons at Rest

An independent confirmation of the existence of X can be obtained by producing it in a process ($e^+e^- \longrightarrow X$) which is the inverse of the suggested decay mode. Narrow resonances would then appear in the s-channel for electron-positron scattering at a center-of-mass energy corresponding to the invariant mass of X. Since colliding beams experiment with electrons and positrons at the required energy scale would be extremely difficult to carry out, a more realistic approach is one in which a beam of positrons interacts with electrons in a fixed atomic target. Such an approach unfortunately suffers from complications arising from the momentum distribution of the bound electrons, as we will see shortly. First we will examine the scattering process, assuming that the electrons are at rest.

The interaction between the resonant state and the electron can be represented by the Lagrangian[54]

$$L_{int} = g_i \int d^3x\, \overline{\psi} \Pi^{(i)} \psi\, \phi_X, \tag{3.2.1}$$

where g_i, the coupling constant, is related to the particle-lepton coupling constant α_i introduced in Eq. (2.6.13) through the relation $\alpha_i = \frac{g_i^2}{4\pi}$. The integrand contains a bilinear covariant factor, $\overline{\psi}\Pi^{(i)}\psi$, where ψ represents the electron field and $\Pi^{(i)}$, the matrices for the coupling vertices. The field representing X is denoted by ϕ_X. The values of the coupling matrices are listed in Table 3.2.1 for spin-0 and spin-1 resonant states.(We will not consider any higher spin states in this description.)

Coupling (i)	J^π	$\Pi_a^{(i)}$	$\Pi_b^{(i)}$	$\Pi_c^{(i)}$
Scalar	0^+	1		
Pseudoscalar	0^-	$i\gamma_5$		
Vector	1^-	γ_μ	$(p_1+p_2)_\mu$	$(p_1-p_2)_\mu$
Pseudovector	1^+	$\gamma_\mu\gamma_5$	$i(p_1+p_2)_\mu\gamma_5$	$i(p_1-p_2)_\mu\gamma_5$

Table 3.2.1 Elementary vertices for the coupling of spin-0 or spin-1 resonant states to the electron. They are quoted in the momentum space language. For spin-1 case three vertices $\Pi_a^{(i)}, \Pi_b^{(i)}$, and $\Pi_c^{(i)}$ are possible.

The effective coupling constant g_i, depends on the momenta of the electron, the positron, and the X-particle which we will denote by p_1, p_2, and k respectively. Lorentz invariance requires the coupling constant to be a function only of invariant quantities, such as p_1^2, p_2^2, and k^2. Since, these quantities have identical values for the production and decay of X, g_i takes the same numerical values for both the processes. An upper bound for the coupling constant is derived in Section 2.6 from the agreement between the observed and the theoretical values for the electron anomalous magnetic moment.

The expression given by Eq. (3.2.1) for the interaction Lagrangian is valid only for an elementary point-like particle X. For a composite object with an internal structure a *form factor* [54] must be included. For large

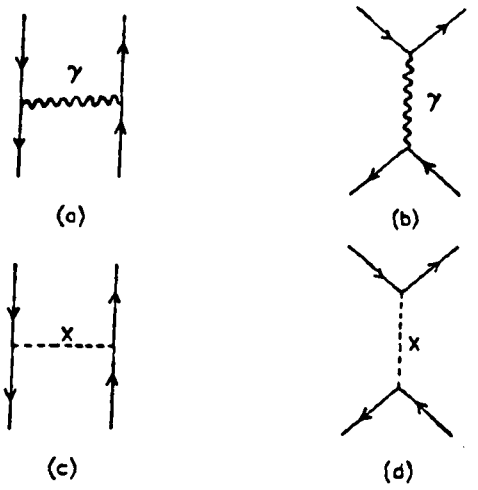

Figure 3.2.1 The first order Feynman diagrams for Bhabha scattering mediated by a photon (a,b) or a resonance state X (c,d).

values of momentum transfer, this modification will result in a suppression of the effective coupling constant in momentum space. Since the resonance Bhabha scattering and the virtual processes contributing to anomalous magnetic moment are sensitive to different values of momentum transfer, it is difficult to make model independent predictions. Hence we will not include formfactor in the rest of the treatment.

The elastic positron-electron scattering, known as Bhabha scattering, is a well understood process in the frame work of quantum electrodynamics. It is mediated by a photon as shown in Fig. 3.2.1(a)-(b). The experimental value for the Bhabha cross section agrees with the theoretical QED prediction to an accuracy of $\pm 10\%$ in the $1 - 2$ MeV range.[68] The validity of the theory has apparently not been tested to a greater accuracy in this range

due to an apparent lack of expectation of any new physical insight. The large uncertainty in the tests, however, leaves room for new physics.

If an X-particle exists it can mediate the elastic scattering in a way identical to the photon. The first order contribution arising due to the X-particle resonant state can be expressed by means of the Feynman diagrams as shown in Fig. 3.2.1(c)-(d). If α_i is much smaller than the fine structure constant α (as implied by the results in section 2.6), the contribution from diagram (c) can be neglected in comparison to the contributions from the diagrams (a) and (b). However, the annihilation diagram in (d) will be enhanced, when the intermediate momentum meets the on-shell condition $(p_1 + p_2)^2 = m_X^2$. Then, narrow resonances will be observable in the s-channel Bhabha scattering at a center-of-mass energy corresponding to the invariant mass of X.

The kinematic variables are identical for positron-electron scattering involving either the photon or the X-particle. The relevant 4-vectors are represented by p_1, p_2, p_3, and p_4. In the laboratory frame of reference they are given by

$$p_1 = (E, \vec{p}),\ p_2 = (m, \vec{0}),\ p_3 = (E_3, \vec{p_3}),\ p_4 = (E_4, \vec{p_4}). \tag{3.2.2}$$

Energy-momentum conservation leads to

$$P \equiv p_1 + p_2 = p_3 + p_4, \tag{3.2.3}$$

and

$$p_i^2 = m^2, \quad i = 1,2,3,4. \tag{3.2.4}$$

The scattering angles and the energies of the final-state particles, obtained from the equations

$$p_3^2 = (p_1 + p_2 - p_4)^2 \quad \text{and} \quad p_4^2 = (p_1 + p_2 - p_3)^2, \tag{3.2.5}$$

satisfy the relation

$$E_j = m\frac{(E+m) + (E-m)\cos^2\theta_j}{(E+m) + (E-m)\cos^2\theta_j}, \quad \text{for} \quad j = 3, 4, \tag{3.2.6}$$

where θ_j represents the scattering angles of the final positron/electron in the laboratory frame. With the application of energy conservation and the use of Eq. (3.2.6), it can be shown that the scattering angles satisfy the relation

$$\cos^2\theta_3 = \frac{(E+m)^2\sin^2\theta_4}{4m^2 + (E^2 + 2mE - 3m^2)\sin^2\theta_4}. \tag{3.2.7}$$

According to the standard rules of scattering theory,[69] the doubly differential Bhabha scattering cross section is given by

$$d\sigma = \frac{m^2}{\sqrt{(p_1 \cdot p_2)^2 - m^4}}\, dLips(s; p_3, p_4)\, |M_{fi}|^2. \tag{3.2.8}$$

The first factor normalizes the cross section to unit incident flux and to the number of target particles per unit volume. The factor $dLips(s; p_3, p_4)$ is known as the *Lorentz invariant phase space* and is given by

$$dLips(s; p_3, p_4) = \left(\frac{1}{(2\pi)^3}\frac{d^3p_3}{(E_3/m)}\right)\left(\frac{1}{(2\pi)^3}\frac{d^3p_4}{(E_4/m)}\right) \times (2\pi)^4\, \delta^{(4)}(p_3 + p_4 - p_1 - p_2), \tag{3.2.9}$$

where the first two factors arise as a result of summing over all the available two-particle final states. The δ-function ensures that the energy and momentum are conserved. The variable $s = (p_1 + p_2)^2$ is the square of the total

center-of-mass energy and M_{fi} is the invariant amplitude for the scattering process, to be evaluated according to the Feynman rules. The normalization used in the above equations are

$$u^+u = E/m \quad \text{and} \quad v^+v = E/m, \tag{3.2.10}$$

where u and v are the electron and positron spinors, respectively.

Integrating Eq. (3.2.8) with the help of the δ-function in Eq. (3.2.9) leads to the expression

$$\frac{d\sigma}{d\Omega_3} = \frac{m^4}{\pi^2} \frac{cos^2\,\theta_3}{[(E+m)-(E-m)cos^2\,\theta_3]} \times \frac{1}{[(E+m)+(E-m)cos^2\,\theta_3 - 2(E+m)cos\,\theta_3]} |M_{fi}|^2. \tag{3.2.11}$$

The invariant amplitude M_{fi} has two parts, M_a and M_b, corresponding to diagrams (a) and (b) of Fig. 3.2.1 respectively. Specifically M_{fi} can be written as

$$M_{fi} = M_a + M_b, \tag{3.2.12}$$

where M_a and M_b are given by

$$M_a = -ie^2\,[\bar{u}(p_4,s_4)\gamma_\mu u(p_2,s_2)]\,\frac{1}{(p_1-p_3)^2}\,[\bar{v}(p_1,s_1)\gamma^\mu v(p_3,s_3)] \tag{3.2.13}$$

and

$$M_b = ie^2\,[\bar{u}(p_4,s_4)\gamma_\mu v(p_3,s_3)]\,\frac{1}{(p_1+p_2)^2}\,[\bar{v}(p_1,s_1)\gamma^\mu u(p_2,s_2)]. \tag{3.2.14}$$

Here s_j denotes the spin indices of the initial and final-state particles, $\bar{u}$ denotes the product $u^+\gamma^0$, and γ_μ denotes the usual 4×4 Dirac-matrices.

The relative negative sign between the two terms is due to the interchange of the external fermion lines in the corresponding Feynman diagrams.

In the present experiment, initial polarization of the collision partners are not known, and the polarization of the final-state particles are not determined. Hence, to obtain the unpolarized cross section from Eq. (3.2.11), we must average $|M_{fi}|^2$ over all the initial polarization states and sum over all the final polarization states. The resulting expression is

$$\begin{aligned}\overline{|M_{fi}|^2} &= \frac{1}{4}\sum_{s_1,s_2}\sum_{s_3,s_4}|M_{fi}|^2 \\ &= \frac{1}{4}\sum_{s_1,s_2}\sum_{s_3,s_4}\left[|M_a|^2+|M_b|^2+M_a^*M_b+M_aM_b^*\right],\end{aligned} \tag{3.2.15}$$

where $\frac{1}{4}\sum_{s_1,s_2}$ is due to the averaging over the initial spin states and $\sum_{s_3,s_4}$ is due to the summing over the final spin states. The 4-terms in the above equation can be simplified using trace theorems.[70] We will omit the algebraic derivation, and will quote only the final result:[71]

$$\begin{aligned}\frac{d\sigma}{d\Omega_3} &= r_e^2\left(2\frac{\gamma+1}{\beta^2\gamma}\right)^2\frac{cos\,\theta_3}{[2+(\gamma-1)sin^2\,\theta_3]^2} \\ &\times\left\{\frac{4}{(1-x)^2}\left[1-\frac{\gamma^2-1}{2\gamma^2}(1-x)+\frac{1}{2}\left(\frac{\gamma-1}{2\gamma}\right)^2(1-x)^2\right]\right. \\ &-\frac{2}{1-x}\left(\frac{\gamma-1}{\gamma+1}\right)\left[\frac{2\gamma+1}{\gamma^2}+\frac{\gamma^2-1}{\gamma^2}x+\left(\frac{\gamma-1}{2\gamma}\right)^2(1-x)^2\right] \\ &\left.+\left(\frac{\gamma-1}{\gamma+1}\right)^2\left[\frac{1}{2}+\frac{1}{\gamma}+\frac{3}{2\gamma^2}-\left(\frac{\gamma-1}{2\gamma}\right)(1-x)^2\right]\right\},\end{aligned} \tag{3.2.16}$$

where $r_e = e^2/4\pi m$, $\beta = |\,\vec{p}\,|/E$, $\gamma = E/m$, and

$$x = \frac{2-(\gamma+3)\,sin^2\,\theta_3}{2+(\gamma-1)\,sin^2\,\theta_3}. \tag{3.2.17}$$

The total cross section is the integral of Eq. (3.2.16) taken over all solid angles. The differential cross section is strongly peaked in the forward direction and diverges as $\theta_3 \to 0$. The divergence is due to the fact that for low-momentum transfer scattering we cannot neglect the emission of very low-energy photons by electrons and positrons.

The invariant amplitude for the annihilation diagram (d) is

$$M_{fi}^{(i)} = g_i^2 \left[\bar{u}(p_4, s_4)\Pi_\mu^{(i)} v(p_3, s_3)\right] \Delta^{\mu\nu}(P) \left[\bar{v}(p_1, s_1)\Pi_\nu^{(i)} u(p_2, s_2)\right], \quad (3.2.18)$$

where the superscript on the invariant amplitude is introduced to accommodate the different coupling types given in Table 3.2.1. The factor Δ denotes the propagator for the boson field of the X-particle of mass m_X. The Lorentz vector indices μ and ν have meaning only for the spin-1 case.

For the spin-0 case the propagator is

$$\begin{aligned} \Delta(P) &= \frac{1}{P^2 - (m_X - i\Gamma^{(i)}/2)^2} \\ &= \frac{1}{(P^2 - m_X^2 + (\Gamma^{(i)})^2/4) + i m_X \Gamma^{(i)}}, \end{aligned} \quad (3.2.19)$$

where we have included the finite resonance width $\Gamma^{(i)}$to avoid the singularity when $s \to m_X^2$. The relation between the decay width and the coupling constant α_i is given by Eq. (2.6.18). For the spin-1 case the propagator becomes

$$\Delta_{\mu\nu}(P) = \left(-g_{\mu\nu} + \frac{P_\mu P_\nu}{m_X^2}\right) \Delta(P), \quad (3.2.20)$$

which can be derived from the Klein-Gordan equation for the boson field.[69] In the lab frame s can be written as

$$s = P^2 = (p_1 + p_2)^2 = 2m(E + m), \quad (3.2.21)$$

in which case $\Delta(P)$ takes the form

$$\Delta(P) = \frac{1}{2m}\,\frac{1}{E - E_R + im_X\Gamma^{(i)}/2m}, \tag{3.2.22}$$

where

$$E_R = \frac{m_X^2 - 2m^2 - (\Gamma^{(i)})^2}{2m}. \tag{3.2.23}$$

Since the square of the amplitude must be averaged over the initial spin states and summed over the final spin states, we obtain

$$\overline{|M_{fi}^{(i)}|^2} = \frac{1}{(2s_1+1)(2s_2+1)} \sum_{s_1,s_2} \sum_{s_3,s_4} |M_{fi}^{(i)}|^2, \tag{3.2.24}$$

and

$$\begin{aligned}\overline{|M_{fi}^{(i)}|^2} =& \frac{g_i^4}{4}\,\Delta^{\mu\nu}(P)\Delta^{*\delta\eta}(P) \\ &\times \mathrm{Tr}\Big(\frac{\not p_3 - m}{2m}\gamma^0\Pi_\delta^{(i)}\gamma^0\frac{\not p_4 + m}{2m}\Pi_\mu^{(i)}\Big) \\ &\times \mathrm{Tr}\Big(\frac{\not p_1 - m}{2m}\Pi_\nu^{(i)}\frac{\not p_2 + m}{2m}\gamma^0\Pi_\eta^{(i)}\gamma^0\Big),\end{aligned} \tag{3.2.25}$$

where $\not p_j$ for $j = 1,2,3,4$ denotes the appropriate vector contracted with the Dirac γ-matrices; that is, $\not p = \gamma^\mu p_\mu$. Using the trace theorems, Eq. (3.2.25) can be simplified to

$$\overline{|M_{fi}^{(i)}|^2} = \frac{g_i^4}{4}\,|\Delta(P)|^2\,\mathcal{J}^{(i)}(s,t), \tag{3.2.26}$$

where $t = (p_3 - p_1)^2 = (p_4 - p_2)^2$. The function $\mathcal{J}^{(i)}(s,t)$ contains all of the algebra characteristic of the interaction.

Substituting the spin-averaged matrix element of Eq. (3.2.26) into Eq. (3.2.11) we can express the unpolarized, differential cross section for

resonant scattering as

$$\frac{d\sigma^{(i)}}{d\Omega_3} = \frac{g_i^4}{4}\frac{m^4}{\pi^2}\frac{cos^2\theta_3}{[(E+m)-(E-m)cos^2\theta_3]}|\Delta(P)|^2 \times \frac{1}{[(E+m)+(E-m)cos^2\theta_3-2(E+m)cos\theta_3]}\mathcal{J}^{(i)}(s,t). \tag{3.2.27}$$

Now substituting for $\Delta(P)$ from Eq. (3.2.22) we finally obtain

$$\frac{d\sigma^{(i)}}{d\Omega_3} = \alpha_i^2\frac{cos^2\theta_3}{[(E+m)-(E-m)cos^2\theta_3]}\frac{m^2}{(E-E_R)^2+\left(\frac{\Gamma^{(i)}m_X}{2m}\right)^2} \times \frac{1}{[(E+m)+(E-m)cos^2\theta_3-2(E+m)cos\theta_3]}\mathcal{J}^{(i)}(s,t). \tag{3.2.28}$$

The function $\mathcal{J}^{(i)}(s,t)$ can be evaluated with the use of the $\Gamma^{(i)}$ matrices from Table 3.2.1 corresponding to the various coupling types $i = S, P, V, A$. The resulting expression for $\mathcal{J}^{(i)}(s,t)$ are

$$\begin{aligned}
\mathcal{J}^{(S)}(s,t) &= \frac{1}{4m^4}(s-4m^2)^2 \\
\mathcal{J}^{(P)}(s,t) &= \frac{1}{4m^4}s^2 \\
\mathcal{J}^{(V)}(s,t) &= \frac{1}{m^4}\left(\frac{s^2}{2}+4m^4+(s-4m^2)t+t^2\right) \\
\mathcal{J}^{(A)}(s,t) &= \frac{1}{m^4}\left(\frac{s^2}{2}-4m^2s+12m^4-\frac{8m^4s}{m_X^2}+\frac{4m^4s^2}{m_X^4}+(s-4m^2)t+t^2\right).
\end{aligned} \tag{3.2.29}$$

Using the resonance energy E_R for the incident positron energy E and substituting the corresponding values of s and t into Eq. (3.2.29) one can obtain the resonance cross section for different coupling types in the laboratory frame directly from Eq. (3.2.28).

The total unpolarized resonance cross section, obtained by integrating the Eq. (3.2.27) over the solid angle $d\Omega_3$, is given by[54]

$$\sigma^{(i)} = \frac{\pi}{4}\frac{\alpha_i^2}{m^2}\frac{m^2}{(E-E_R)^2+\left(\frac{\Gamma^{(i)}m_X}{2m}\right)^2}\zeta^{(i)}(E), \tag{3.2.30}$$

where the coefficients $\zeta^{(i)}(E)$ (when evaluated at the resonance) are given by

$$\begin{aligned}
\zeta^{(S)}(E_R) &= (\rho-4)^2/\rho, \\
\zeta^{(P)}(E_R) &= \rho^2, \\
\zeta^{(V)}(E_R) &= \frac{4}{3}(\rho+2)^2/\rho, \\
\zeta^{(A)}(E_R) &= \frac{4}{3}(\rho-4)^2/\rho.
\end{aligned} \tag{3.2.31}$$

Here, the definition of $\rho = (m_X/m)^2$ is the same as that in Chapter 2. Using α_i from Eq. (2.6.18) to express the cross section in terms of the decay width of the resonant state, we obtain

$$\sigma^{(i)} = \frac{4\pi}{m_X^2}\frac{2J_i+1}{\rho-4}\frac{\left(\frac{\Gamma^{(i)}m_X}{2m}\right)^2}{(E-E_R)^2+\left(\frac{\Gamma^{(i)}m_X}{2m}\right)^2}, \tag{3.2.32}$$

where we have employed Eq. (2.6.19) to express $\zeta^{(i)}(E_R)$ in terms of $f^{(i)}(\rho)$. We have used J_i to denote the spin of the resonance state. The connection between the integrated resonance cross section and the decay width given by Eq. (3.2.32) is understandable, since the production and the decay processes are related to each other by the *principle of detailed balance*.[72]

In deriving Eq. (3.2.32) we have assumed the produced resonance states will decay entirely through the e^+e^- channel. However, it is conceivable that other channels such as $\gamma\gamma$ or $\gamma\gamma\gamma$ are also open, thus reducing the

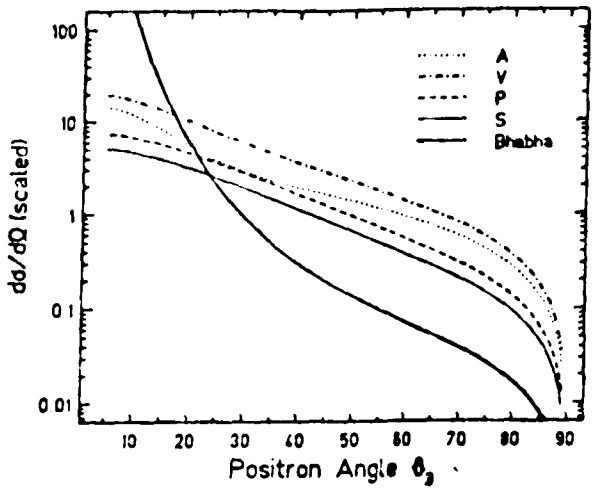

Figure 3.2.2 The differential cross section as a function of positron scattering angle θ_3 in units of α^2/m^2 for e^+e^- scattering at a beam energy, $E = 2.262$ MeV. The assumed mass is $m_X = 1.832$ MeV. The thick line shows ordinary Bhabha scattering. The other lines correspond to resonant cross sections for various couplings.[54]

e^+e^- signal in a Bhabha scattering resonance search. In order to accommodate such open channels, the cross section of Eq. (3.2.32) must be multiplied by the branching ratio, $\Gamma^{(i)}_{e^+e^-}/\Gamma^{(i)}$, where $\Gamma^{(i)}_{e^+e^-}$ denotes the partial width of the e^+e^- channel.

The differential cross section evaluated by Reinhardt *et al.*,[54] for Bhabha and resonance scattering is reproduced in Fig. 3.2.2. The evaluation neglects interference terms between the resonance diagram and the Bhabha diagrams. However, these terms are of the order of $\alpha\alpha_i/m^2$ and cancel

each other when averaged over the resonance region.[54] Caldi *et al.*[73] in fact included the interference terms in their evaluation and showed that the interference structure observable in the free electron case is completely "washed out" by the smearing caused by the motion of target electrons.

3. Resonant Bhabha Scattering off Electrons Bound in an Atom

In carrying out the analysis in the previous section, we assumed the target electrons to be at rest. However, in a solid target the electrons are in constant motion. Since the sensitivity of a resonant search experiment depends strongly on the momentum distribution of the target electrons we will examine the problem in some detail.

It is well known in solid state physics that the motion of the target electrons broadens the spectrum of scattered photons, in a Compton scattering experiment.[74] In fact, it is this very property of the Compton scattered photon that is utilized for studying the electron momentum distribution in solids. We will briefly summarize the application of Compton profiling to the determination of momentum distribution of electrons in targets.

We all know that a photon of wave length λ, suffers a shift in the wave length, $\lambda' - \lambda$, when it scatters from a free electron in accordance with the relation

$$\lambda' - \lambda = \frac{2h}{mc} sin^2 (\phi/2), \qquad (3.3.1)$$

where ϕ is the angle of scattering. When the electron is in motion, the shifted line will be broadened so that $\lambda' - \lambda$ is given by

$$\lambda' - \lambda = \frac{2h}{mc} sin^2(\phi/2) - \frac{2\lambda sin(\phi/2)}{mc} p_z, \tag{3.3.2}$$

where p_z is the electron momentum projected onto the crystallographic scattering vector. The second term describes the broadening of the scattered radiation and is proportional to the electron momentum, p_z. Hence, the line shape - known as the Compton profile - can be used to obtain the one dimensional electron momentum distribution of the crystal studied.

The intensity of the scattered photon at any point in the profile will be proportional to the probability of observing the momentum component p_z, along the scattering vector. The Compton profile $J(p_z)$ is then given by

$$J(p_z) = \int\int dp_x\, dp_y\, P(p_x, p_y, p_z), \tag{3.3.3}$$

where $P(p_x, p_y, p_z)$ is the probability distribution for the target electrons. For an isotropic distribution of electron momenta, the integral can be converted to cylindrical coordinates

$$J(p_z) = 2\pi \int_0^\infty dp_r\, p_r\, P(p_x, p_y, p_z), \tag{3.3.4}$$

where p_r is the momentum distribution in x-y plane and is given by $p_r^2 = p_x^2 + p_y^2$. Now converting to total momentum variable, p, we get

$$J(p_z) = 2\pi \int_{|p_z|}^\infty dp\, p\, P(p_x, p_y, p_z). \tag{3.3.5}$$

Rewriting the compton profile in terms of the radial momentum distribution we get

$$J(p_z) = \frac{1}{2} \int_{|p_z|}^{\infty} \frac{I(p)}{p}\, dp, \tag{3.3.6}$$

where the function $I(p)$ is given by $I(p) = 4\pi p^2 P(p_x, p_y, p_z)$. The function $I(P)$ can be obtained by differentiating the compton profile $J(p_z)$. Using the resulting value of $I(p)$, the total cross section for the Bhabha scattering process can be averaged over the target electron momentum, for a given value of incident positron energy to yield

$$< \sigma(E) >= \frac{1}{2} \int \int I(p)\sigma(E)\, dp\, dcos\,(\theta_{e^-}), \tag{3.3.7}$$

where E is given by Eq. (3.2.2)

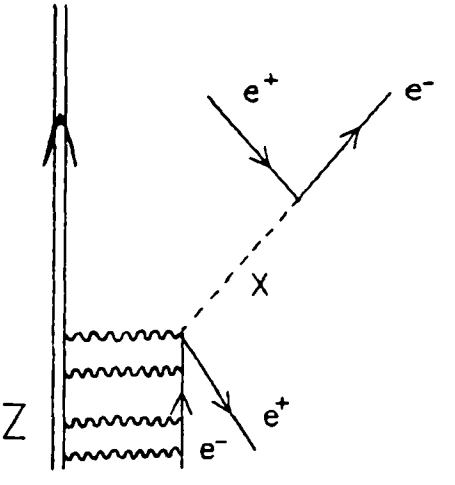

Figure 3.3.1 Feynman graph for resonant positron scattering off a bound atomic electron.

The Feynman diagram for the resonant scattering of a positron from a bound electron is shown in Fig. 3.3.1. For a positron of incident momentum $\vec{p}$, the corresponding production cross section can be written as[54]

$$d\sigma^{(i)} = \frac{E}{p}\frac{1}{(2\pi)^3} d^3p_X \, 2\pi\delta(E_X - E_n - E)\left|T_{fi}^{(i)}\right|^2 \tag{3.3.8}$$

with the transition matrix element

$$T_{fi}^{(i)} = g_i \int d^3x \, \phi_X^*(\vec{p_X}, \vec{x})\bar{\psi}_{e^+}(\vec{p}, \vec{x})\Pi^{(i)}\psi_n(\vec{x}), \tag{3.3.9}$$

where ϕ_X, ψ_{e^+}, and ψ_n denote the wave functions of the X-particle, the incident positron, and the bound electron respectively and E_X and E_n denote the energy of X-particle and bound electron respectively. The delta function results from the evaluation of the appropriate time integral. Assuming the incident positron is negligibly affected by the Coulomb repulsion of the nucleus (an assumption that is reasonable in the MeV region in which the experiment is performed), the positron wave function can be replaced by the plane wave, $\sqrt{m/E}\, v(\vec{p}, s)\, e^{-i\vec{p}\cdot\vec{x}}$. If an average is taken over the initial spin states, Eq. (3.3.8) then becomes

$$\frac{d\sigma^{(i)}}{d\Omega_X dE_X} = \pi\delta(E_X - E_n - E)\frac{p_X m}{p} g_i^2 F_n^{(i)}(\vec{q}, \vec{p}), \tag{3.3.10}$$

where the function $F_n^{(i)}$ is given by

$$F_n^{(i)}(\vec{q}, \vec{p}) = \frac{1}{2}\sum_s \left|\bar{v}(\vec{p}, s)\Pi(i)\psi_n(\vec{q})\right|^2, \tag{3.3.11}$$

and the electron wave function in the momentum space is given by

$$\psi_n(\vec{q}) = \frac{1}{(2\pi)^{3/2}} \int d^3x \, e^{-i\vec{q}\cdot\vec{x}}\, \psi_n(\vec{x}). \tag{3.3.12}$$

The corresponding total production cross section is

$$\sigma^{(i)} = 2\pi^2 \frac{m}{p^2} \Theta(E + E_n - m_X) \int_{|p-p_X|}^{p+p_X} dq\, q F_n^{(i)}(\vec{q}, \vec{p}), \qquad (3.3.13)$$

where the X-particle momentum is to be replaced in accordance with the relation $p_X^2 = (E + E_n)^2 - m_X^2$. As can be seen the integral Eq. (3.3.13) is closely related to the Compton profile of the target electrons.

Reinhardt *et al.*[54] performed the above integration with hydrogenic wave functions taken for the target electrons. Reproduced in Fig. 3.3.2(a)-(b), the result illustrate the X-production cross section as a function of the positron energy for hydrogenic atoms with Z = 1, 4, and 6. A narrow resonance is visible. In Fig. 3.3.2(b) the result is shown for Z = 90. The asymmetric shape of the cross section, evident in Fig. 3.3.2(b), is due to the relativistic motion of the electrons in a heavy atom. The arrows in Fig. 3.3.2(b) denote the incident positron energy for resonant scattering, and the relative shift of the arrows is caused by the additional energy contributed to the scattering by the bound electrons. Thus for heavier atoms the resonance state can be excited with a broad range of positron energies. However, the signal will be suppressed in inverse proportion to the energy spread of the target electrons. Calculations similar to those of Reinhardt *et al.* were performed by Caldi *et al.*[73] for a lithium target and is consistent with the above calculations.

We now consider the results of calculations performed specifically in connection with this thesis experiment for realistic momentum distributions of electrons in lithium and teflon. These distributions are shown in Fig. 3.3.3

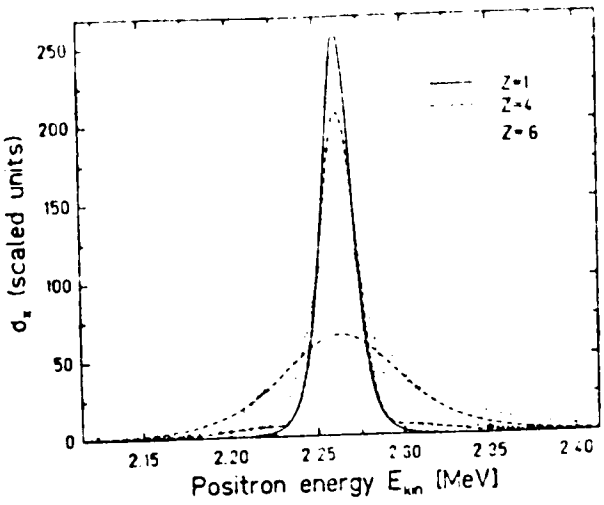

(a)

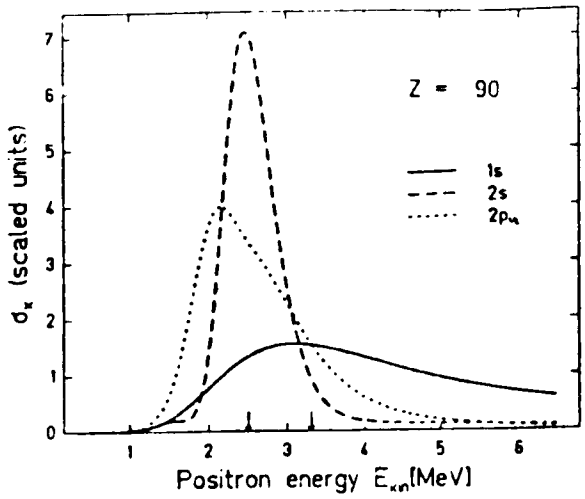

(b)

Figure 3.3.2 X-production cross section σ_X in units of α_X/m^2 for e^+ scattering of the unscreened bound atomic electrons as a function of the positron energy, with m_X = 1.832 MeV. (a) Full line: 1s-state of Z=1, Dashed line: 2s and 1s states of Z=4, Dotted line: 2s,2p, and 1s states of Z=6. (b) For Z=90; Full line: 1s state, Dashed line: 2s state, Dotted line: $2p_{1/2}$.[54]

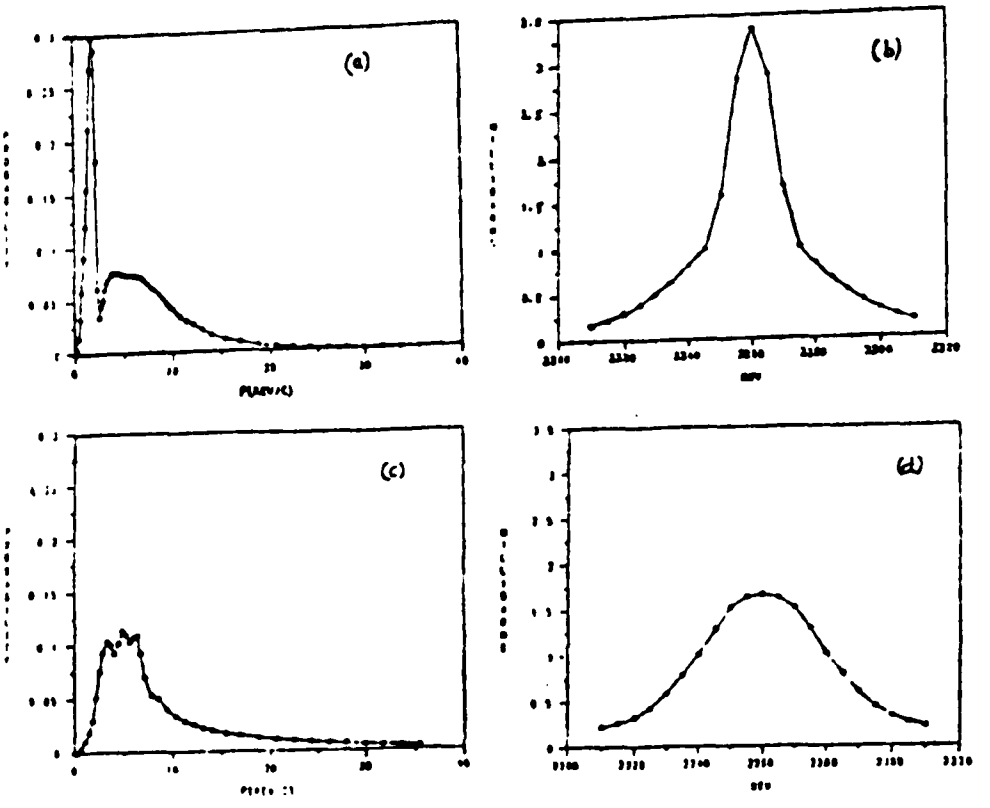

Figure 3.3.3 (a)Radial momentum distribution of electrons in Li, (b) particle production cross section with a Li target, (c) radial momentum distribution of electrons in teflon, and (d) particle production cross section with a teflon target. The parameters used are: $m_X = 1.8$ MeV and $\Gamma_X^{(P)} = 8.9$ MeV.[75]

along with the corresponding total cross section for $e^+e^- \to X \to e^+e^-$ for the case of a pseudoscalar coupling.[75] The width of the production cross section demonstrates the need to use a target such as lithium over a high-Z target for an increased resonance signal. In the experiment we will also use a second target like teflon for normalization, since the signal is much weaker for a teflon target compared to a lithium target as is evident from Figs. 3.3.3(b) and (d). The Fig. 4.6.5 shows the ratio of the total cross section for e^+e^- scattering which includes the Bhabha scattering and resonant scattering to the Bhabha cross section, integrated over the detector acceptance of the present experiment.

The X-resonance created will be identified through the e^+e^- decay channel. Therefore for completeness we will list the cross section corresponding to the full diagram given in Fig. 3.3.1. The Coulomb effects of the nuclei on the final state particles will be neglected.

The cross section for resonant Bhabha scattering is[54]

$$d\sigma^{(i)} = \frac{d^3p_3}{(2\pi)^3(E_3/m)}\frac{d^3p_4}{(2\pi)^3(E_4/m)}\frac{m}{p}(2\pi)^4\delta(E+E_n-E_3-E_4)\left|M_{fi}^{(i)}\right|^2. \tag{3.3.14}$$

The invariant matrix element is the same as in Eq. (3.2.25), except for the replacement of $u(p_1,s_1)$ by the bound momentum space wave function $\psi_n(\vec{q})$. In accordance with Eq. (3.2.25) the spin averaged matrix element is thus given by

$$\begin{aligned}\overline{|M_{fi}^{(i)}|^2} =& \frac{g_i^4}{2}\,\Delta^{\mu\nu}(P)\Delta^{*\delta\eta}(P) \\ &\times \mathrm{Tr}\Big(\frac{\not p_3 - m}{2m}\gamma^0\Pi_\delta^{(i)}\gamma^0\frac{\not p_4 + m}{2m}\Pi_\mu^{(i)}\Big) \\ &\times \Big(\bar\psi_n\Pi_\eta^{(i)}\frac{\not p_1 - m}{2m}\Pi_\nu^{(i)}\psi_n\Big).\end{aligned} \tag{3.3.15}$$

The total resonance cross section can then be found after the appropriate integration is performed in Eq. (3.3.14).

4. The Effects of Spread in Beam Parameters

Throughout the previous sections, we assumed that the positron beam energy was infinitely narrow and well defined. In practice, the beam will not be monochromatic, but rather it will have a finite energy spread, ΔE, about the mean beam energy, E. Hence, the cross sections derived previously will have to be averaged over an appropriate energy spread. Assuming a Lorentzian distribution for the beam energy spread we can write this average as

$$< A(E) > \;=\; \frac{1}{\pi}\int d\epsilon \frac{\frac{\Delta E}{2}}{(\epsilon - E)^2 + \left(\frac{\Delta E}{2}\right)^2} A(\epsilon), \qquad (3.4.1)$$

where $A(E)$ stands for either the differential or the total cross section. If the resonance width is small compared to the beam energy spread, the above averaging results in the replacement of $\frac{m_x \Gamma^{(\epsilon)}}{m}$ by ΔE in the denominators of Eq. (3.2.28) and Eq. (3.2.32).

Reinhardt *et al.*[54] performed calculations for a beam energy spread of $\Delta E = 10$ keV and for a positron scattering angle of $\theta_3 \sim 29°$ (corresponding to equal angles for positron and electron scattering in the laboratory frame). The results are summarized as follows in terms of resonant enhancements for

all four couplings:

$$\frac{\left(\frac{d\sigma^{(i)}}{d\Omega_3}\right)_{Res}}{\left(\frac{d\sigma}{d\Omega_3}\right)_{Bhabha}} < \begin{matrix} 1.3\% \\ 2.6\% \\ 16\% \\ 1.4\% \end{matrix} \quad \text{for} \quad i = \begin{matrix} S \\ P \\ V \\ A \end{matrix}, \tag{3.4.2}$$

When a range of scattering angles is taken into account, as will be the case for a realistic experiment, the enhancement will be diminished. For example for an angular acceptance window of $15° \leq \theta_3 \leq 45°$, the ratio in Eq. (3.4.2) will be approximately halfed. Under these conditions, a 1% level of sensitivity will demand a beam with an energy spread of only a few keV. Such conditions will then allow the coupling constant α_i to be probed in the region still allowed by the $g-2$ constraint. (see Fig. 2.6.6.) This conclusion must yet be modified to account for the momentum distribution of the target electrons which reduces even further the expected signal to background ratios. Such a calculation performed for the present experimental geometry will be discussed in Chapter 4.

5. Normalization using the Mott Scattering

When a beam of positrons strikes a solid target, Mott scattering events will occur in addition to those associated with Bhabha scattering. Mott cross section for positrons scattered by the nuclear Coulomb field is given by

$$\frac{d\sigma}{d\Omega} = \frac{(\alpha Z)^2 E^2}{4|\vec{p}|^4 \sin^4(\theta/2)}\left(1 - \frac{|\vec{p}|^2}{E^2}\sin^2(\theta/2)\right), \tag{3.5.1}$$

where θ is the scattering angle and $\vec{p}$ is the initial momentum of the positron. Mott scattering of the positrons can be utilized to normalize the Bhabha scattering cross section. This will be necessary, since we cannot count all the incident positrons in the beam dump. The divergence of the positron beam increases as it passes through the target by multiple scattering and some of the positrons are lost before reaching the beam dump. In addition, some part of the positron beam has to pass through holes in the beam dump setup for constant energy monitoring. Hence, Mott scattering will be exploited to provide an independent normalization for Bhabha scattering.

6. Results from Experiments Performed at other Facilities

Experiments have been performed at several laboratories[76-90] to search for resonant states in positron-electron scattering. Most of these experiments looked for evidence of the process $e^+e^- \rightarrow X \rightarrow e^+e^-$, based on the principles described above. Several of them searched for the process $e^+e^- \rightarrow X \rightarrow \gamma\gamma$. A positive result was first reported by an experiment performed at the Stuttgart Pelletron.[83] However, a later run with increased sensitivity failed to confirm the original result.[91] Any positive results claimed by the remaining groups are not statistically significant. We will devote the balance of this chapter to a summary of the results from these experiments with emphasis placed on the investigations carried out at Stuttgart[83,84] and Grenoble.[86,87]

The earliest reported resonance search carried out by Erb *et al.*[76] dealt with positrons scattering from a Th target. Although the statistics were poor, the investigators reported a peak at 340 keV in the positron and electron spectra. However the experiment suffered from several flaws. First, there was present a large background of electrons produced by Compton scattering of annihilation photons with an edge at 340 keV. Thus any interpretation of a resonance signal with poor statistics at 340 keV is quite dangerous. More significantly the "resonance" disappeared when the thorium target was replaced by a tantalum target.

With the target located adjacent to the positron source there were large variations in the incident positron angles. As a result the kinematics of the individual events could not be reconstructed. Multiple scattering in the thick, high Z target only added to the difficulties. Finally in view of the large variations in incident positron angles it is hard to explain how a peak in the sum energy spectrum could have occurred. It is worthwhile noting that followup experiments[77,78] with similar setups and better suppression of the Compton scattered events, did not observe any evidence of a peak structure.

Several other experiments[79,80] did claim the existence of a peak at 330 keV. However, these experiments suffered from problems similar to those just described. For example, an experiment by M. Sakai *et al.*[80] used a positron source (^{118}Te-^{118}Sb-^{118}Sn) with several γ-transition lines, which produced conversion electrons near the observed signal, thereby making the interpretation of a resonance extremely suspect.

Two experiments with a collimated beam of positrons from a radioactive source produced contradictory results.[81,82] A.P. Mills, Jr. and J. Levy[81] used a Be target and brought the scattered positrons and electrons to a single detector with the help of a magnetic field. For a 1.8 MeV resonant state, they set a very low limit of 1 bkeV (90% confidence level) on the product of the resonant cross section and its width. von Wimmersperg *et al.*[82] used a polyethylene target and searched for coincidence events with a pair of plastic scintillators. The positrons passing through the target were counted by another plastic scintillator to provide a normalization for the Bhabha events. von Wimmersperg *et al.* reported a $5.8 \pm 2.7\%$ deviation from the expected Bhabha scattering signal at 710 keV. However, their conclusion was based on the deviation of two adjacent points from a sample of 12 points. Since the data sets were not repeated, it is difficult to attribute too much confidence to their conclusion.

In all of the experiments we have considered thus far, the kinematics of the individual events were not known since the experiments employed positrons over a wide range of energies and/or angles. The experiments which we will now describe[83 -87] remedied this problem either by the use of magnetic fields to produce momentum selection or by the *moderation* and the subsequent acceleration of the positrons to produce energy selection. (We will describe the latter technique in more detail in the next Chapter.) Since the energy resolution of fixed-target experiments is limited by the motion of the target electrons, the energy or momentum resolution of the incident

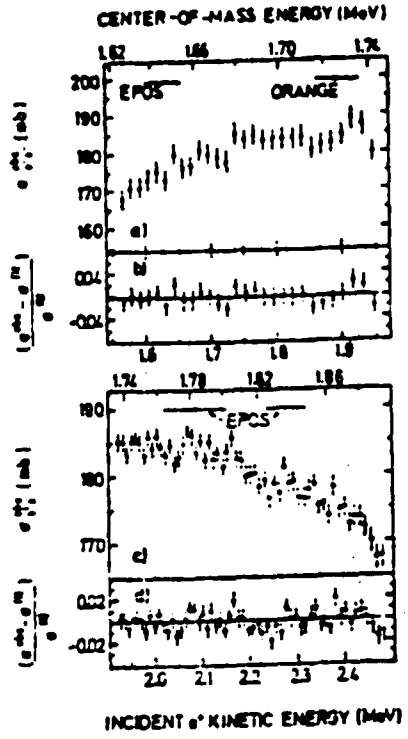

Figure 3.6.1 Observed e^+e^- scattering cross section for scattering from a 9.2 mg/cm^2 thick beryllium target. Also indicated are the expected location of the resonance from the EPOS and ORANGE lines. (b),(d) Deviation of the observed cross sections in (a),(c) from respective fits to a second order polynomial.[85]

beams in these studies did not have to be much better than the limit set by the motion of the target electrons.

E. Lorenz *et al.*[85] used a spectrometer consisting of a double focusing bending magnet to select positrons from a ^{82}Sr-^{82}Rb source. The positron beam was focused onto a Be target. An array of 19 hexagonally shaped plastic scintillators situated behind the target and having 2π solid angle coverage in the center-of-mass frame identified the scattered e^+e^- pair. Backgrounds were estimated from data obtained with the target removed. With positron

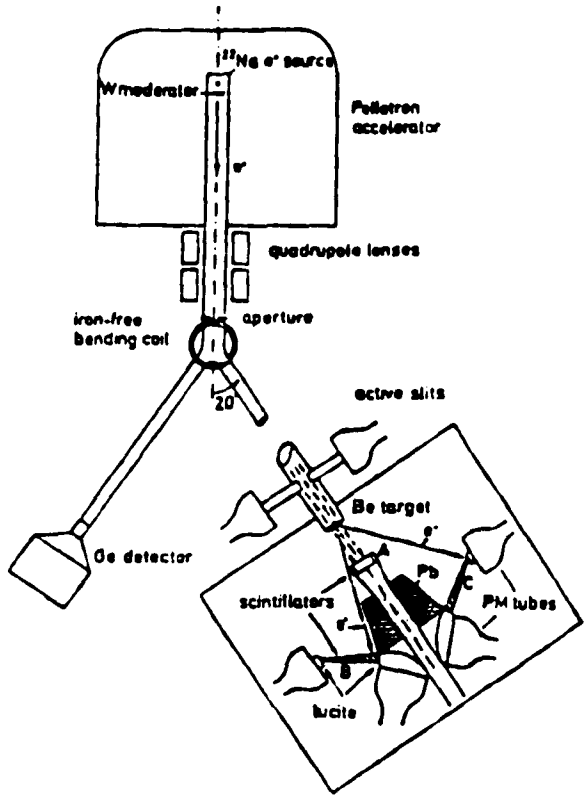

Figure 3.6.2 Setup for the Stuttgart experiment. A denotes the normalizing counter and B and C denote the position sensitive scintillators.[84]

intensities at the target varying from 150 to 1300 e^+/s coincidence rates ranged from 300 to 2000 per hour. A total of 1.1×10^5 events were collected for energies between 1.55 and 1.95 MeV in steps of 15 keV, and 9.8×10^5 events were collected for energies between 1.92 and 2.48 MeV in steps of 10 keV. The result of Lorenz *et al.* is reproduced in Fig. 3.6.1. With a statistical accuracy of 1.6% for center-of-mass energies between 1.62 and 1.74 MeV and 0.8% for those between 1.74 and 1.89 MeV (Fig. 3.6.1(b),(d)), respectively) no significant deviations from expected signals are apparent.

In an experiment carried out at Stuttgart,[83,84] positrons from a 26-33 mCi ^{22}Na source were thermalized in a thin (3-5 μm) tungsten moderator

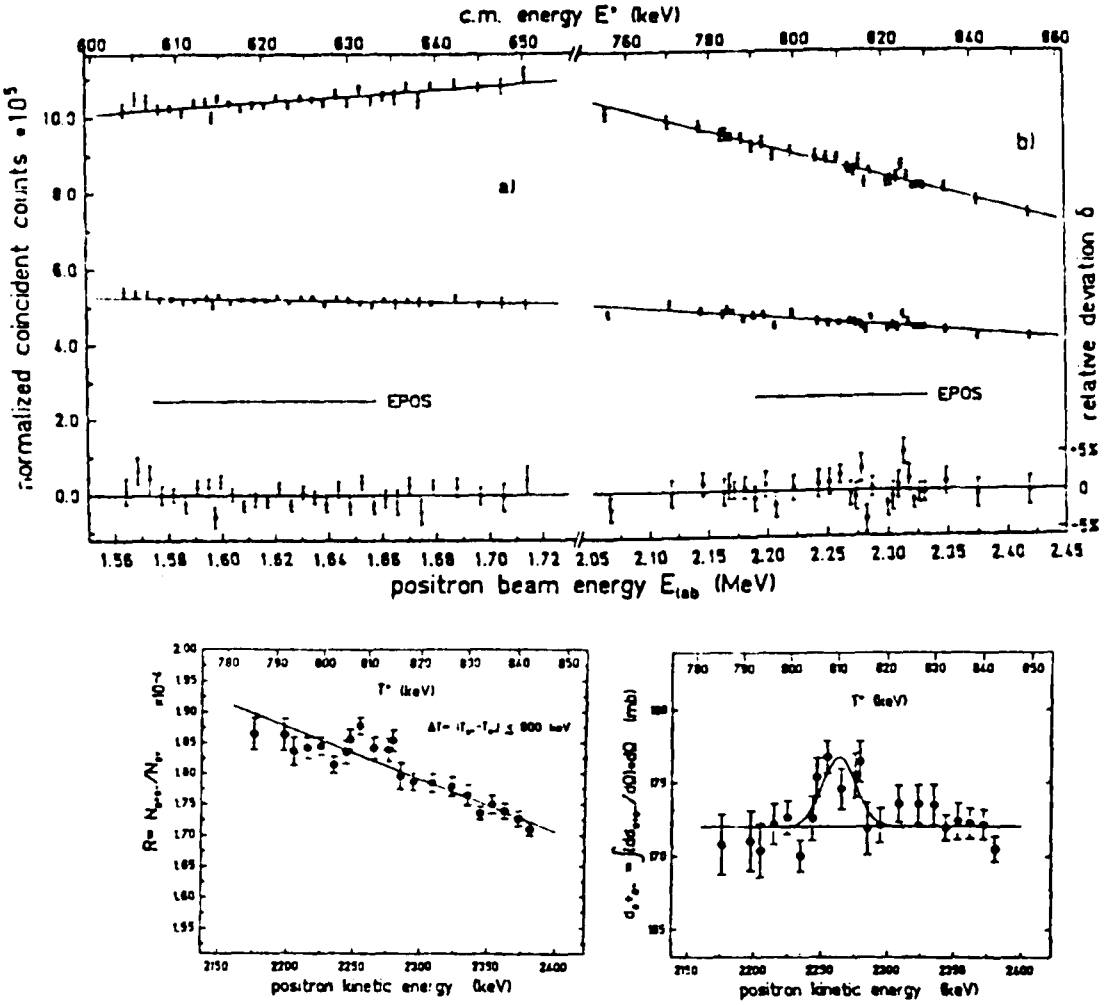

Figure 3.6.3 (a),(b) Normalized e^+e^- coincident events for the two energy regions studied. Top: Data and fits for the full angular range of the detectors. Middle: Data and fits for the scattering angles around 90° (center of mass). Bottom (right scale): Relative deviation of the data points from the fit for the full angular range. (c) Normalized e^+e^- coincidence rate for the scattered e^+e^- energy difference below 800 keV. The full line shows the best fit. (d) Experimental e^+e^- scattering cross section. The horizontal line represents the weighted mean of the data excluding the region between 2245 and 2285 keV. A Gaussian fit to this excluded region gave 2263 ± 4 keV and 27 ± 2 keV for the position and FWHM, respectively.[84]

and accelerated in a Pelletron accelerator. The accelerated beam was deflected 20° and focused onto a target to produce a final beam size of 5 mm. The energy of the beam was determined by reversing the current in the 20° bending coil, thereby steering the beam to a germanium detector.

The Stuttgart group employed a conical axially symmetric plastic scintillator as shown in Fig. 3.6.2 to identify e^+e^- events. The scintillator signals were read out by several photo-multiplier tubes, and the ratio of their pulse heights was used to identify the position of the scattered e^+ or e^- events. The experimental setup had angular resolutions of $\Delta\theta = 2.4°$ and $\Delta\phi = 8°$ over the ranges $17° \leq \theta \leq 44°$ and $0° \leq \phi \leq 360°$. The e^+ beam stopped in a central scintillator (A in Fig. 3.6.2) was used for normalization. Additional normalization information was provided by a Mott scattering signal. Typically the beam intensity was 1.2×10^4 e^+/s.

The first Stuttgart experiment[83] used a Mylar target. With the beam energy scanned in steps of 5-10 keV, the Stuttgart group collected 3-4 $\times 10^3$ coincident events for each energy point and reported no statistically significant deviation from the expected Bhabha scattering signal at the energies suggested by the EPOS results. The result is reproduced in Figs. 3.6.3(a) and (b).

The second Stuttgart experiment[84] used a Be target and scanned the beam energy over the region 2.175-2.625 MeV in steps of 10 keV. With 8×10^3-2×10^4 e^+e^- events collected per data point, the Stuttgart group obtained the results shown in Figs. 3.6.3(c) and (d). The normalized e^+e^- coincidence rate, with the energy difference between the scattered particles

kept below 800 keV, is shown in Fig. 3.6.3(c). The excess event rate between 2245 keV and 2285 keV with respect to the linear fit (solid line) shown appears as 4.7 standard deviations. The experimental e^+e^- cross section, obtained by integrating the results over the center-of-mass angles 60.7° to 119.3° at the lowest energy and 59.2° to 120.8° at the highest energy, is shown in Fig. 3.6.3(d). A Gaussian fit to the cross section over the energy range 2245-2285 keV yields values of 2263 ± 4 keV and 27 ± 2 keV for the position and FWHM of the peak structure respectively.

In yet a third experiment,[91] the Stuttgart group performed the experiment with increased positron intensity. With a factor of 4 improvement in the positron intensity, they collected $1 - 3 \times 10^5$ coincident events at positron energies in the range $2170 - 2370$ keV in steps of 6 keV. The Stuttgart group conclude that there is no structure at a level of 1% in contradiction to the second experiment.

In an experiment performed at Grenoble[86,87] positrons were produced in a titanium target covered in the center by a platinum foil that was exposed to thermal neutrons from a high flux beam reactor. The positrons are mainly produced via external conversion caused by high-energy γ rays from the $^{48}Ti(n_{th},\gamma)^{49}Ti$ reaction. The platinum foil increased the positron yield due to the Z^2 dependence of the $\gamma \longrightarrow e^+e^-$ production process. A double focusing β-spectrometer provided momentum discrimination of the resulting positron beam focused onto a beryllium foil. The positron beam had a typical intensity of 8×10^5 e^+/s. The coincident e^+e^- pairs were sensed by 4 Si(Li) detectors, placed symmetrically with respect to the beam direction at

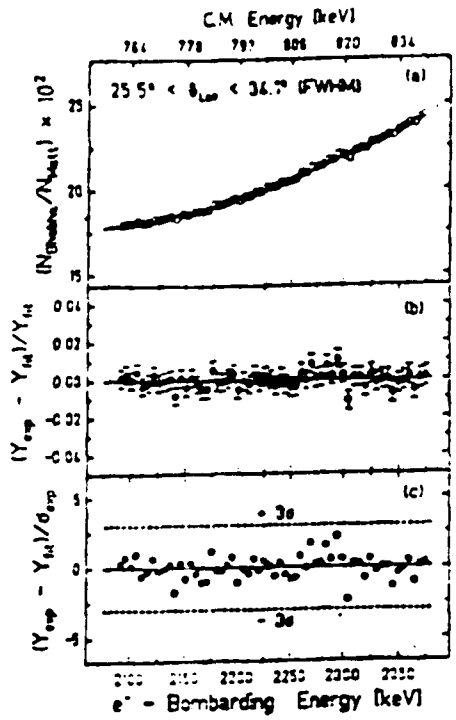

Figure 3.6.4 (a)Ratio of Bhabha to Mott scattering as a function of the bombarding energy. The solid line is a fit of a simple smooth function to the data. The relative as well as the standard deviations from the fitted curve are shown in (b) and (c), respectively.[87]

a distance of 85 mm from the target. The Grenoble experiment scanned an energy region from 2.1 to 2.4 MeV in steps of 5 keV. With Mott scattered e^+ events employed for normalization, the Grenoble group obtained the ratios of Bhabha to Mott cross sections shown in Fig. 3.6.4. At a statistical accuracy of 0.5% they observed no resonant scattering.

In an experiment at Giessen,[88] positrons were created by bombardment of a cooled tungsten converter with a 26 MeV electron beam. A magnetic monochromator system was used to select 10^7 e^+/s per 10 keV energy interval, and the beam energy was varied between 1.2 MeV and 2.3 MeV in

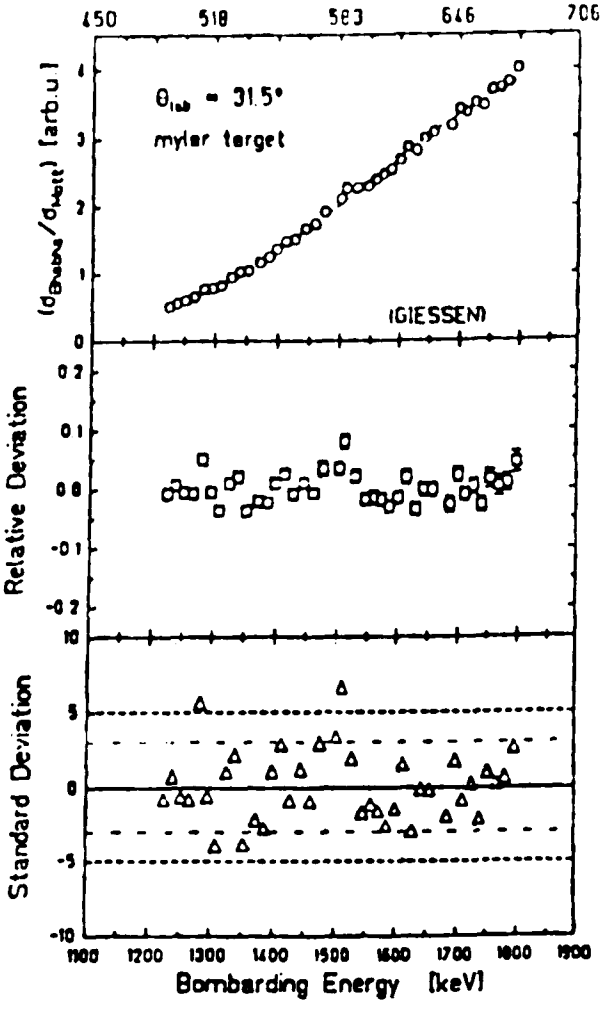

Figure 3.6.5 Ratio of Bhabha to Mott cross sections as a function of bombarding energy. Also shown are the relative and standard deviations.[88]

steps of 15 keV. Although the beam divergence was small, the beam size at the Mylar target was 6 mm × 10 mm. An array of Si detectors mounted symmetrically with respect to the beam axis was used to detect the scattered Bhabha and Mott events. Fig. 3.6.5 shows the measured ratio of Bhabha to Mott scattering cross sections as a function of the positron bombarding energy. Even though the data points show 5 standard deviation effects at some points, the Giessen group argues that their results display no structure

at a 3% level, since all the points lie within the statistical accuracy of the experiment.

An alternate approach to the resonance search utilizes the fact that if the X-particle were a $J = 0$ state, it could decay through the process $X \rightarrow \gamma\gamma$. (The GSI experiments did not search for this mode of X-decay, since the background radiation from the heavy ion collisions precluded any such observation.) The photon decay channel can be identified by examining the annihilation-in-flight spectra of the positrons incident on a target. This received further attention from the wrong interpretation of the photon peaks observed in the Berkley heavy-ion experiment.[92] Berkley group reported coincident photon lines in an experiment performed with super heavy ions similar to the experiments performed at GSI. However, a followup experiment found that the observed structure is caused by cascade transitions from high spin states of the heavy ion used in the scattering process.[93] Motivated by the original claim of the Berkley group two-photon spectra from the annihilation-in-flight of the positrons were recorded and searched for resonances[89,90]. There was no evidence for a structure at 3% level. In particular, this experiment sets a limit for the ratio of the partial widths for the X-particle decay into two-photon and e^+e^- channel of $\Gamma_{\gamma\gamma}/\Gamma_{e^+e^-} \leq 0.7$ corresponding to the 810 keV line observed at GSI.

Chapter 4.

Details of the Experimental Setup

1. Overview

We have already shown that for a resonance in Bhabha scattering to be sensitive at a 1% level, a monoenergetic positron beam is required. In order to meet this challenge we undertook the development of a dedicated positron beam facility at Brookhaven National Laboratory utilizing a 3 MeV Dynamitron accelerator[94] and a high-intensity source of moderated positrons. In the first sections of this chapter we will describe the techniques employed in the production, acceleration, transportation, and monitoring of the positron beam. At the end of the chapter we will describe the detector and data acquisition system which we developed for the Bhabha experiment.

2. Positron Beam Production

The most commonly used positrons for the low-energy beam production come either from photon pair conversion in a high energy accelerator[95] or from radioactive decay of nuclei.[96] At Brookhaven, much effort has been devoted to the latter approach since the early 1980's, and for the purposes of our Bhabha experiment it seemed to be an appropriate approach. In

light of this decision we will not dwell at length on an accelerator based positron production. Suffice to say that when energetic electrons are decelerated in matter, photons are emitted through the bremsstrahlüng process. Positrons can be produced (along with the electrons) by the pair conversion of these photons, when the photon energy is in excess of twice the electron rest mass. This technique has been used effectively at Lawrence Livermore Laboratory.[95]

The Positron Source

The most commonly used radio-isotopes in positron beam facilities[96] are ^{64}Cu, ^{58}Co, and ^{22}Na. The ^{64}Cu isotope is rather short lived ($\tau_{1/2} \sim 12.8$ hours) and is used only when it can be employed immediately after its production, thus necessitating easy access to a local nuclear reactor. On the other hand, the ^{58}Co and ^{22}Na isotopes have long half-lives (71 days and 2.602 years respectively). Hence facilities utilizing these sources require only long-term servicing. Another criterion to be considered in the selection process of a source is the e^+ branching ratio. The e^+ branching ratios [(number of e^+ emissions)/(total number of decay emissions)] for ^{22}Na and ^{58}Co are 0.89 and 0.15, respectively. Based on both half-life and branching ratio considerations, ^{22}Na is a better choice as a source material. The decay scheme of ^{22}Na is shown in Fig. 4.2.1(a).

Commercially available ^{22}Na sources (supplied by du Pont, New England Nuclear) have a maximum strength of 150 mCi. As we will see shortly the efficiency of a monoenergetic positron beam production from a primary

source typically ranges between 10^{-3} and 10^{-4}. Hence, commercial sources cannot produce the intensity required (at least 3×10^5 e^+/s) for our experiment. As a consequence, a development program was undertaken at Brookhaven to produce an intense, high e^+ yield ^{22}Na source.[97] Safety measures necessary for use in an accelerator environment dictated encapsulation of the source as well as stringent operating procedures.

The source capsule design, reproduced[97] in Fig. 4.2.1, utilizes a titanium body and a $5 - 6$ μm-thick titanium window which is welded to the body. The capsule is closed with a tantalum plug which maximizes the backscattering of positrons in order to increase the positron yield. The capsule design provides an adequate volume for the neon gas that evolves from the ^{22}Na decay. The integrity of the window seal was checked under pressure of up to 5 atmosphere, with a subsequent helium leakage measurement of 10^{-8} torr-l/sec.

The source material in solution form was deposited on the titanium window and allowed to evaporate. Solutions of NaCl were tried but were found to result in non-uniform deposition. Ultimately, an aqueous solution of sodium acetate deposited over ashless filter paper (which provides nucleation sites) was found to produce a homogeneous source distribution. Unfortunately, the exposure to radiation caused significant deterioration to the filter paper causing unwanted material to be deposited in the source. Nevertheless, the advantage of the homogeneity achieved with this method far outweighed the disadvantage of the decrease in the positron yield that results from e^+ absorption by the residue left behind.

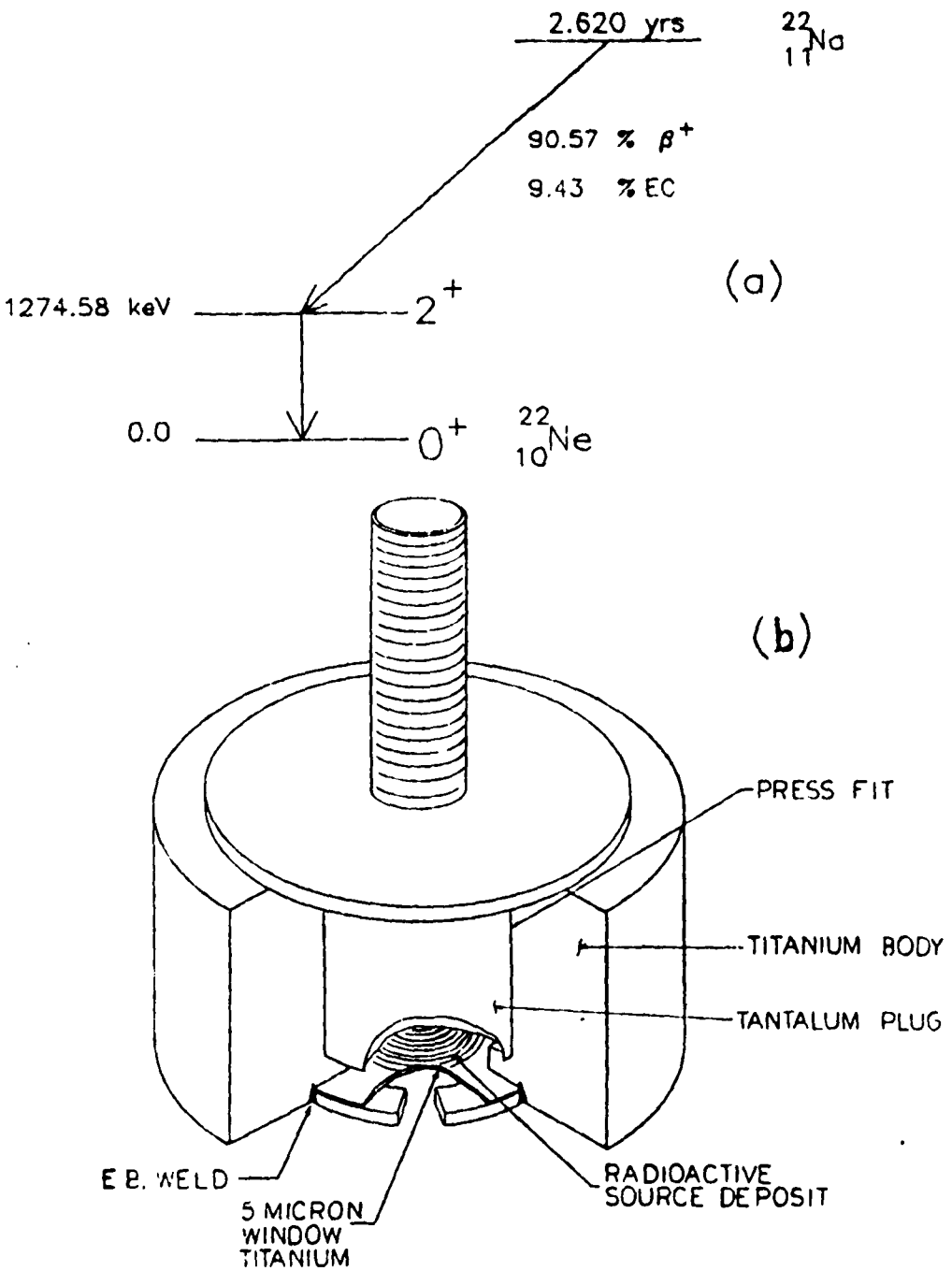

Figure 4.2.1 (a) The Decay scheme of ^{22}Na and (b) the schematics of ^{22}Na source capsule.

The deposition on the capsule window was carried out by repeatedly adding small drops of about 20 μl of the source solution and letting the solution dry for about 30 minutes at 60 $^{\circ}C$. The positron and the gamma ray yields of the source were measured after each deposition, the separation of positrons and gamma rays being achieved with the use of a scintillator with movable shutter. (The shutter stopped all the positrons emitted from the source; hence when the shutter is closed the scintillator counted only gamma rays.) The source capsule which we used in our experiment had an activity of 250 mCi with 16 % positron emission. The active area of the source was 6 mm in diameter.

Moderator

Radioactive decay of ^{22}Na atoms produces positrons over a wide range of energy with the distribution having the shape of the usual β-decay spectrum and characterized by an end-point energy of 546 keV. In order to produce a monochromatic positron beam from this spectrum, a technique known as "moderation" was developed several years ago.[98] The discovery of the moderation process revolutionized the low energy positron beam technology by reducing both the mean energy and the energy spread of the positrons and enhancing the usable portion of the positron spectrum.[98]

The moderation process is usually achieved by the use of an annealed crystaline material, placed in front and around the radioactive source. These moderator materials have a ϕ_+, for positrons that are inherently negative work functions.[98]

The positron work function of a material is defined as the minimum energy required to take a positron from a point inside the material to the vacuum outside. The work function has a bulk contribution and a surface contribution. The former is the positron chemical potential, μ_+, a positive quantity which arises from a combination of the repulsive force produced by the ion cores and the attractive force produced by the electrons. The surface contribution, called the surface dipole potential barrier, D, is due principally to the tail of the electron distribution at the surface-vacuum interface. For positrons the surface dipole barrier is negative and directed out of the solid. The combined effects of μ_+ and D, (which have opposite signs) can produce a negative value of ϕ_+ for some materials. For such materials, the positrons that reach the surface after thermalization in the bulk, will be emitted into the vacuum even though they have very low energies when they reach the surface. The result is the emission of a "monoenergetic" low-energy positron beam having a longitudinal energy $e\phi_+$ and a spread in transverse energies characteristic of the multiple scattering processes that produced the thermalization in the bulk material.

The efficiency, ϵ, of a moderator is dependent upon three factors:[99] the probability, $P_{im}(z)$, of a positron becoming thermalized within a small range dz at a distance z from the surface; the probability, $P_{diff}(z)$, of the thermalized positrons diffusing to the surface; and the probability, $P_{em}(z)$, of these positrons being emitted after reaching the surface. The first probability, $P_{im}(z)$, is given by

$$P_{im}(z) = \mu exp(-\mu z), \tag{4.2.1}$$

where μ, the absorption coefficient of the material is related to the density ρ of the moderator material and to the endpoint energy, E_{max}(in MeV) of the positron spectrum according to the empirical expression

$$\mu = 1.7\rho/E_{max}^{1.14}. \tag{4.2.2}$$

The diffusion probability, $P_{diff}(z)$, is given by

$$P_{diff}(z) = exp\Big(-\frac{z}{z_d}\Big), \tag{4.2.3}$$

where z_d, the positron diffusion length is related to the diffusion coefficient, d, and the life time, τ, of the positron in the material according to $z_d = \sqrt{2d\tau}$. The efficiency is obtained from an integration of the product of the three probabilities over all values of z:

$$\begin{aligned} \epsilon &= P_{em}\mu \int_0^\infty exp\Big((-\mu + \frac{1}{z_d})z\Big)dz \\ &= \frac{P_{em}\mu z_d}{(1+\mu z_d)} \\ &\simeq \frac{1.7P_{em}\rho\sqrt{d\tau}}{E_{max}^{1.14}}. \end{aligned} \tag{4.2.4}$$

The final form of Eq. (4.2.4) is obtained with the approximation that the diffusion length is much less than the mean implantation depth, an approximation that is valid for most metals and other dense materials.[99] Eq. (4.2.4) identifies the qualities of a good positron moderator: a large positron diffusion coefficient, d; a long positron lifetime, τ; a high density, ρ ; and a high probability, P_{em}, of positron emission from the surface.

The diffusion coefficient is maximized by selecting a crystaline material of high perfection and by removing defects (which can trap the positrons) through annealing. Since positron lifetimes are similar in all solid media (100-200 ps), τ is not a deciding factor in selecting a good moderator. The emission probability, a function of surface properties, is measured by allowing a low-energy positron beam to strike the surface of the moderator. The measured fraction of positrons reemitted then determines P_{em}. (Usually P_{em} is about 30% with 70% of the positrons trapped at the surface or emitted as positronium.) While the endpoint energy also plays a role, it is not significant enough to change the selection of the source material in our case.

The historical developments of the various moderator materials can be found in Refs. 98 and 99 and will not be discussed here. Instead, we will describe the results of a recent study at Brookhaven[100] of several thin-film moderators. The moderation efficiencies of different thin films (0.3 to 7 μm thick) were measured for tungsten, nickel, tantalum, molybdenum, niobium, and copper. Single crystals of tungsten and nickel gave the highest efficiencies of $5.9(3)\times10^{-4}$ and $6.6(3)\times10^{-4}$ respectively. Although the nickel crystal showed a higher initial efficiency, it was found to degrade fast when exposed to a bad vacuum. The efficiency of a tungsten crystal was found to be enhanced when the source of positrons are backed with a tungsten sheet. The enhancement is attributed to the increase in the number of the positrons from backscattering. The data showed that the moderator efficiency increases as the thickness of the single-crystal decreases. With the lower limit on

the thickness determined by practical considerations, we chose single crystal tungsten 1 μm thick as the moderator.

There are two kinds of geometries that can be employed in the moderation of the positrons; namely, reflection and transmission. In the reflection geometry, the moderator resides behind the source and the moderated positrons are reemitted from the same surface through which they entered the moderator. Hence the central part of the moderator surface will be shadowed by the source capsule and will result in a distorted initial beam.

In the transmission geometry, the moderator is placed in front of the source capsule, and the moderated positrons escape through the surface opposite to the source, thus eliminating the shadowing produced by the first scheme. Since the source capsule does not interfere with the moderated positrons, the transmission geometry also facilitates better electromagnetic field configurations for extraction of the moderated positrons. For both of these reasons we used a transmission mode for moderation at the Brookhaven Dynamitron beam facility.

The positron beam emerging from the moderator is characterized[101] by a mean longitudinal kinetic energy of 3 eV and an angular spread that is governed by the transverse energy of the emitted positrons. At room temperature, the measured energy width (FWHM) is $\simeq$ 75 meV which corresponds to an angular spread of $\pm 10^{\circ}$ about the normal to the surface of the moderator. The initial beam diameter is approximately 8 mm.

Source Chamber

Source chamber houses the source-moderator holder and is the first part of the injector system for the accelerator. The source chamber is designed to meet the space constraints imposed by the accelerator terminal and is optimized for easy insertion and removal of the source-moderator holder. The source-moderator holder can be inserted remotely to ensure low radiation exposure to the personnel. Since, the accelerator is mounted vertically, the weight of the tantalum source-moderator holder employed for the enhancement of backscattering and hence positron yield, provides sufficient force for vacuum seal.

When the accelerator is turned on after a shut down, the high voltage is turned on in accordance with a prescribed *conditioning* process. Since the conditioning causes a corona and an increase in the radiation in the accelerator column, the source chamber is provided with a moving flap arrangement, which can cover and protect the moderator from the radiation damage.

3. The Design and The Fabrication of The Filter System

The moderation process creates monochromatic, low-energy positrons with excellent initial properties as explained in the previous section. However, a large component of high-energy positrons will be present along with the moderated positrons. The high-energy positron contamination is caused by the use of a transmission moderator. Since the moderator is only $1\mu m$

thick, the high-energy end of the ^{22}Na spectrum passes through the moderator with very little energy loss. Fig. 4.3.1 shows a schematic representation of the positrons emitted from the ^{22}Na source with and without the moderator present.

In order to remove the unmoderated part of the positron spectrum, a filter system was developed. Ideally, the filter system should select all the moderated positrons and should discard the remainder of the spectrum. At the Dynamitron, we were able to eliminate 99.99% of the unwanted positrons at the injection stage while retaining most of the moderated beam. Following acceleration and transport to the experimental chamber, we found that the high energy contamination was less than two ppm.

At low-energy positron beam facilities, several techniques are commonly employed to isolate the moderated positrons from the rest of the spectrum. They include transporting the moderated positrons away from the source region with the use of an axial magnetic field; filtering the moderated positrons with the use of crossed electric and magnetic fields; and reflecting the moderated positrons through 90° with respect to their initial trajectories with the use of an electrostatic mirror. For our application, we found all of these methods wanting, either due to incompatible spacial requirements or due to the difficulties created[102] by having a magnetic field present at the accelerator terminal. Instead, we chose to use the limited space available in the vertical direction at the accelerator terminal to install a 75-cm long electrostatic filter section between the source chamber and the entrance to the accelerator.

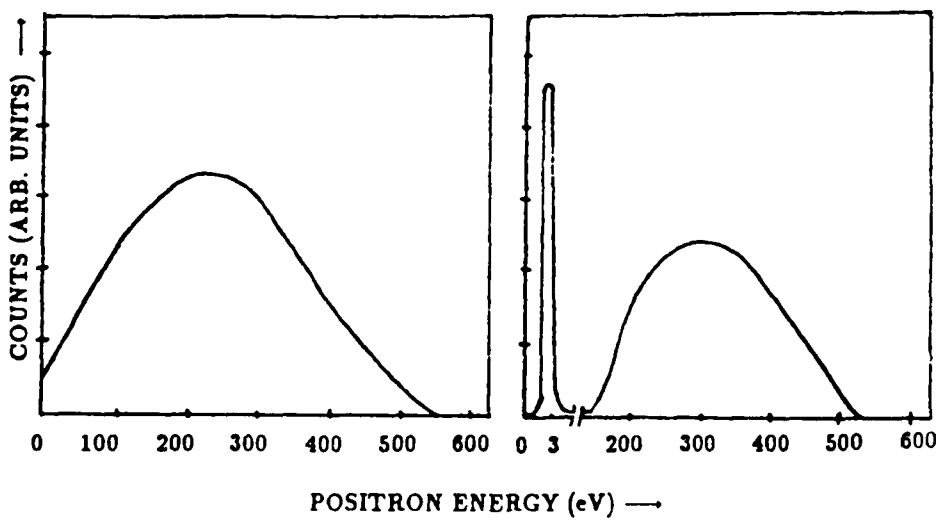

Figure 4.3.1 (a) The positron spectrum of ^{22}Na decay before the moderator and (b) after the moderator as a function of energy (not to scale).

The filter system consists of a modified Soa immersion lens[103] and a pair of symmetrical einzel lens which respectively extracts and transports the moderated positrons. The low-energy moderated positrons are focused by these lenses through a small aperture ($\simeq$ 6 mm in diameter) at the exit of the filter section. Since the lens elements operate at relatively low voltages, the trajectories of the high-energy positrons are not changed appreciably by the filter section. Thus the high-energy contamination is reduced by a factor which depends on the solid angle acceptance of the aperture with respect to the ^{22}Na source. A long filter section will decrease the solid angle of acceptance and will cut down unwanted positrons. The length of

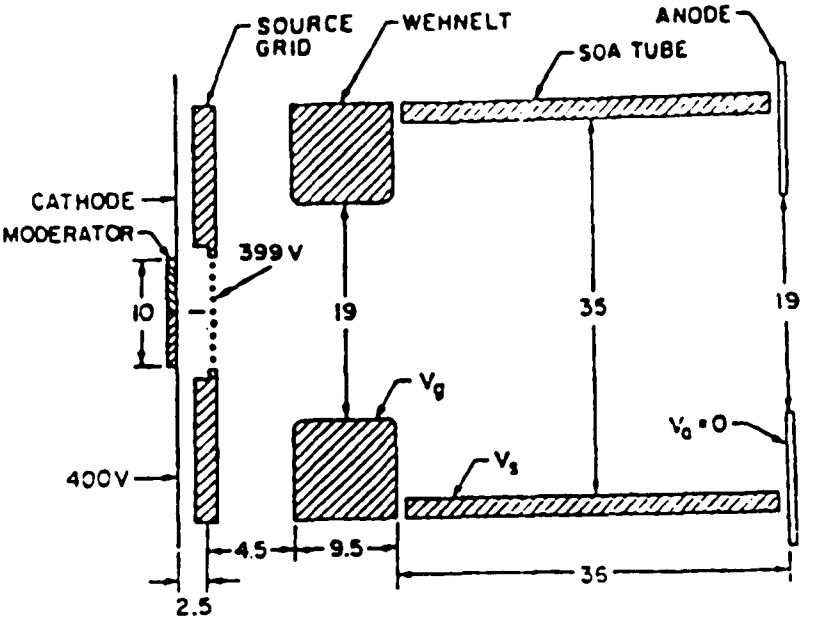

Figure 4.3.2 Modified Soa gun. All dimensions are in mm. The wehnelt electrode has a 1.5 mm radius rounded edge.[103]

the dynamitron filter section is 75 cm (the maximum space available at the terminal) which produces a filter factor of 10^{-4}.

Prior to construction, we modeled the filter lens in detail with the use of the SLAC Electron Trajectory Program.[104] Adapted from a previous study,[103] the Soa geometry which we employed as our first stage lens, is a modified version of an immersion lens with an additional tube element, as illustrated by Fig. 4.3.2. The introduction of the Soa tube prevents the punch-through of external fields from the nearby grounded surfaces and provides one more degree of freedom in controlling the positron trajectories. In addition, the Soa tube keeps the size of the lens small, without which

the separation between the Wehnelt and the anode planes would force the selection of a much larger diameter ($\simeq$ 15 cm) for the lens system. Since the properties of the modified Soa immersion lens were studied at length previously,[103] we used existing tabulations of exit trajectory characteristics as input for the SLAC computer code.

The Soa immersion lens provides a 400-V acceleration for the positrons prior to accelerator injection. Since the positron intensity is low, the space charge effects can be neglected. For our application we found that optimum performance is achieved with the following choice of lens voltages, all given with respect to ground: moderator or cathode = 400 V, Soa grid = 399 V, Wehnelt = 390 V, Soa tube = 280 V, and anode = 0 V. Fig. 4.3.3 shows the trajectories of the positrons for launches from the moderator with the above values for the lens parameters. The trajectories shown include the extreme rays corresponding to a radius, r, of 4 mm and half angles, θ, of $\pm 10°$.

According to the Liouville's theorem,[105] the phase space volume of a set of charged particles is conserved. The phase space volume is defined by the space occupied by the charged particles in the six dimensional coordinate-momentum space. For particles with low transverse energy, almost all of the particles will be confined to a region near to the beam axis. Under these conditions, the momentum portion of the phase space can be replaced by the half angle of divergence of the rays with respect to the beam axis. Thus the Liouville's theorem can be re-expressed in terms of the maximum radius r, at an image of the beam source and the maximum half angle, θ, at the same axial location. The product of r and θ is called the "emittance", and

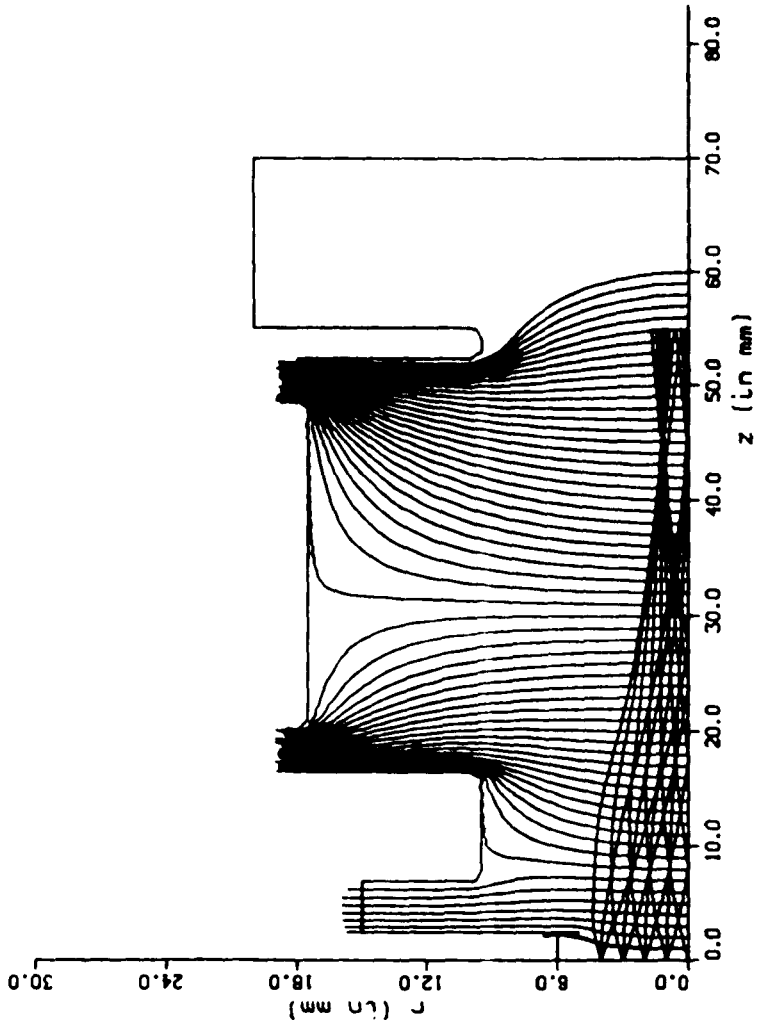

Figure 4.3.3 Trajectories of moderated positrons through the modified Soa lens system calculated with the use of the SLAC Electron Trajectory Program (Ref. 104). The trajectories corresponds to launches from $0, 1, 2, 3,$ and 4 mm and angles $0°, \pm 10°$ and they travel from left to right. The lines starting from the axis and going up are the equipotential lines.

Liouville's theorem states that for a given beam energy the emittance is conserved. When the energy of a beam is changed, the emittance scales inversely with the energy. Thus, if a beam is accelerated from an energy E_i to an energy E_f, the emittance is reduced by the factor $\sqrt{E_i/E_f}$. For our application, the emittance of the beam at the exit of the Soa lens will be reduced by the factor $\sqrt{3\ eV/400\ eV} \simeq 0.09$ with respect to that at the moderator surface. Assuming an initial emittance of $\sim$ 700 mrad·mm ($r \simeq 4$ mm, $\theta \simeq \pm 10°$) for 3 eV positrons, the emittance for 400 eV positrons should be $\sim$ 65 mrad · mm. The SLAC ray trace program in fact yielded values of $\sim$ 1.65 mm for r and $\sim$ $\pm 3°$ for θ at 400 eV which corresponds to an emittance of 87 mrad · mm, slightly larger than the predicted value. The discrepancy is due to the limited number of rays used and the limited size of the mesh points used in deriving the potential distribution in the SLAC program analysis.

The Soa lens is followed by a pair of symmetrical einzel lenses, which are designed to focus the moderated positrons at the exit of the filter system. A symmetrical einzel lens, an example of which is shown in Fig. 4.3.4 provides focusing without changing the beam energy. It consists of a short tube element sandwiched between two longer tubes. The outer tubes have the same voltage and hence the name *symmetrical* einzel lens is applied. The geometry of an einzel lens is simple enough not to demand a detailed ray trace analysis and can be studied using a transfer matrix method.[106]

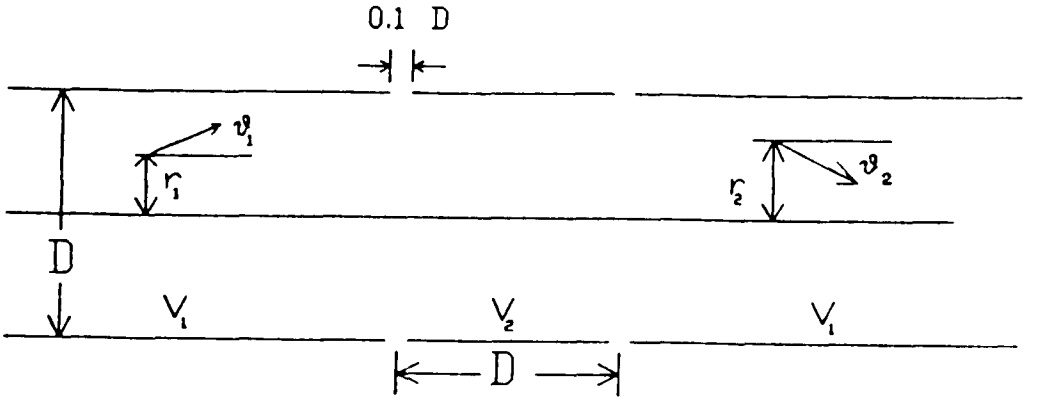

Figure 4.3.4 A schematic diagram of a symmetrical einzel lens. D is the diameter of the tube and V_1 and V_2 denotes the voltages on the tube elements and r and θ denote the trajectory height and the angle with respect to the beam axis.

For a positron entering the lens from the left (location 1 in Fig. 4.3.4), the trajectory at the exit (location 2 in Fig. 4.3.4) can be obtained by applying the simple matrix equation

$$\begin{pmatrix} r_2 \\ \theta_2 \end{pmatrix} = (T) \begin{pmatrix} r_1 \\ \theta_1 \end{pmatrix}, \tag{4.3.1}$$

where r and θ denote the trajectory height and the angle with respect to the beam axis, as shown in Fig. 4.3.4, and T is a 2×2 matrix known as the transfer matrix. The FORTRAN subroutine used for calculating the transfer matrix appropriate for the filter design was taken from the listing

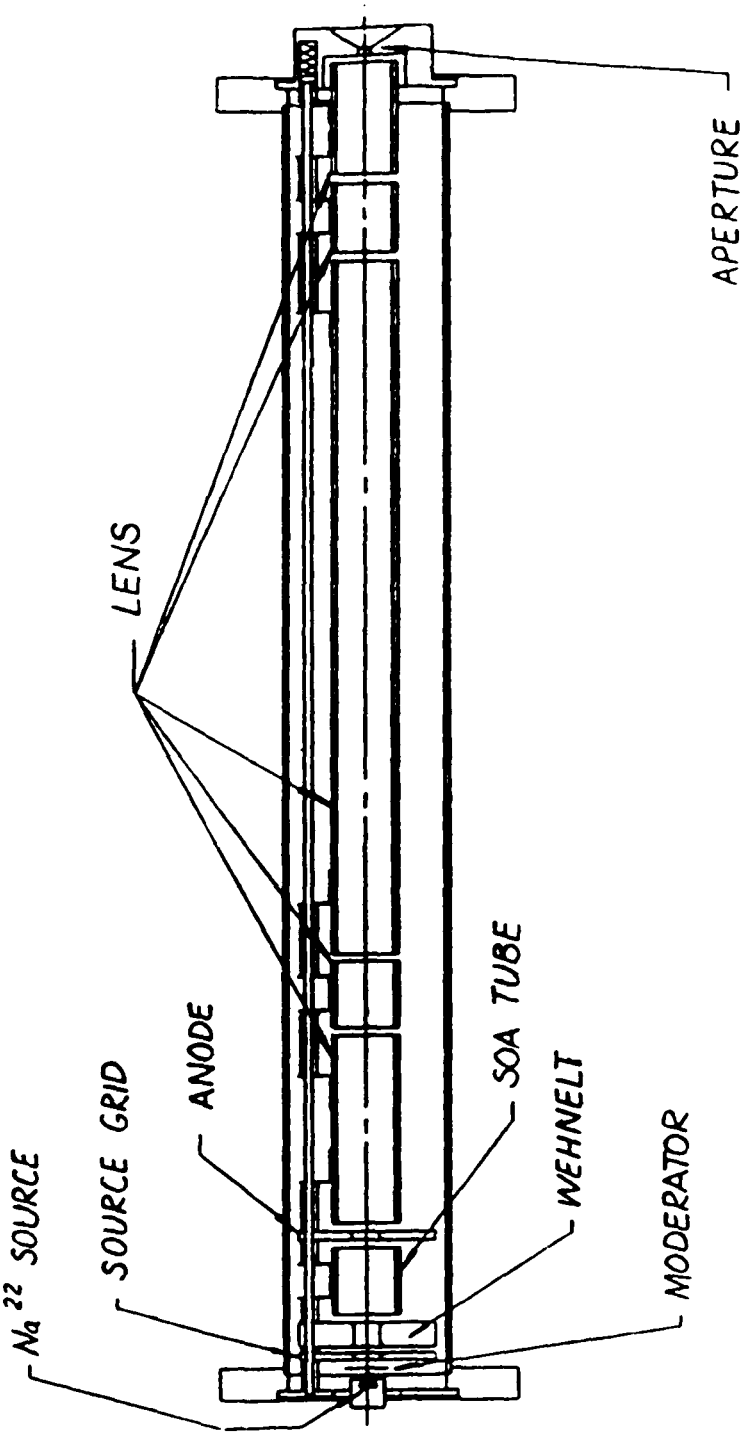

Figure 4.3.5 A schematic diagram of the filter section.

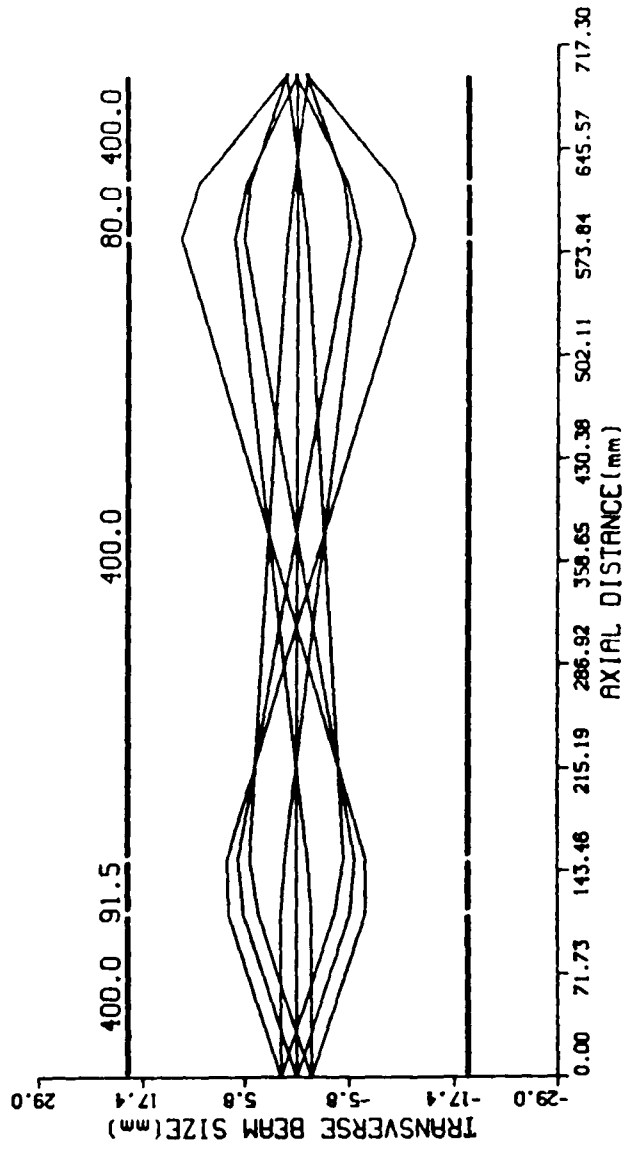

Figure 4.3.6 The trajectories of the extreme rays through the filter system. Also listed at the top are the corresponding voltage values for each lens element.

given in Ref. 106. We found that for a 75-cm long filter, an optimized design required two einzel lenses. A schematic diagram of the filter section is shown in Fig. 4.3.5. Since the outer tube element of each lens is long compared to its diameter, the lenses can be regarded as non-interacting.

Ray tracing through the free space between the lenses involves multiplication by a simple matrix:

$$\begin{pmatrix} r_2 \\ \theta_2 \end{pmatrix} = \begin{pmatrix} 1 & L \\ 0 & 1 \end{pmatrix} \begin{pmatrix} r_1 \\ \theta_1 \end{pmatrix}. \tag{4.3.2}$$

Here L is the length of the drift space and the entry and exit points are again denoted by 1 and 2. A program which incorporated the matrix of Eq. (4.3.2) as well as the transfer matrix T was used to determine the positron trajectories. The program varied the voltages on the lens elements to optimize the final beam properties. Fig. 4.3.7 shows the trajectories of the extreme rays through the filter system for the optimized lens voltages found. The beam parameters at the exit of the filter section are

$$\begin{aligned} r &\simeq 1.218 \text{ mm} \\ \theta &\simeq \pm 5^\circ, \end{aligned} \tag{4.3.3}$$

the small inflation of the emittance again is attributed to the approximation of the phase space envelope by the properties of the extreme rays.

4. The Acceleration

The Dynamitron accelerator[94] is an electrostatic, high-voltage accelerator, designed to provide a charged particle beam in the energy range of

0.5 to 3.0 MeV. The main components of the accelerator are the acceleration column, the rectifier stack, the corona rings, the high voltage terminal, and the radio frequency oscillator system. The accelerator is located inside a pressure vessel filled with SF_6 gas at 76 atmosphere pressure to suppress sparks and corona discharges.

The accelerator column shown in Fig. 4.4.1 consists of a chain of 96 dynodes, which are designed to have high pumping speed and good wall shielding, requirements that are somewhat contradictory. The structure of the dynodes provides excellent shielding of the beam from the insulator sections between dynodes and avoids charging of the insulator during prolonged operation of the accelerator.

The corona rings are fabricated from cylindrical aluminium stick which has been polished and bent into a semicircular shape. The radius of the semicircle permits the rings to be mounted on a circumference that encompasses the accelerator column and the attached rectifier stack. The corona rings not only act to suppress sparks, but also provide the coupling capacitance through which the radio frequency power is transmitted to the rectifier stack. When the tank vessel is closed, a set of large, semi-cylindrical electrodes (known as D plates) completely surround the high-voltage column and energize all the rectifier stages equally through the mutual capacitance between the D plates and the corona rings. The rectified voltage is fed to a resistor chain which is tapped to power the dynode chain. The high voltage is divided equally among the dynodes.

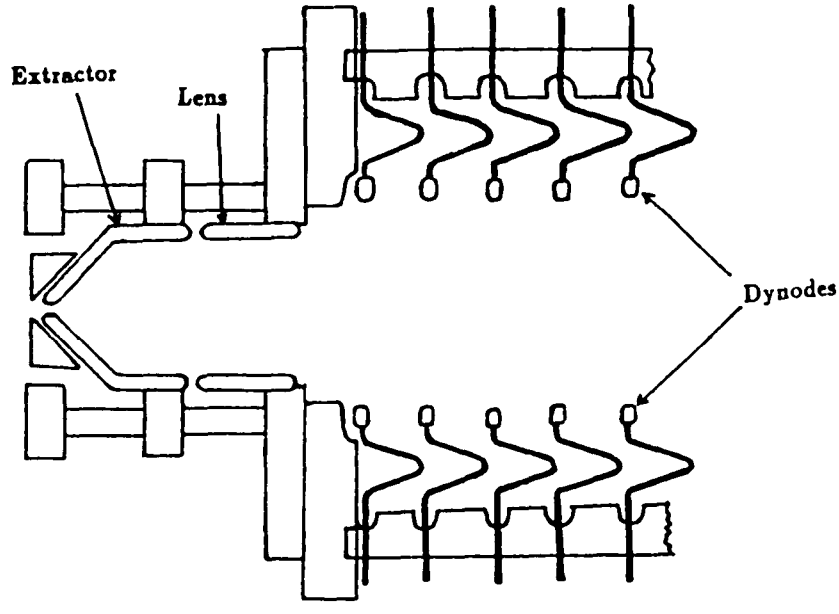

Figure 4.4.1 The injection stage of the accelerator showing the first few dynode chains.

The high-voltage terminal requires a low-voltage source to power the injector system. Since the terminal resides at a very high voltage, it is impossible to bring the power in on cables which originate at essentially ground potential outside the tank. Hence, a motor situated at the bottom of the accelerator tank is used to drive a generator at the terminal. The generated voltage is rectified before applying to the various elements of the injector system.

When a beam of charged particles is injected into an accelerator column, it is automatically focused by the accelerating field. In order to provide some control over the focusing, additional tuning electrodes are incorporated

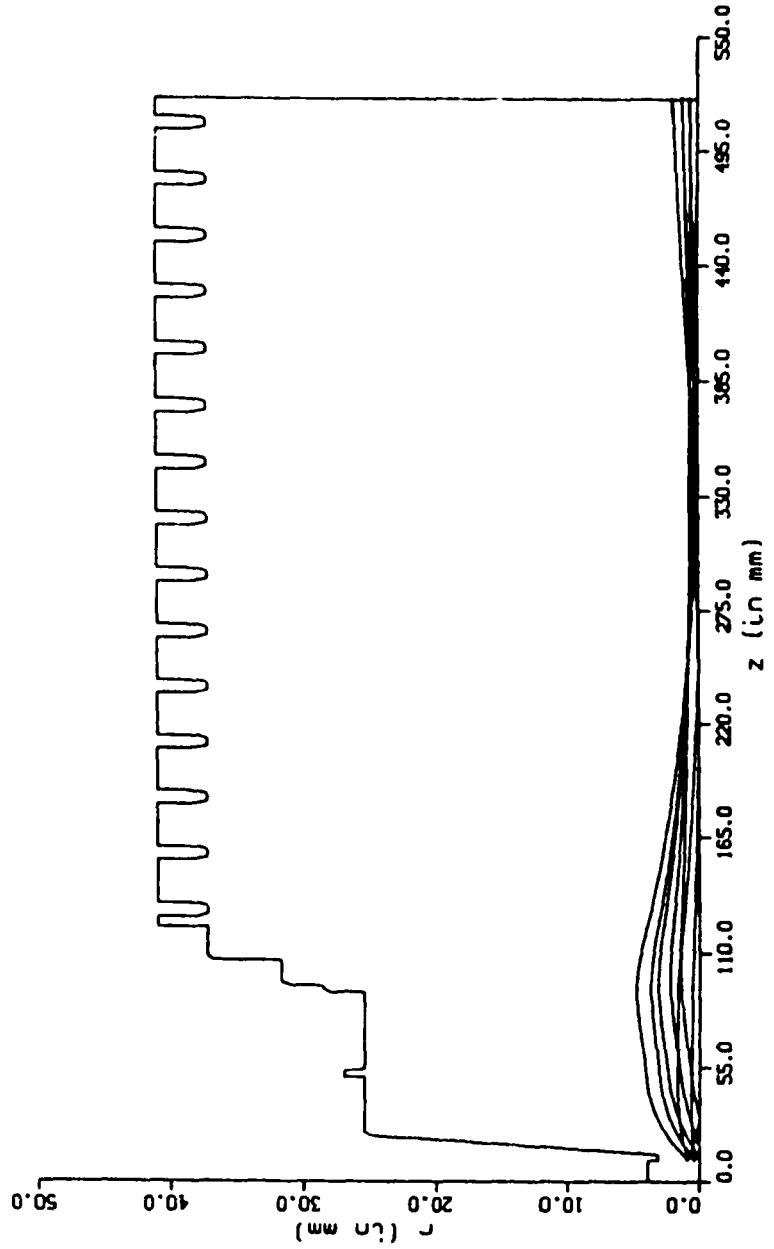

Figure 4.4.2 The trajectories of positrons during the initial stage of the acceleration for a final beam energy of 2.2 MeV. The extractor and lens voltages are 1600 V and 4700 V, respectively.

into the injector stage. We retained these elements, called the "extractor" and "lens" in the Dynamitron manuals, and in spite of some ambiguity in the meaning, we continued to use the same nomenclature. A schematic diagram of these injector elements along with the first few dynodes of the accelerator are shown in Fig. 4.4.1.

With the use of the SLAC program,[104] we traced the positrons through the system up to the 15^{th} dynode of the accelerator. We tried various combination of extractor and lens voltages to improve the quality of the accelerated beam. The resulting trajectories of the positrons for a final beam energy of 2.2 MeV at the exit of the accelerator is reproduced in Fig. 4.4.2. At this point the beam envelope is characterized by a radius and a divergence given respectively by

$$r \simeq 1.2\text{mm} \quad \text{and} \quad \theta \simeq 42.0\text{mrad}. \tag{4.4.1}$$

The remaining part of each positron trajectory involves only acceleration and can be determined from the simple matrix transfer equation

$$\begin{pmatrix} r_2 \\ \theta_2 \end{pmatrix} = \begin{pmatrix} 1 & \frac{L(\gamma_1+\gamma_2)}{\gamma_1(R+1)} \\ 0 & \frac{\gamma_2}{\gamma_1 R} \end{pmatrix} \begin{pmatrix} r_1 \\ \theta_1 \end{pmatrix}, \tag{4.4.2}$$

where L is the acceleration length, $\gamma_1 = \frac{E_1}{mc^2}$, $\gamma_2 = \frac{E_2}{mc^2}$, $R = \sqrt{\frac{\gamma_2^2-1}{\gamma_1^2-1}}$, and E_1 and E_2 are the respective energies of the positrons at the initial position r_1 and the final position r_2. At the exit of the accelerator column there is a small defocusing effect. The accelerated positron beam at an energy of 2.2 MeV is characterized by an emittance of 6mrad · mm.

5. The Beam Transport System

The accelerated beam has to be transported to the target area, which is approximately 11 m away from the exit of the accelerator. Since the accelerator is oriented vertically a 90° bending of the beam is necessary. The use of a bending magnet is beneficial to the energy character of the beam, since the dispersion can be employed to remove the remaining unmoderated positrons. In order to achieve this goal and to ensure that the beam size and divergence at the target be kept as small as possible, conditions required for unambiguous kinematic reconstruction of the scattered events, we carried out a detailed study of the beam transport system with the help of the program TRANSPORT.[107]

The accelerated beam is symmetric in the transverse plane. One of the design criteria is to preserve this symmetry as much as possible during the beam transport. Hence, instead of quadrupoles, we used solenoids for beam focusing. We benefited from using solenoid lenses in other ways as well. If misaligned, solenoids distort the beam properties less than quadrapoles under similar conditions. Moreover, solenoid lenses typically must produce stronger fields than those produced by quadrapoles under similar focusing applications. Thus the focusing properties of solenoids are less susceptible to distortion by stray magnetic fields. Before providing the details of the beam line design, we will describe the operating principles of a solenoid lens. We will also review the characeristics of a double focusing bending magnet.

The Solenoid Lens

A solenoid is the most often used focusing element in a transport system for a beam comprising low-energy particles. If the length of the solenoid is finite, fringe fields will be present, in addition to an axial field, thereby producing a radial component which depends on both the axial and radial coordinate of the charged particle. It can be shown that,[108] for a charged particle, traversing the solenoid the equation of motion is given by

$$\frac{d^2r}{dz^2} = -\left(\frac{e}{8mV}\right)B_z^2 r, \tag{4.5.1}$$

where, eV is the energy of the beam, B_z is the axial field, z is the axial distance, and m is the mass of the charged particle.

We have used cylindrical coordinates in Eq. (4.5.1), since the solenoid and presumably the beam have cylindrical symmetry. The negative sign in the equation implies that there is a force driving the particle towards the axis. Since the driving force is directly proportional to the distance of the particle, r, from the axis, a focusing effect results. It should be noted that the force is proportional to the square of the magnetic field. Hence, reversing the magnetic field by reversing the current in the solenoid windings will not change the direction of the force. In other words, there will be no change in the focus when the direction of the field is reversed. Although the image of the beam is rotated when it passes through a solenoid for our purpose the effect has little consequence since our beam is symmetric in the transverse plane.

The Double Focusing Bending Magnet

There are two functions that a bending magnet can serve in a beam line. The obvious one is to change the direction of the beam and, for example, direct it to a particular experimental area. The second is to provide dispersion or correlation of the transverse position with the momentum of the beam particle. The dispersion allows the selection of a restricted range of momenta to be transmitted to the experimental area.

An ordinary bending magnet has its field boundary normal to the reference trajectory at the entrance and the exit face of the magnet. (A reference trajectory is the central trajectory of the beam and is used to specify any other trajectory traversing the beam line.) Such a magnet has a focusing effect in the bending plane, which destroys the symmetry of the beam in the transverse plane.

The focusing of an ordinary bending magnet can be understood with the aid of Fig. 4.5.1(a). A particle entering the magnet outside the reference trajectory spends more time in the magnetic field, resulting in a larger deflection compared to that of the reference trajectory. Similarly, a particle entering the magnet inside the reference trajectory is deflected less compared to the reference trajectory. Hence, the trajectories on either side of the reference trajectory in the bending plane are deflected towards the reference trajectory. The net result is a focusing effect in the bending plane.

In the transverse plane (perpendicular to the bending plane), the trajectories experience almost the same field, when the fringe fields are neglected. Hence, no focusing occurs in the transverse plane. A bending

magnet, such as the one shown in Fig. 4.5.1(a) thus breaks the cylindrical symmetry of the beam.

It is possible, however, to restore the symmetry in both planes, by constructing a bending magnet with a modified pole face. If a field boundary is introduced which is not perpendicular to the reference trajectory at the entrance and the exit face, as shown in Fig. 4.5.1(b), focusing can be produced in the transverse plane. Such a non-normal boundary is often referred to as a *rotated pole face.*[105,109] The pole face rotation angles of the entrance and the exit face are defined as the angle at the pole face between the normal to the pole boundary and the reference trajectory. The angles are labelled as β_1 and β_2 and are defined as positive if magnet iron is removed for the trajectories outside the reference trajectory and added for the trajectories inside.

The use of rotated pole faces affects trajectory behaviour in both the bending and the transverse planes. In the bending plane, the effect of a pole face rotation is defocusing, since a particle entering the magnet on either side of the reference trajectory is bent away from the reference trajectory, as can be understood from Fig. 4.5.1(b). However, in the transverse plane the addition of the pole face rotation has a focusing effect due to the fringe fields present at the pole face.[105] By proper choice of β_1 and β_2 it is possible to have identical focusing effects in both planes. For a 90° bend, the proper values are,[109] $\beta_1 = \beta_2 = 26.57°$. Such a bending magnet capable of focusing in both planes is called *double focusing bending magnet.*

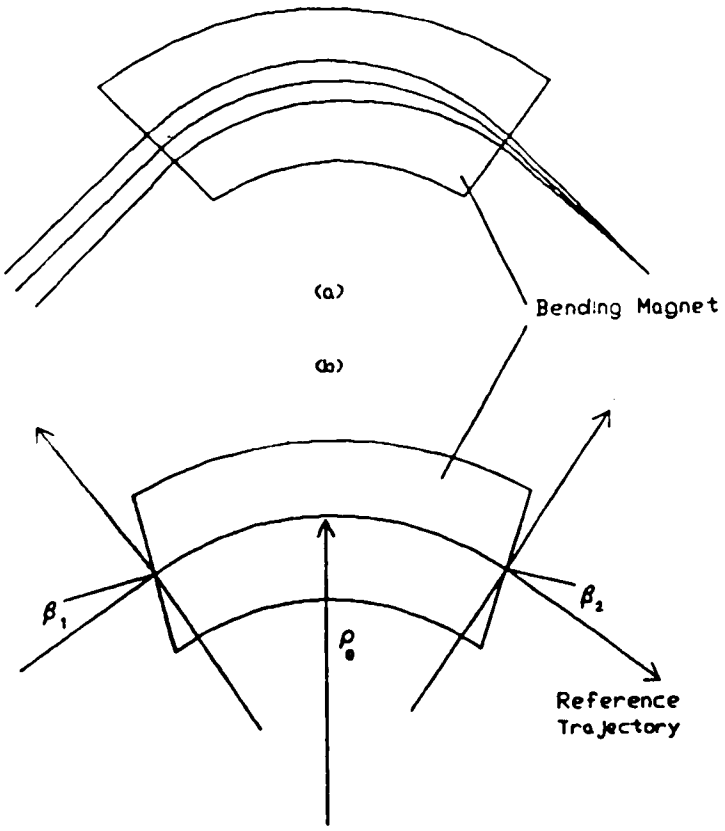

Figure 4.5.1 (a) A bending magnet showing the focusing effect in the bending plane, and (b) a bending magnet with non-zero entrance and exit pole face rotation.

The focal length[105] of a double focusing, 90° bending magnet is twice the radius of curvature, ρ. Hence, if a beam of charged particles is brought into focus at a distance 2ρ from the entrance pole face of the magnet, an image will be formed at a distance 2ρ from the exit pole face. The focal points are called object and image points, analogous to the terminology used for optical lenses.

For a double focusing, 90°-bending magnet the dispersion of the beam due to momentum spread is $4\rho \times \frac{\Delta p}{p}$, where Δp is the excess momentum of any trajectory compared to the momentum p of the reference trajectory.[105] As we just noted, when a beam is brought to a focus at the object point of the magnet, ideally it will be focused at the image point. The ideal condition will hold, however, only if all the particles have the same momentum in which case there will be a one to one correspondence between the object and the image plane. On the other hand, for practical situations, a particle with a slightly different momentum will take a different path through the bending magnet, resulting in a dispersion at the image point. With the incorporation of an image-point collimator system, we used the dispersion property of the magnet to remove any residual high-energy contamination of our beam, as will be described in detail in a later section.

The TRANSPORT Program and The Beam Line Design

TRANSPORT[107] is a computer program suitable for use in the design of magneto-static beam transport systems. It employs first-order and second-order matrix multiplication techniques and has fitting capabilities to

produce an optimum solution. The program has provision for treating the misalignment of the magnet systems and the momentum dispersion of the beam.

The notation for the coordinates used by the program is summarized as follows. The longitudinal coordinate (which is along the reference trajectory) is denoted by z, and the transverse coordinates, by x (horizontal) and y (vertical). A charged particle can then be represented by a single column matrix X, whose components are the position, angle, and the momentum of the particle with respect to the reference trajectory:

$$X = \begin{pmatrix} x \\ \theta \\ y \\ \phi \\ l \\ \delta \end{pmatrix}. \tag{4.5.2}$$

Here x and y are the horizontal and vertical displacement of the arbitrary ray with respect to the assumed central trajectory, θ and ϕ are the angle the trajectory makes with the central trajectory in the horizontal and vertical plane, l is the path length difference between the arbitrary ray and the central trajectory, and $\delta = \frac{\Delta p}{p}$ is the fractional momentum deviation of the ray from the assumed central trajectory. The path length difference, l, is not important in our case since we are not using a pulsed beam.

A magnetic lens is represented to first order by a square matrix R. The passage of the charged particle through the system can then be represented by the matrix equation

$$X(1) = RX(0), \tag{4.5.3}$$

where $X(0)$ is the initial coordinate vector and $X(1)$ is the final coordinate vector. The combined effect of several magnetic elements and drift spaces can be obtained by successive multiplication of the appropriate matrices representing elements or drift spaces in sequence, the first element being on the extreme right and the last element being on the extreme left of the product.

In accelerator and beam transport systems, the behaviour of an individual particle is of less importance than the overall behaviour of the set of charged particles that constitute the beam. The TRANSPORT code represents the beam in phase space by an ellipsoid in a 6-dimensional coordinate space. The equation of the ellipsoid is given by

$$X(0)^T \sigma(0)^{-1} X(0) = 1, \tag{4.5.4}$$

where $X(0)^T$ is the transpose of the vector $X(0)$, and $\sigma(0)$ is a real, positive-definite, symmetric matrix. It can be shown that[107] the square root of the diagonal terms of the matrix σ is a measure of the beam size in each coordinate. The first order R-matrices for various elements used in the Dynamitron beam line can be found in Ref. 107.

The transport program can vary the parameters of the beam line elements to conform to the constraints determined by the experimental setup. For our application we impose constraints on the beam size and divergence. First we require a focused beam at the object plane of the bending magnet. The matrix elements $\sqrt{\sigma_{11}}$ and $\sqrt{\sigma_{33}}$ which corresponds to horizontal and vertical coordinates are minimized by varying the field of a solenoid placed

between the object plane and the accelerator. If the off diagonal elements of the sigma matrix are zero at any point, the ellipsoid is said to have a waist at that point. In addition to minimizing the spatial extent of the beam, the solution produces a waist at the object plane.[107,105]

The bending magnet has a radius of curvature of 25.4 cm. Since the beam is designed to focus at the object plane, the double focusing bending magnet produces an image at a distance $2\rho = 50.8$ cm from the exit pole face. The beam diverging from the image point is transported to the target area by a second solenoid, identical in design to the first solenoid. Again, the location and strength of the solenoid are determined from the requirement that there be a waist at the target.

Based upon the TRANSPORT studies we developed the beam-line configuration shown in Fig. 4.5.2. In order to facilitate beam tuning we installed steering coils at various locations along the beam line as shown in the figure. The final beam parameters at object, image, and the target locations are listed in Table 4.5.1 for three energy values. Fig. 4.5.3 shows the beam envelope along the beam line for a beam energy of 2.2 MeV.

Beam Monitoring System

In order to ensure that the beam was transported to the target area in accordance with its design specifications, we installed several beam monitoring devices, some passive and some active, at various positions along the beam line. The locations chosen were dictated in part by departures of the beam from its ideal character. For example, we found that in practice, the

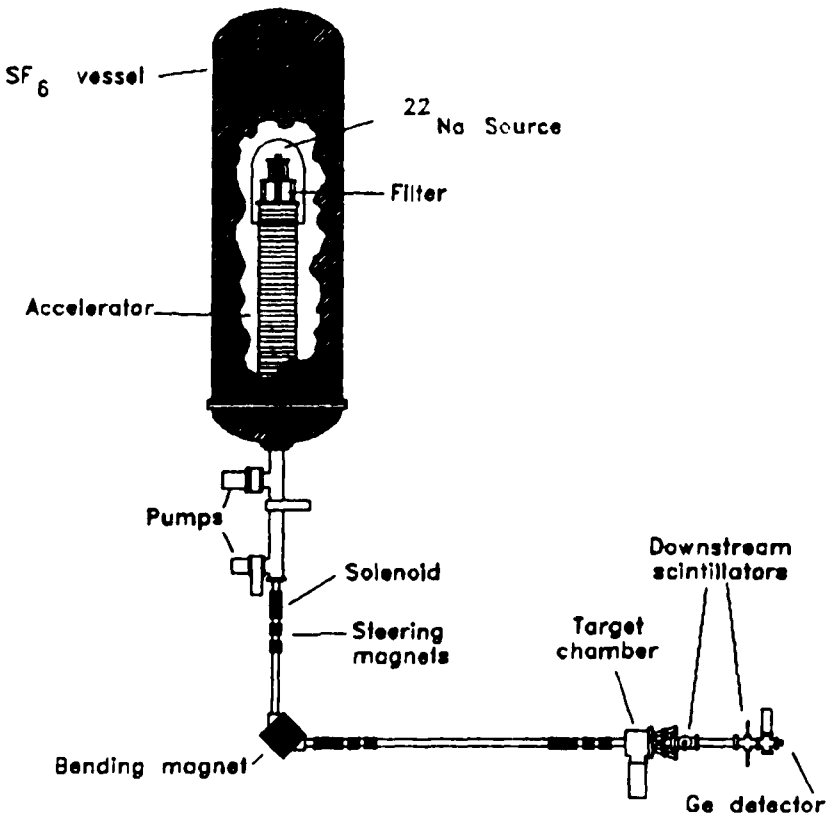

Figure 4.5.2 The layout of the Dynamitron beam transport system along with a schematic of the accelerator.

Position	x(cm)	θ(mrad)	y(cm)	ϕ(mrad)
Beam Energy = 2.0 MeV				
Object	0.12	5.0	0.12	5.0
Image	0.12	5.3	0.12	5.1
Target	0.1	14.9	0.1	14.9
Beam Energy = 2.2 MeV				
Object	0.12	5.1	0.12	5.1
Image	0.12	5.5	0.12	5.1
Target	0.1	15.0	0.1	15.0
Beam Energy = 2.5 MeV				
Object	0.12	5.2	0.12	5.2
Image	0.12	5.7	0.12	5.4
Target	0.1	15.5	0.1	15.5

Table 4.5.1 The beam size and divergence at various locations along the beam line. The symbols x, θ, y, and ϕ are explained in the text.

accelerated beam was larger in size than calculations predicted, a result that we attribute to the imperfections in the accelerating column. In addition, since the beam exiting the accelerator must travel 2.9 m, before the first solenoid, we found that the beam strayed from the nominal beam-line axis, an effect that is almost certainly due to the background magnetic fields.

In order to address these problems, we installed a passive aperture of approximate size 1.5 cm at the entrance to the first solenoid. This aperture ensured that the beam entering the first solenoid was restricted in size to a value consistent with the downstream design. We also placed a NaI detector (which detects the 511 keV gamma line from positron annihilation) outside the vacuum pipe adjacent to the aperture to permit the incoming beam to be steered onto the axis of the solenoid.

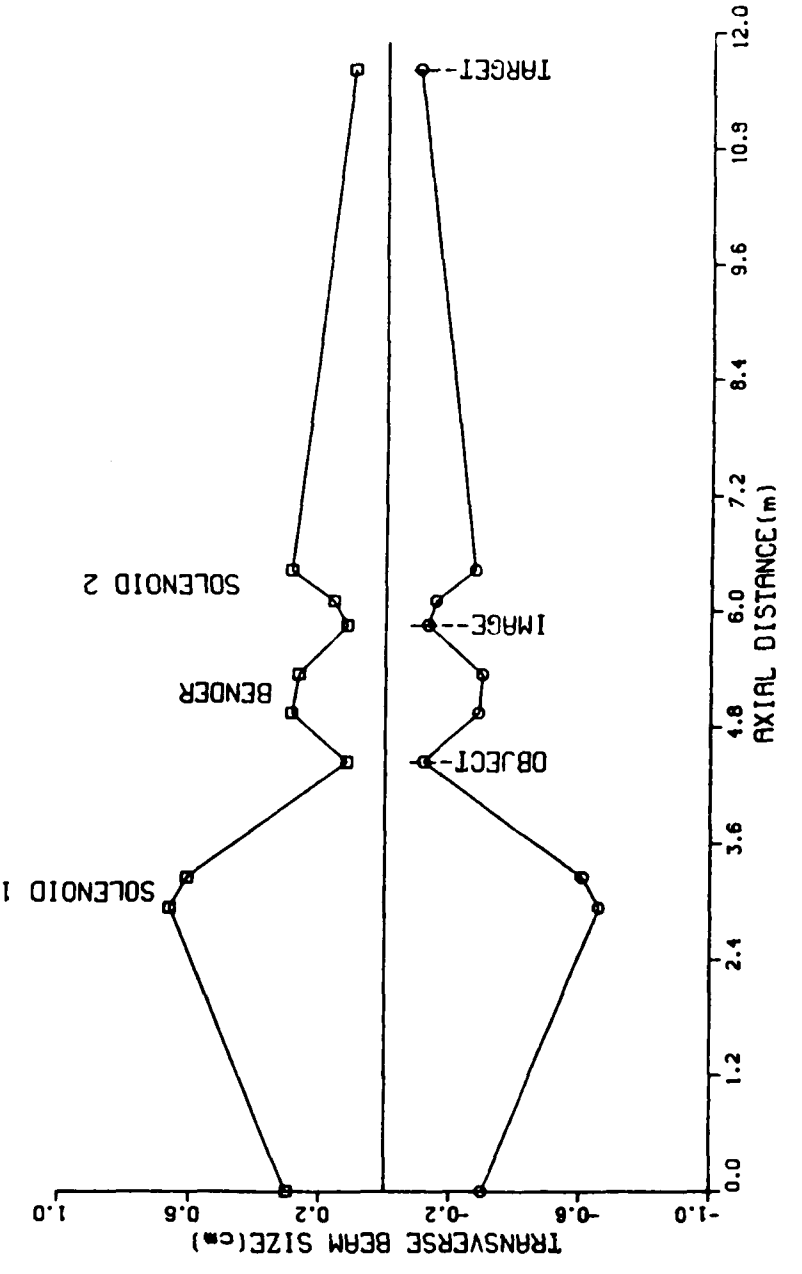

Figure 4.5.3 Beam envelope through the beam transport system for a 2.2 MeV beam.

At the object and image planes we installed active collimators. With the use of an optical telescope we were able to align the apertures of these collimators with respect to the axis of the bending magnet to an accuracy of at least ± 0.1 mm. We employed these collimators to ensure that there is indeed a waist at both focal points and, moreover, to restrict the beam pass-energy to ± 6 keV of the nominal beam energy. The active collimators mounted on xyz manipulators, were made of 12-mm thick plastic scintillators coupled to light guides and photomultiplier tubes. The scintillators can completely stop positrons with energies as high as 2.5 MeV and have a detection efficiency that approaches 100%.

We usually inspected the spatial distribution of the positron beam with the use of channel electron multiplier arrays (CEMAs) that were coupled to phosphorescent screens. The images on the screen was recorded by a high sensitivity surveillance CCD video camera and displayed at the accelerator console area. The CEMA detectors which could be moved into position manually under vacuum, were located just beyond the image collimator and at the target position. The CEMA devices could not be operated in the vertical beam section because of large backgrounds due to the ions and X-rays originating in the accelerator column.

We monitored the beam energy continuously with the use of a 7-mm thick, windowless high-purity germanium (HPGe) detector, located at the end of the beam line, as shown in Fig. 4.5.2. We calibrated the HPGe detector by observing the gamma and electron conversion-electron lines from

^{207}Bi,^{56} Co, and ^{228}Th sources. For 2.26 MeV gamma transition from ^{228}Th isotope, we determined the FWHM resolution of the detector to be 3.5 keV.

6. The Target Chamber, the Detector System, and the Beam Dump

The target chamber is designed to accommodate the detectors, the target, and the beam monitoring system. Both the CEMA (channel electron multiplier array) and the target holder can be moved under vacuum to a position on the beam axis or to a non-intrusive location off the beam axis.

The target arm is sufficiently long that it can be withdrawn into a separate small chamber that can be isolated with a valve from the target chamber to permit loading of the targets and to protect the target from contamination when it is not in use. An additional arm in the target chamber holds the calibration source and allows it to be positioned at the target location for calibration of the detector systems when required.

The downstream end of the target chamber consists of a flange, 17.5 inches in diameter, onto which the detector systems is mounted, as illustrated in Fig. 4.6.1. The flange has cutouts that are sealed with thin (50 μm thick) Kapton sheets which are supported by a mesh of tantallum wires. The sheets are thick enough to maintain the integrity of the vacuum system and yet thin enough not to destroy the kinematics of the scattered events through multiple scattering.

The detector system, optimized in design to identify the kinematics of the scattered events, consists of four multiwire proportional chambers

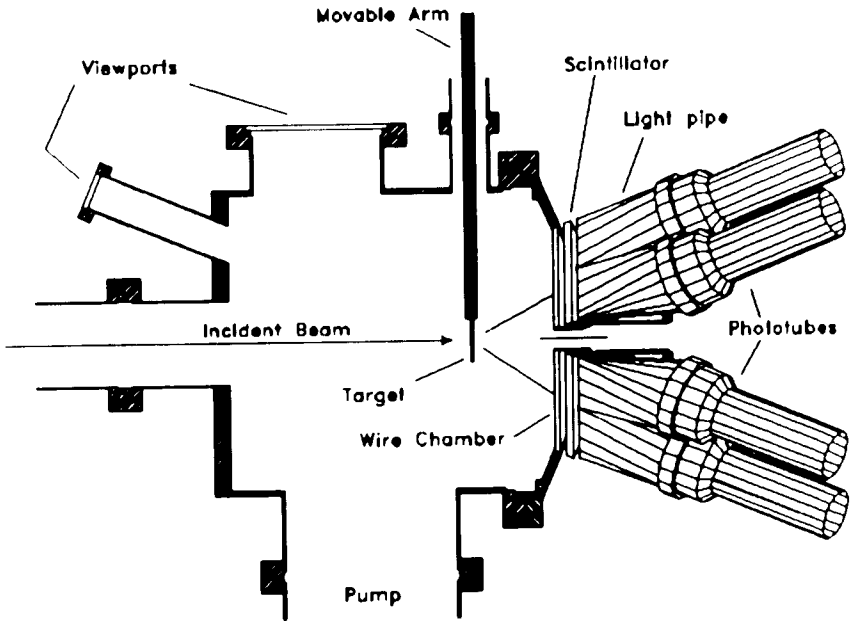

Figure 4.6.1 The target chamber showing the target arm and the detector system.

(MWPC) backed up by Bicron* plastic scintillators. The detectors are arranged in a pyramid structure, shown in Figs 4.6.1 and 4.6.2.

The MWPC's identify the scattered charged particles and discriminates against the γ-ray events originating from positron annihilation in the target. Shown schematically in side view in Fig. 4.6.3, each MWPC consists of two planes of equally spaced anode and cathode wires sandwiched between aluminized Mylar windows. The anode and the cathode plane are separated by a distance of 2.5 mm. Typical wire spacings in the anode and the cathode planes are 1.95 mm and 1.27 mm, respectively. The anode wires (20 μm in diameter) are made of gold plated tungsten and the cathode wires (75 μm in diameter), of a copper-beryllium alloy. There are 39 anode wires and 120 (in groups of 3) cathode wires.

The anode and the cathode wires are not read out separately, but rather are tied together to form a long chain with either resistors or delay lines between them. For the anode wires which employ the resistive read-out, the location of the events are obtained by charge division method.[110] For the cathode plane, which employs the delay-line read-out, the time difference between the arrival of the signals from either end is used to obtain the event location. With these read-out schemes which are are illustrated in Fig. 4.6.3 we were able to achieve position resolutions of 2 mm and 250 μm in the anode and the cathode planes, respectively, thus leading to an accuracy of

* Plastic scintillator systems is assembled by Bicron Co., USA. Hence we will call them Bicron Plastic scintillator.

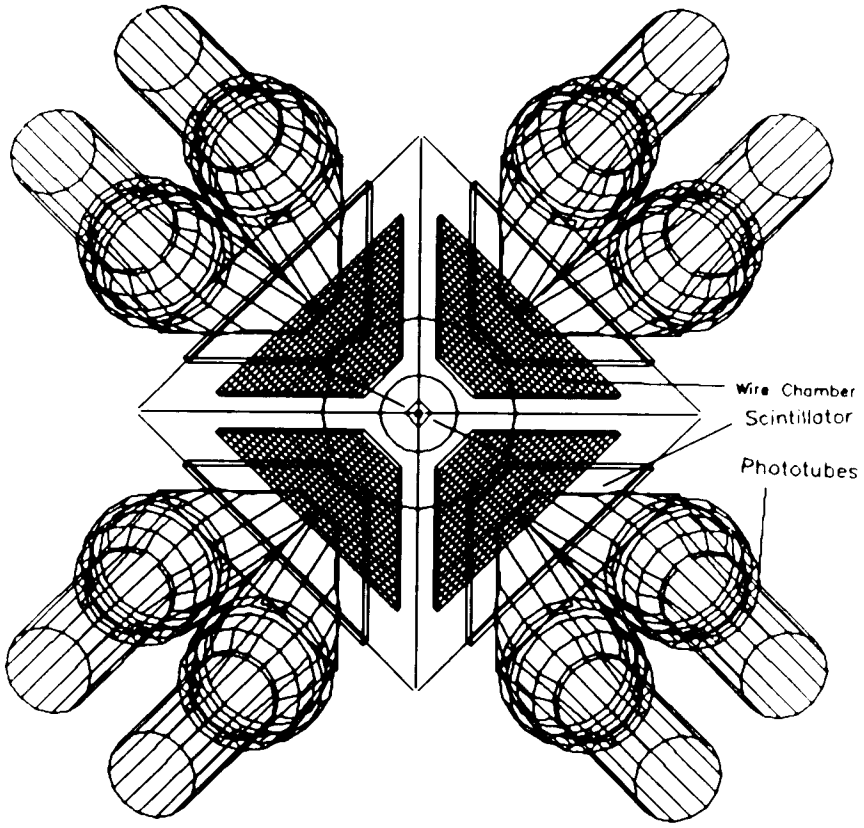

Figure 4.6.2 The geometrical arrangement of the detector system. They are arranged in a pyramid like structure with the MWPC followed by the scintillators in four quadrants.

$\pm 1°$ in the determination of the azimuthal and polar scattering angles with respect to the target.

The plastic scintillator is 1 cm thick and capable of stopping the highest energy particle in the experiment (a Mott scattered event at 2.5 MeV). The scintillator for each detector quadrant is divided into two halves and is coupled to different phototubes in order to increase the light collection. The calibration of the scintillator energies is achieved with a ^{207}Bi source at the target location. A typical calibration run is shown in Fig. 4.6.4. The response of the detector system was further studied by sweeping the detector with a positron beam, by employing a steerer magnet at the entrance of the target chamber.

Most of the beam particles passing through the target suffer only small changes in the direction of their motion. Thus they can be effectively counted in two sets of 1-cm thick scintillators located downstream from the target chamber at distances of 57 and 137 cm. Each set is split into two halves to provide positional information. A semicircular cut in each half produces a circular aperture through which part of the beam can pass through when properly tuned. The first set of scintillators having an aperture 1.9 cm in diameter, provides a horizontal read-out, while the second set, having an aperture 0.3 cm in diameter, provides a vertical read-out. The positrons passing through these holes are counted in the germanium detector for energy monitoring. Even though these beam dump counts are not used for any absolute quantitative analysis they do provide an independent monitor of the total beam intensity during a run.

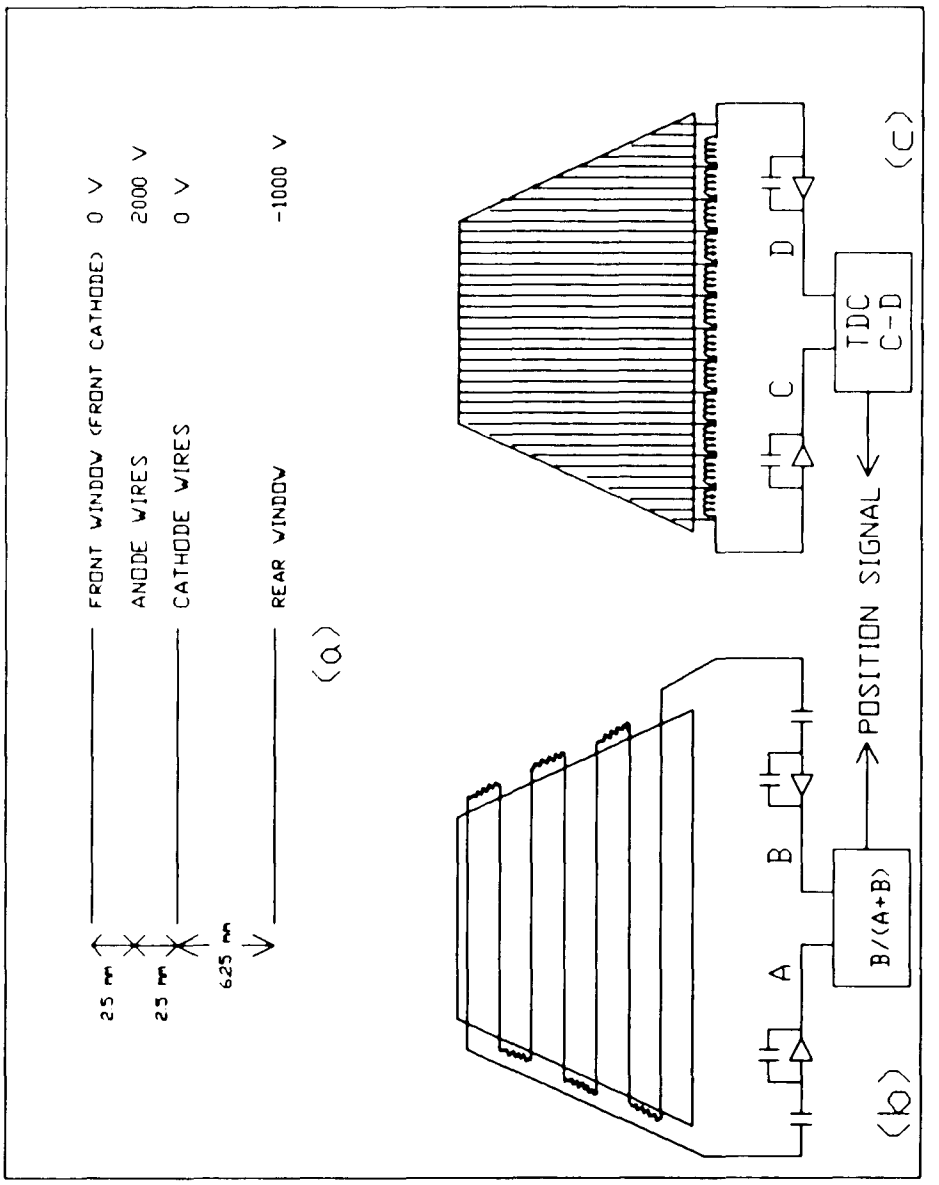

Figure 4.6.3 Schematic diagram showing (a) side view of the MWPC, (b) Anode position readout, and (c) the cathode position readout.

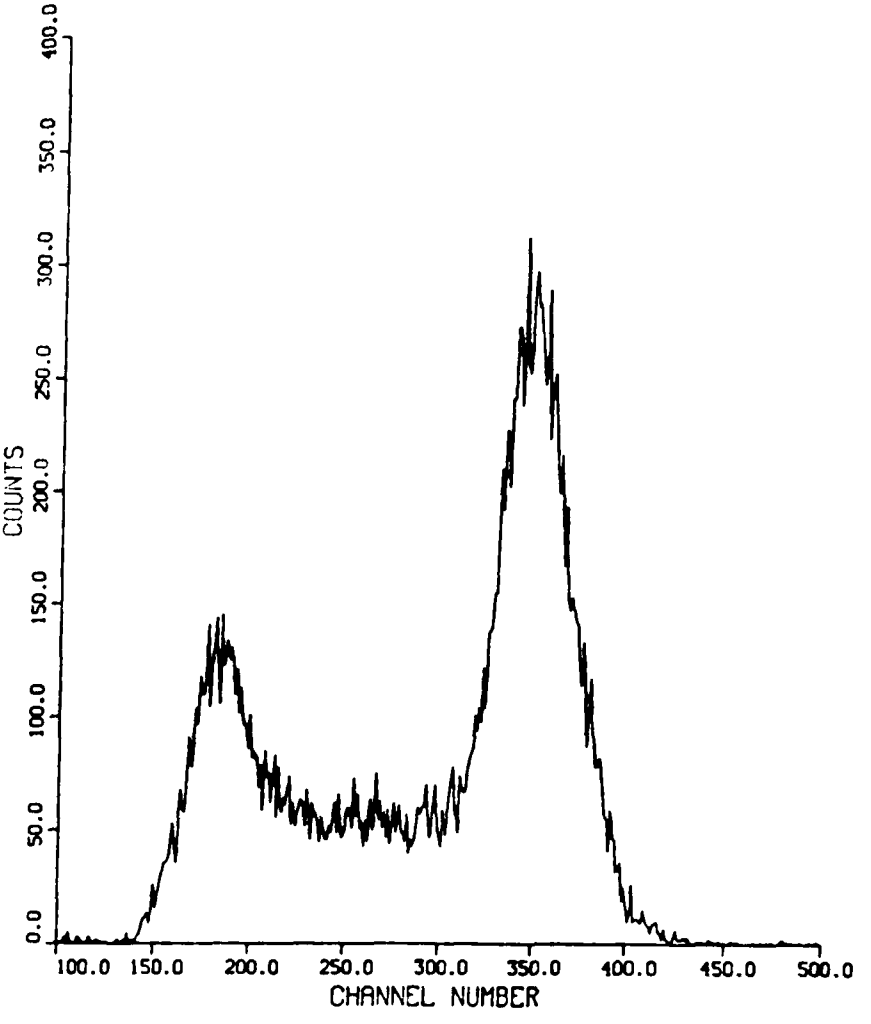

Figure 4.6.4 Diagram showing the calibration run for the plastic scintillators. It shows the conversion electron lines at 481.7 and 975.6 keV from ^{207}Bi.

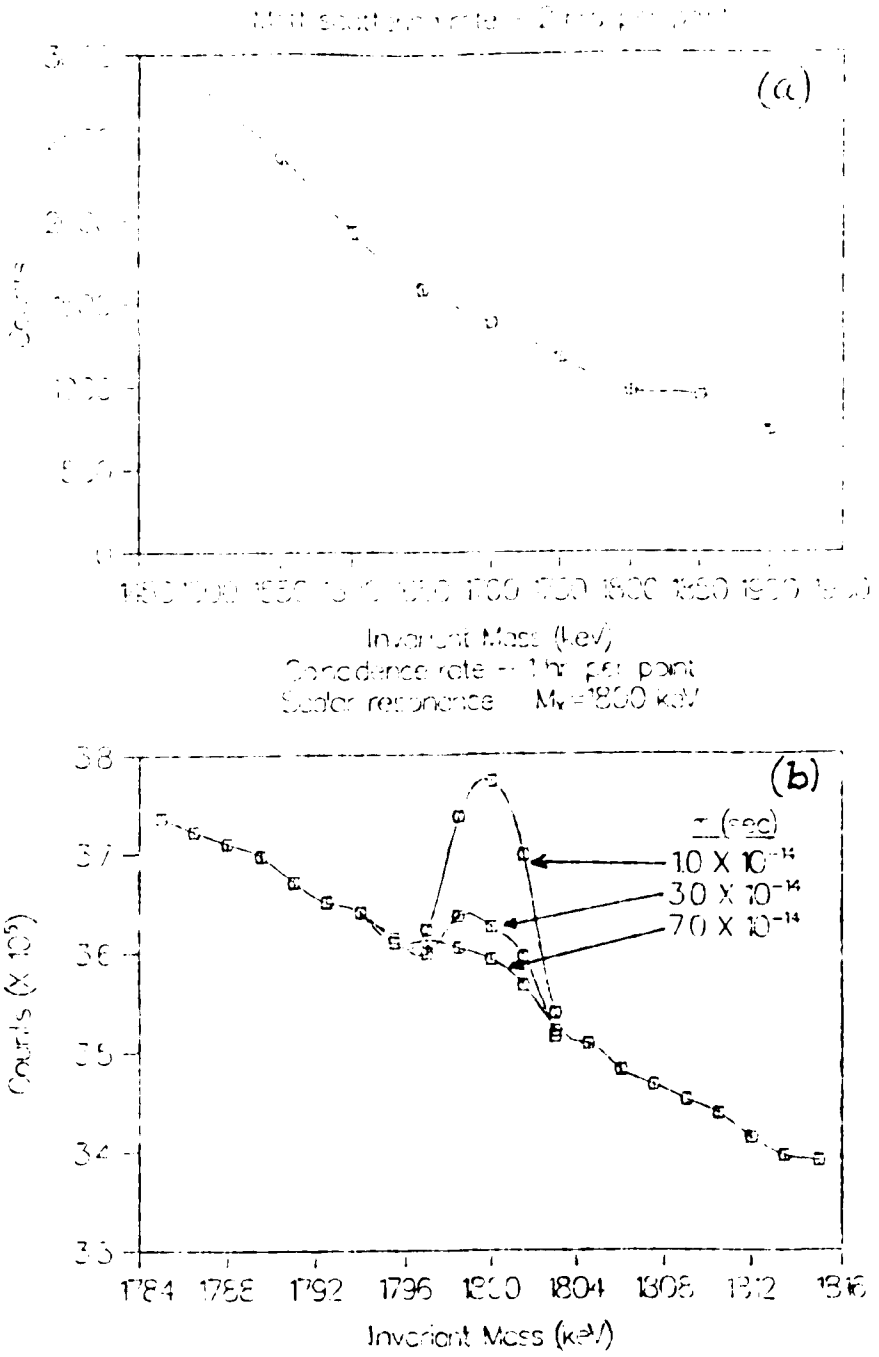

Figure 4.6.5 The diagram showing the Monte-Carlo calculations of (a) the Mott scattering rate and (b) the resonant Bhabha scattering rate for the detector geometry described in the text. The parameters used in the calculations are: $M_X = 1800$ keV, positron beam intensity $= 5 \times 10^6\ e^+/s$.

The Monte-Carlo simulation of the Mott scattered and Bhabha scattered events is shown in Fig. 4.6.5[75]. The figure shows the expected event rates in our detector geometry. The resonant cross section is calculated by assuming a neutral state of mass $M_X = 1800$ keV.

Data acquisition is accomplished with the use of standard CAMAC electronics arranged as shown in Fig. 4.6.6. This figure also shows the trigger logic employed for identifying Bhabha and Mott scattered events. Events that pass hardware cuts are preprocessed/formatted by a Starburst microprocessor. The Starburst is a single CAMAC auxillary crate controller with an onboard PDP 11/73 microcomputer and memory mapped CAMAC interface. As local buffers within the Starburst fill, the stored data are transferred to buffers in the Microvax computer residing in the global common. The data in the global common can be shared by different process for online monitoring. Ultimately the data are then transferred onto a tape by the acquisition process running in the Microvax.

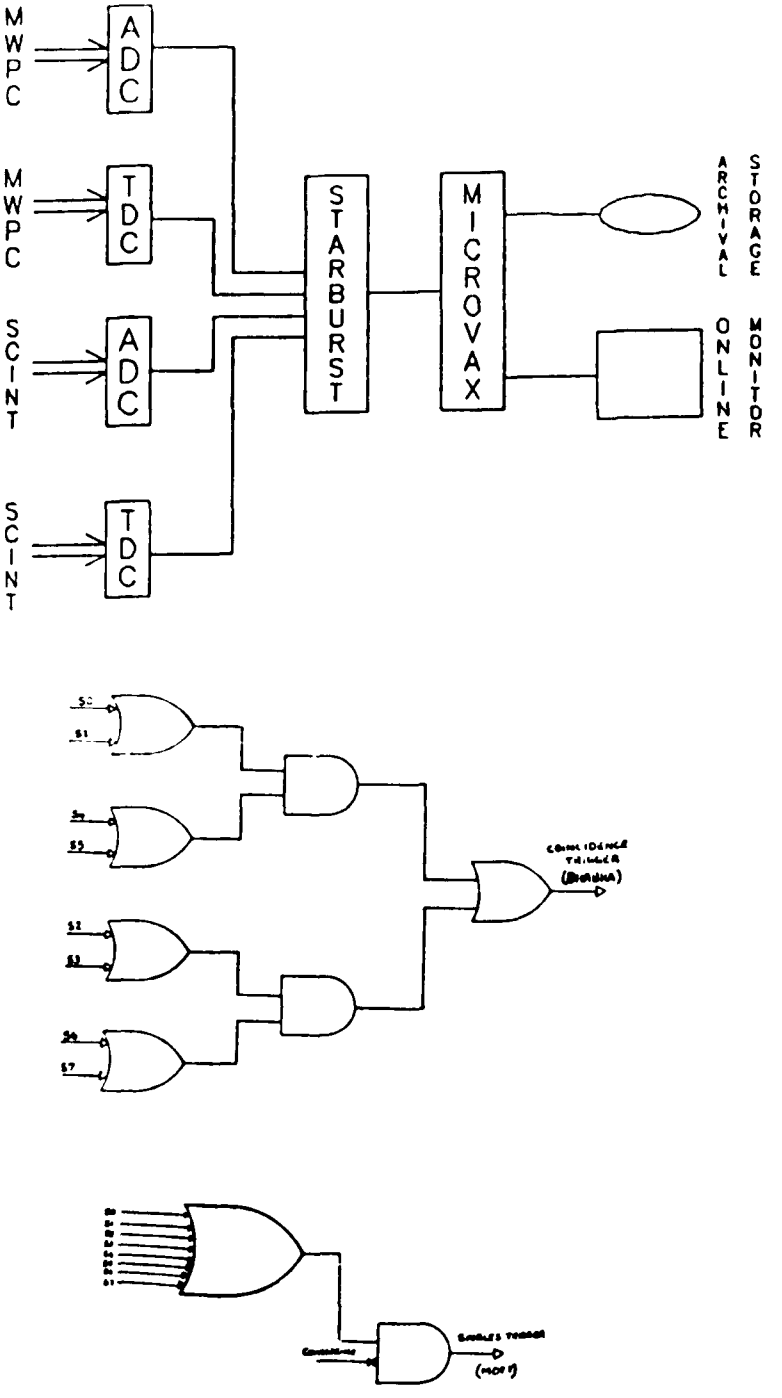

Figure 4.6.6 Block diagram of the data acquisition system and trigger logic. S0,S1,S2,... denotes the Bicron scintillators.

Chapter 5.

Results and Conclusions

In this chapter we will describe the results of the measurements which we carried out in order to determine the characteristics of the positron beam. We will examine the suitability of the beam for resonant searches and briefly review our first observations of Bhabha events.

The total positron beam intensity was measured by steering the beam onto a scintillator located at the object plane of the bending magnet. The maximum intensity achieved in this manner was 5×10^5 e^+/s under typical running conditions. In order to determine the contamination due to high-energy positrons, we increased the grid voltage in the Soa lens to ~ 100 V, a value that is certainly sufficient to stop all of the moderated positrons. The surviving beam is then composed of high-energy positrons. We found that the collimator at the image plane of the 90° bender intercepted a maximum of $\leq$ 6000 high-energy e^+/s, a rate that is not unreasonable considering the solid-angle acceptance of the upstream energy filter and the dispersive properties of the 90° bending magnet. With the transport optics tuned optimally for the moderated positrons, we found that the high-energy contamination from the unmoderated positrons at the target location was less than 1 e^+/s, a value that we believe permits us to classify the beam as one of extremely high purity.

The total positron beam intensity was also monitored with the use of the CEMA's.[111] The gain of the two stage models is of the order of $10^6 - 10^7$.[112] We compared the count rates obtained from a CEMA detector coupled to a ORTEC 142 GH preamplifier and an ORTEC 583 fast discriminator to those obtained either from a calibrated BGO detector[113] and or from a plastic scintillator (active beam collimator). We found, somewhat surprisingly that the counting efficiency of the CEMA was quite high (about 60%) although it decreased with time after extended use, an effect that is correlated with the high event rate per channel ($\sim$ 100 counts/s) to which the CEMA was exposed.[112]

As we noted previously, the CEMA's provided us with a means of visually observing the spatial properties of the beam. The beam "size" observed at the target location in this manner was about 1.5 mm. The small dynamic range of the CEMA detector unfortunately limited the possibility of observing any fine structure in the beam spot. Although a detailed analysis of the shape of the beam was thus precluded, we can nonetheless confidently say that the beam spot is reasonably round.

We also measured the beam size by moving a wedge-shaped plastic scintillator across the beam and counted the number of positrons it intercepted. With this procedure we obtained a beam size of 1.1 mm FWHM, a result that is consistent with the CEMA observations. From measurements of the beam size at the second solenoid and the target location and the knowledge of the distance of the drift region between them, we deduced the beam divergence at the target to be less than 0.5°.

We also used the measurements of the beam size to obtain an estimate of the beam energy distribution. We varied the acceleration energy by ± 1 keV, keeping the optical elements of the transport system (all the solenoids and bending magnet) at a constant value. Under these conditions we observed the position of the positron beam at the target to move a distance of ± 3 mm. As a result we can conclude that the beam energy has distribution with a width that is smaller than 0 5 keV.

We studied the beam energy width further with the use of the HPGe detector and obtained a spectrum with a width of < 4 keV FWHM. After deconvoluting the result with the detector resolution we obtain an intrinsic width of < 1 keV for the positron beam, which is consistent with the result of our beam size studies. The HPGe spectrum measured with a 1.477 MeV positron beam is shown in Fig. 5.1. The distinctive features of this spectrum are the full energy peak and the background on both the low and high-energy side. The high-energy background is produced by the addition of the 511 keV annihilation quanta to the beam energy and shows up above the beam energy as a 511 keV annihilation line together with a corresponding Compton edge. The low-energy background is mainly due to incomplete energy deposition in the 7-mm thick detector as well as to positrons scattered from the active slits which limit the HPGe count rates and which are located between the target and the HPGe detector. During the measurements, the count rate in the HPGe detector was usually between 5 and 20 kHz. The final beam parameters are summarized in Table 5.1.

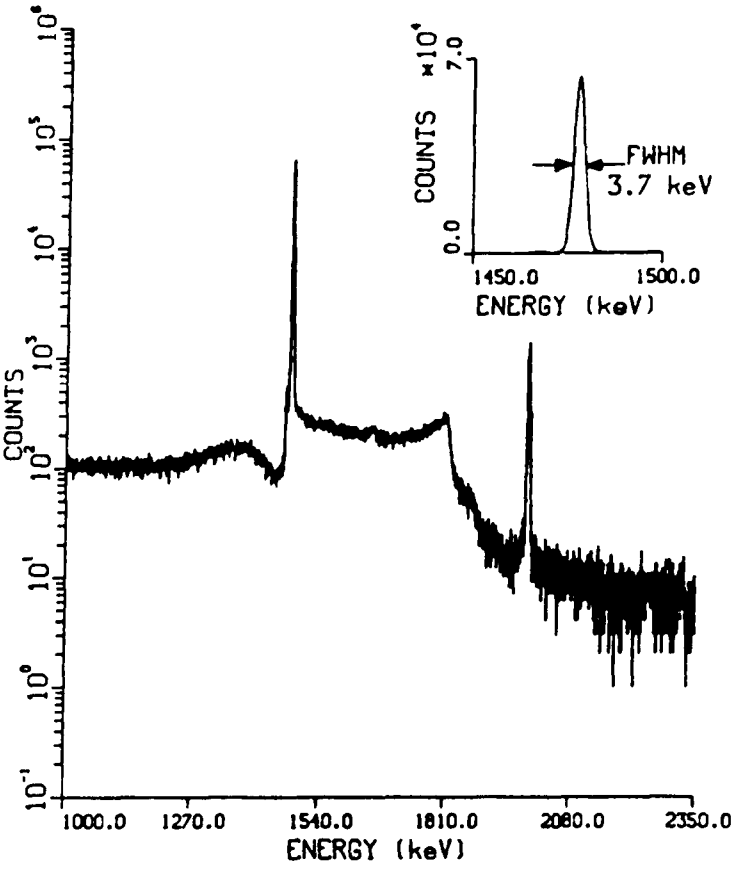

Figure 5.1 The measured HPGe spectrum of a 1.4 MeV positron beam. The annihilation line and the compton edge above the beam energy is due to the addition of the 511 keV γ-line to the beam energy. Resolution of the detector is 3.5 keV FWHM.

^{22}Na SOURCE ACTIVITY	250 mCi
β^+ YIELD OF THE ^{22}Na SOURCE	16%
MODERATOR EFFICIENCY	5×10^{-4}
TOTAL TRANSPORT EFFICIENCY	$\sim 80\%$
e^+ INTENSITY AT THE TARGET	$5 \times 10^5 e^+/s$
HIGH-ENERGY CONTAMINATION	$< 1 e^+/s$
BEAM SIZE,FWHM	1.1 mm
BEAM DIVERGENCE HALF ANGLE	$< 0.5°$
BEAM ENERGY SPREAD, FWHM	< 1 keV

Table 5.1 Characteristics of the 3 MeV positron beam.

We note that the position of the measured conversion electron lines used for the beam energy calibration moved at a rate 0.5 keV/day during the experimental run, a behaviour that is consistent with energy loss in residual gas condensation on the cooled detector surface for a vacuum system with a base pressure of 1×10^{-6} Torr. We point out that the residual gas in our unbaked and cryopumped vacuum system consists mainly of water vapour. Due to the water condensates and the calibration procedure, the accuracy of the positron beam energy measurement is thus limited to ± 200 eV.

During our first Bhabha observations we scanned the positron beam energy E_+ over an energy range from 2150 to 2350 keV in steps of 5 keV. We monitored the beam energy at the beginning and at the end of each run. Before starting to record data for a particular energy value, we performed the following steps to minimize systematic errors in the data sample. First we scaled the bending magnet current to the value corresponding to the desired beam energy. Then we adjusted the high voltage of the accelerator column so that the beam passed through the center of the image slit located at the image focal point of the bending magnet. At this point we checked the energy of the beam with the HPGe detector and readjusted the accelerator voltage if necessary. Using the CEMA at the target location we checked the shape of the beam and fine-tuned the solenoids to optimize the image.

In order to ensure that the beam was centered on the target in the same way for each energy, we required the Mott scattering rates from a teflon target be the same (to within $\pm\sqrt{\text{mean number of counts}}$) in each of the four quadrants of the Bicron pyramid detector. We achieved this centering by steering the beam spot on the target with the help of a pair of deflector coils situated 50 cm upstream of the target chamber. Finally we recorded the beam energy and collected data for 10-20 minutes without any target in place. During this target-free run, we demanded that there be no signal corresponding to the beam energy and that the event rates remain essentially the same as that of a run without the beam present. The background events

are believed to be originating from cosmic ray background. The data collected without the target in place provided an estimate of background rates before the start of a run and ensures that the beam is well tuned.

During our preliminary studies we collected 50,000 coincidence events with both lithium and teflon targets at each of 40 energy values in the range of 2150-2350 keV. (This sample is much larger than the number of events accumulated by any other group.) The hardware triggers used to record the Mott events and the Bhabha events are as follows. (See Fig. 4.6.6.) A Mott-scattered event (called a single event) is identified when one and only one of the Bicron plastic scintillator quadrants has a signal and the energy deposited is higher than 400 keV. An event is recorded as a coincidence event, if the opposite quadrants of the Bicron scintillator is fired within 35 nsec.

In Fig. 5.2 and 5.3 we show some of the online histograms monitored to ensure a smooth performance of the detectors and beam during a run. Figs. 5.2 (a) and (b) show the energy spectrum of the Mott scattered events and the sum energy spectrum spectrum of the Bhabha events, respectively. The FWHM of these spectra are 195 and 230 keV respectively. The low-energy tail in the Mott spectrum is caused by the multiple scattering of positrons from the detector frames. The azimuthal distribution of the Mott scattered events corresponding to the four quadrants are shown in Fig. 5.3(a). The coplanarity distribution of the coincidence events, pictured in Fig. 5.3(b) has a FWHM of 15°. The distribution of opening angles between the coincident event partners, shown in Fig. 5.3(c) has a FWHM of 5°.

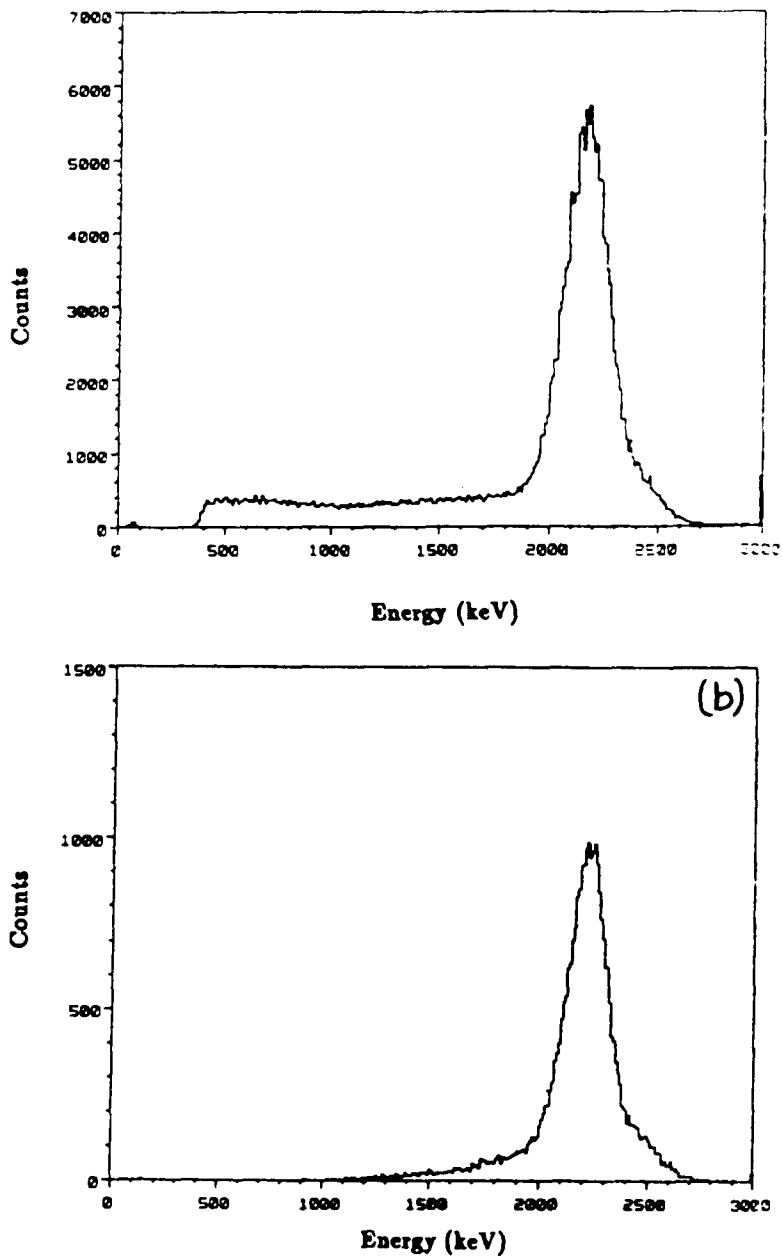

Figure 5.2 The observed energy spectrum of the (a) Mott and (b) Bhabha events in the Bicron scintillators.

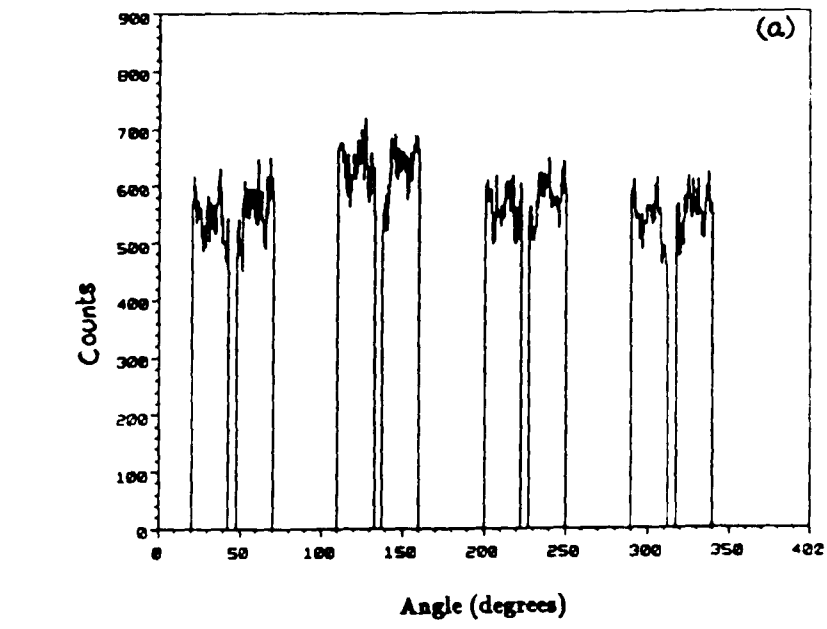

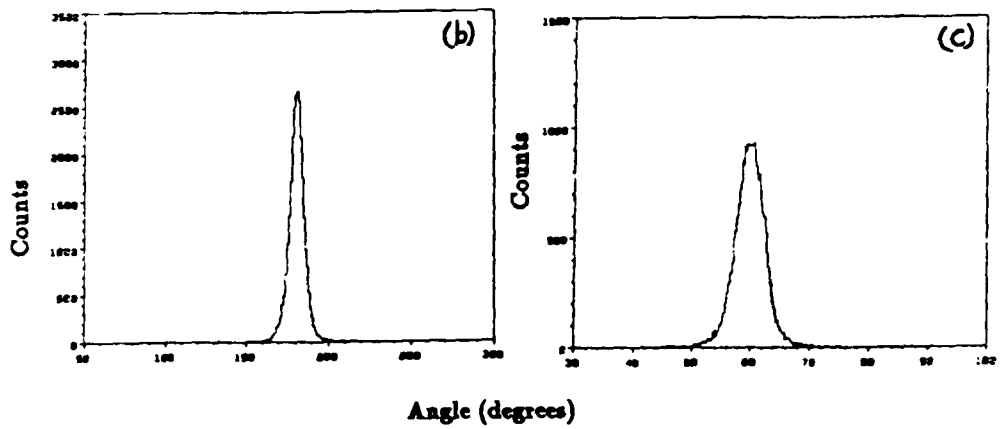

Figure 5.3 (a) The azimuthal angular distribution of Mott events (b) coplanarity of the Bhabha events, and (c) the distribution of opening angles between Bhabha event partners.

At present, we are analyzing the data sample to identify and correct for systematic errors. One of the main ambiguities in the experiment is associated with the normalization scheme as is evident from the shape of the singles energy-spectrum of Fig. 5.2(a). In order to estimate the number of Mott scattered events for a particular energy value, the total number of events in the elastic peak have to be determined. However, the singles energy-spectrum has a long tail on the low-energy side of the elastic peak, which shifts the base line of the elastic peak and alters the estimated number of events in the elastic peak. As pointed out earlier, the low-energy tail is caused by the positrons scattered at small angles from the target, with a subsequent scattering either from the target chamber and or the support structure of the detector system. Presently, we are performing different fitting procedures for the Mott spectrum (a gaussian for the elastic peak with a smooth background) and are hoping to arrive at a unique normalization scheme. Since the tail distribution is caused by the low-angle positron scattering, the distribution is very sensitive to the direction of the incident beam and hence a small change in the incident beam direction from one energy point to another can result in large systematic errors. Even though this normalization problem is encountered by all of the Bhabha scattering experiments,[76 -90] it is largely ignored.

In conclusion, we have developed an intense monoenergetic positron beam suitable for use in a Bhabha search experiment. We have made detailed measurements of the beam properties. Based upon preliminary measurements of Bhabha coincidences we believe that the Brookhaven experimental program will yield results of a quality that surpass those obtained elsewhere.[76 -90] We further believe that the comprehensive studies of systematic effects which we performed during our beam characterization measurements should assist other experimental groups that engage in similar research.

Although, we developed our positron beam for the specific purpose of searching for an s-channel resonance in Bhabha scattering, we note that our technical achievements may have other ramifications. The fabrication of the intense ^{22}Na source at Brookhaven is likely to be emulated elsewhere. The electrostatic energy filter should be of great utility in many other moderated positron applications.[98] Finally the Dynamitron beam itself should be very useful for studies of positron channeling effects, precision measurements of in-flight annihilation, and development of a positron microbeam. We therefore believe that our work has substantially advanced the frontiers of positron science.

References

1. T.E. Cowan, J.S. Greenberg in *Physics of Strong Fields*, NASI ser. B, 153 ed. W. Greiner,(Plenum Pub. Co. New York,1987),p111.

2. W. Greiner, B. Müller, and J. Rafelski, *Quantum Electrodynamics of Strong Fields*, (Springer-Verlag,Berlin,1985).

3. E. Bedrermann, *et al.*, GSI Scientific Report 1988, GSI 89-1,157(1989).

4. P.J. Mohr, Phys. Rev. Lett. 34,1050(1975).

5. D.A. Owen, Phys. Rev. Lett. 30,887(1973).

6. T. Kinoshita, IEEE Trans. on Instr. and Methods, IM-36,201(1987).

7. E. Merzbacker, *Quantum Mechanics*, John-Wiley&Sons, New York, p607(1970).

8. J.S.Greenberg, *et al.*, Phys. Rev. Lett. 39,1404(1977).

9. C. Kozhuharov in *Physics of Electronic and Atomic Collisions*, ed. by S. Datz (North Holland, Amsterdam,1982) p.179.

10. P. Kienle, Ann. Rev. Nucl. Part. Sci. 36,605(1986).

11. W.E. Meyerhof *et al.*, Phys. Lett. B 69,41(1977).

12. H. Backe, In *Trends in Physics*, ed. M.M. Woolfson, Bristol: Adam Higler, 445(1979).

13. G. Soff, *et al.*, Phys. Rev. Lett. 38,592(1977).

14. J.S. Greenberg in *X-ray and Atomic Inner Shell Physics*, ed. B. Crasemann, American Institute of Physics, New York, 173(1982).

15. D. Schwalm in *Electronic and Atomic Collisions*, ed J. Eichler *et al.*, Elseveir, 295(1984).

16. H. Bokemeyer, *et al.* in *GSI Scientific Report*, GSI-81-2:127(1981).

17. J. Schweppe, *et al.*, Phys. Rev. Lett. 51,2261(1983).

18. J.S. Greenberg and P. Vincent in *Treatise on Heavy-Ion Science, Vol. 5: High Energy Atomic Physics*, ed. D.A. Bromley, Plenum, New York, 138(1985).

19. M. Clemente *et al.*, Phys. Lett. 137B,41(1984).

20. W. Koenig, *et al.*, Z.Phys. A - Atomic Nuclei 328, 129(1987).

21. T. Cowan, *et al.*, Phys. Rev. Lett. 54,1761(1985).

22. A. Schäfer, J. Phys. G: Nucl. Phys. 15,373(1989).

23. T. de Reus, *et al.*, Z. Phys. D 8,305(1988).

24. G. Soff, *et al.*, Physica Scripta 36,743(1987).

25. T. Cowan, *et al.*, Phys. Rev. Lett. 56, 444(1986).

26. L.M. Krauss and M. Zeller, Phys.Rev. D34,3385(1986).

27. A. Passoja, *et al.*, Nucl. Inst. Methods, 157,513(1978); M. Neissian, *et al.*, Phys.Rev., 125,639(1962).

28. D. Burch *et al.*, Phys. Lett. 40B,357(1972).

29. W. Litchen and A. Robatino, Phys. Rev. Lett. 54,781(1985); T. de Reus *et al.*, Z. Phys. D8,305(1988).

30. D. Carrier and L.M. Krauss, Phys. Rev. C 38,1225(1988).

31. J. Reinhardt, *et al.*, Phys. Rev. C 33,194(1986).

32. For a summary of standard axion results see: T.W. Donnelly, *et al.*, Phys. Rev. D 18,1607(1978).

33. J.E. Kim, Phys. Rep., 150,1(1987).

34. C. Edwards *et al.*, Phys. Rev. Lett. 48,903(1982); M. Sivertz *et al.*, Phys. Rev. D 26,717(1982); M.S. Alam *et al.*, Phys. Rev. D 27, 1665(1983).

35. R.D. Peccei *et al.*, Phys. Lett. 172,189(1986); L.M. Krauss and F. Wilczek, Phys. Lett. 173,189(1986).

36. R. Eichler *et al.*, Phys. Lett. B 175,101(1986).

37. D.A. Bryman and E.T. Clifford, Phys. Rev. Lett. 57,2787(1986).

38. G. Ang *et al.*, Z. Phys. 228,151(1969); M. Suzuki, Phys. Lett. B 175,364(1986).

39. N.J. Baker *et al.*, Phys. Rev. Lett. 59,2832(1987).

40. A. Konaka, *et al.*, Phys. Rev. Lett. 57,659(1986).

41. M. Davier, *et al.*, Phys. Lett. B 180,295(1986).

42. E.M. Riordan, *et al.*, Phys. Rev. Lett. 59,755(1987).

43. C.N. Brown, *et al.*, Phys. Rev. Lett. 57,2101(1986).

44. Y.S. Tsai, Phys. Rev. D 34,1326(1986).

45. A. Schäfer, *et al.*, Mod. Phys. Lett. A 1,1(1986).

46. M.W. Ritter, *et al.*, Phys. Rev. A 30,1331(1984);
A.P.Mills and G.H.Bearman, Phys. Rev. Lett. 34,246(1975).

47. A. Schäfer, *et al.* J. Phys. G: Nucl. Phys. 11,L69(1985).

48. S.M. Ludeen and F.M. Lipkin, Phys. Rev. Lett. 46,232(1981).

49. L. Taucher, *et al.*, Phys. Rev. Lett. 35,410(1975).

50. T. Kinoshita, *et al.*, Phys.Rev. Lett. 52,717(1984).

51. B.N. Taylor, J. Res. Natl. Bur. Stand., 90,91(1985).

52. R.S. Van Dyck, Jr., in *Atomic Physics*, 9, eds. R.S. Van Dyck, Jr. and E.N. Fortson, World Scientific, Singapore, 53(1984).

53. J. Bailey, *et al.*, Nucl. Phys. B 150,1(1979).

54. J. Reinhardt, *et al.*, Z. Phys. A. 327,367(1987).

55. Cheuk-Yin Wong and R.L.Becker, Phys. Lett. B 182,251(1986).

56. K. Geiger, *et al.*, Z. Phys. A. 329,77(1988).

57. B. Müller, J. Reinhardt, W. Greiner, and A. Schäfer, J. Phys. G: Nucl. Phys. 12,L109(1986).

58. L.S. Celenza, V.K. Mishra, C.M. Shakin, and K.F. Liu, Phys. Rev. Lett. 57,55(1986); L.S. Celenza, C.R. Ji, and C.M. Shakin, Phys. Rev. D 36, 2144(1987); L.S. Celenza, A. Pantziris, C.M. Shakin, and Hui-Wen Wang, Brooklyn College preprint, B.C.C.N.T 88/031/175 (March,1988).

59. Y.J. Ng and Y. Kikuchi, Phys. Rev. D 36,2880(1987); Y.Kikuchi and Y.J.Ng, North Carolina preprint, IFP-314-UNC (April,1988).

60. D.G. Caldi and A. Chodos, Phys. Rev. D 36,2876(1987); D.G. Caldi, A. Chodos, K. Everding, D.A. Owen, and S. Yafaesefat, Yale preprint, YCTP-P21-88 (Sept. 1988).

61. see for example: S. Meshkov, p125, *Experimental Meson Spectroscopy - 1983*, ed. S.J. Lindenbaum, American Institute of Physics, New York (1984).

62. P. Fomin, *et al.*, Riv. Nuovo Cim. 6,1(1983);
T. Maskawa and H. Nakajima, Prog. Theor. Phys. 52,1326(1974).

63. J. Kogut, E. Dagotto, and A. Kocic, Phys. Rev. Lett. 60,772(1988);
E. Dagotto and J. Kogut, Phys. rev. lett. 59,617(1987).

64. R.D. Peccei, DESY, Hamburg, preprint # DESY 88-024(1988).

65. E. Dagotto and H.W. Wyld, Phys. Lett. B 205,73(1988).

66. S. Schramm, B. Müller, J. Reinhardt, and W. Greiner, Mod. Phys. Lett. A 3,783(1988).

67. see for example: T.D. Lee, p553, *Particle Physics and Introduction to Field Theory*, Harwood Academic Publishers, New York, (1981).

68. A. Ashkin, L.A. Page, W.M. Woodward, Phys. Rev. 94,357(1954).

69. F. Halzen and A.D. Martin, *Quarks and Leptons: An Introductory Course in Modern Particle Physics*, John Wiley & Sons, New York, (1983).

70. J.D. Bjorken and S.D. Drell, p 104, in *Relativistic Quantum Mechanics*, McGraw-Hill, Inc. (1964).

71. see for example: J.M Jauch and F. Rohrlich, p260 in *The Theory of Photons and Electrons*, Addison-Wesley Pub. Co. Inc., (1955).

72. see for example: C.J. Joachain, p439, *Quantum Collision Theory*, North-Holland Pub. Co., Amsterdam, (1975).

73. D.G. Caldi, *et al.*, Phys. Rev. D 39,1432(1989).

74. M. Cooper, Rep. Prog. Phys., 48,415(1985).

75. S.D. Henderson, pvt. communication, not published, (1989).

76. K.A. Erb, I.Y. Lee, and W.T. Milner, Phys. Lett. B 181,52(1986).

77. R. Peckhaus, *et al.*, Phys. Rev. C 36,83(1987).

78. T.F. Wang, *et al.*, Phys. Rev. C 36,2136(1987).

79. Chr Bargholtz, *et al.*, J. Phys. G: Nucl. Phys. 13,L265(1987).

80. M. Sakai, *et al.*, Phys. Rev. C 38,1971(1988).

81. A.P. Mills, Jr. and J. Levy, Phys. Rev. D 36,707(1987).

82. U. von Wimmersperg, *et al.*, Phys. Rev. Lett. 59,266(1987).

83. K. Maier, *et al.*, Z. Phys. A: Atomic Nuclei, 326,527(1987).

84. K. Maier, *et al.*, Z. Phys. A: Atomic Nuclei, 330,173(1988).

85. E. Lorenz, *et al.*, Phys. Lett. B, 214,10(1988).

86. H. Tsertos, *et al.*, Phys. Lett. B 207,273(1988).

87. H. Tsertos, *et al.*, Z. Phys. A: Atomic Nuclei, 331,103(1988).

88. U. Grundinger ed., GSI preprint No. GSI09-87 p3 (1988).

89. S.H. Connell, *et al.*, Phys. Rev. Lett. 60,2242(1988).

90. M. Minowa, *et al.*, U. Tokyo preprint no. UT-ICEP-88-05(1988).

91. K. Maier, *et al.*, p171, *Positron Annihilation*, eds. L. Dorikens-Vanpraet, M. Dorikens, and D. Segers, World Scientific, Singapore, (1989).

92. K. Danzmann, *et al.*, Phys. Rev. Lett. 59,1885(1987).

93. K. Danzmann, *et al.*, Phys. Rev. Lett. 62,2353(1989).

94. M.R. Cleland and P.Farrell, IEEE Trans. on Nucl. Sci., 227, June (1965).

95. G. Gräff *et al.*, in *Positron Scattering in Gases*, eds. J.W. Humberston and M.R.C. McDowell, Plenum Publishing Corporation, (1984).
P.H. Howell, *et al.*, Seventh Conference on the Application of Accelerators in Research and Industry, North Texas State University, Dentor, Texas (1982).

96. K.G. Lynn and W.E. Frieze, p165, *Positron Scattering in Gases*, eds. J.W. Humberston and M.R.C. McDowell, Plenum Publishing Corporation, (1984).

97. H. Huomo *et al.*, to be published, (1989).

98. P.J. Schultz and K. G. Lynn, Rev. Mod. Phys. 60,701(1988); And references there in.

99. C.D. Beling and M. Charlton, Contemp. Phys. 28,241(1987).

100. E. Gramsch, J. Throwe, and K.G. Lynn, Appl. Phys. Lett. 51, 1862(1987).

101. D.A. Fischer, K.G. Lynn, and D.W. Gidley, Phys. Rev. B 33, 4479(1986).

102. V.W. Hughes, R.L. Long Jr, M.S. Lubell, M. Posner, and W. Raith, Phys. Rev. A 5,195(1972).

103. K.F. Canter, P.H. Lippel, W.S. Crane, and A.P. Mills, Jr., *Positron Studies of Solids, Surfaces, and Atoms*, ed. A.P.Mills, Jr., W.R. Crane, and K.F. Canter, World Scientific, (1984).

104. W.B. Herrmannsfeldt, SLAC Report No. 226, Stanford Linear Accelerator Center (1979).

105. D.C. Carey, *The Optics of Charged Particle Beams*, Harwood Academic Publishers, New York (1987).

106. K.F. Canter, P.H. Lippel, and D.T.Nguyen, *Positron Studies of Solids, Surfaces, and Atoms* ed. A.P. Mills, Jr., W.R. Crane, and K.F. Canter, World Scientific (1984).

107. K.L. Brown, R. Rothacker, D.C. Carey, and ch. Iselin, SLAC Report No. 91, Rev. 2, Stanford Linear Accelerator Center, (1977).

108. A.B. El-Kareh and J.C.J. El-Kareh, p252, in *Electron Beams, Lenses, and Optics*, Volume 1, Academic Press (1970).

109. S. Penner, Rev. Sci. Instr., 32,150(1961).

110. V. Radeka in *Experimental Techniques in High Energy Physics* Ed. Thomas Ferbel, Addison-Wesley Publishing Company, Inc., 579(1987).

111. Model number 6025/3025, Galileo Electro-Optics Corp. Galileo park, Sturbridge, Massachusetts, USA.

112. J.L. Wiza, Nucl. Instr. and Meth. 162,587(1979).

113. Model number 2M2/2-X BGO, Bicron Co., USA.